The Kinematics of Molecular Gas and Dust in the Nearby Galaxies Centaurus A and M82

Thesis by

Alice C. Quillen

In Partial Fulfillment of the Requirements
for the Degree of
Doctor of Philosophy

California Institute of Technology
Pasadena, California
1993
(defended May 3, 1993)

In memory of Milton S. Plesset

ACKNOWLEDGEMENTS

I have many things to be thankful for while I have been at Caltech: for encouragement, help with writing, insight, aid, understanding, advice, cheer, companionship, inspiration, introducing me to the work studied in this thesis, helping me do the work in this thesis, financial support, enjoyable physics and other types of discussions, and enjoyable teaching experiences. For these things I thank the following people:

S. Sridhar, Dini Rath, Paulo Coppi, Cole Miller, Steinn Sigurdsson, Garrett Biehle, Theresa Brainerd, Mark Voit, Nick Scoville, Lars Bildsten, Sterl Phinney, Bharat Ratra, Chris Thompson, Scott Tremaine, Greg Willette, Peter Goldreich, Jerry Sussman, Kip Thorne, Kurt Cutler, Tom Phillips, Jocelyn Keene, Thomas Buettgenbach, Taco, Gene Serabyn, Connie Walker, James Graham, Lee Armis, James Larkin, Gerry Neugebauer, Andrea Ghez, Tom Soifer, Anneila Sargent, Keith Mathews, Joe Mazzarella, George Djorkovski, Michelle Vine, Todd Brun, Kevin Rauch, David Hogg, Shirley Hampton-Parker, Josh Roth, Andreas Reisenegger, Sanghee Park, Roger Blandford, Lin Yan, Eanna Flanagan, Norman Murray, Renu Malhotra, Steve Winters, Lars Bildsteen, Melvyn Davies, Mark Muldoon, Gisela Schmoll, Michael Lee, Bobby St. Pierre, Mark Morris, Glenn Boyd, Albert Young, David Edehlson, Gino Thomas, Gil Rivlis, Michal Peri, John Schwarz, Patricia Schwarz, Michael Malak, Ruchi Yongsunthon, Seth Lloyd, Eve Zimmerman, Polly Plesset, Janet Jenks, Milton Plesset, Anna Ceresole, Donna Driscoll, Tim de Zeeuw, Ewine van Dishoek, Jacqueline van Gorkom, Jay Frogel, Leon Golub, Alex Ridgeway, Karen O'Neill, Gill Knapp, Dave Montano, David Bhram, Laura Jones, Mary Kennedy, Rob Olling, John Hibbard, Patricia Quillen, Carl G. Quillen, Carl Quillen Jr., Emily Quillen, Emma G. Quillen, the CSO staff, and the CTIO staff.

ABSTRACT

This thesis presents a kinematical study of the molecular gas and dust in the nearby radio galaxy Centaurus A (NGC 5128) and the nearby starburst M82.

The CO (2–1) emission along the inner dust lane of Centaurus A, observed with the Caltech Submillimeter Observatory on Mauna Kea, shows the molecular gas to be in a thin disk, with a velocity dispersion of only about 10 km s^{-1}. The observed line profiles are broadened considerably due to beam smearing of the gas velocity field. The profile shapes are inconsistent with planar circular and noncircular motion. However, a warped disk in a prolate potential provides a good fit to the profile shapes. The morphology and kinematics of the molecular gas is similar to that of the ionized material, seen in Hα. The best fitting warped disk model not only matches the optical appearance of the dustlane, but also agrees with the large scale map of the CO emission, and is consistent with HI measurements at larger radii.

We present infrared images of Cen A (NGC5128) in the J,H, and K bands observed with the 1.5 m telescope at CTIO. The infrared morphology is primarily determined by the presence of a thin absorptive warped disk. By integrating the light of the underlying prolate galaxy through such a disk, we construct models which we compare with infrared and X-ray data. The geometry of the warped disk needed to fit the IR data is consistent with a warped disk which has evolved as a result of differential precession in a prolate potential. The disk has an inclination, with respect to the principal axis of the underlying elliptical galaxy, that is higher at large radii than in the inner region.

A scenario is proposed where a small gas rich galaxy infalling under the force of dynamical friction is tidally stripped. Stripping occurs at different times during its infall. The orientation of the resulting gas disk depends upon the angular momentum of the infalling galaxy. We find that the resulting precession angle of the disk is well described by the precession model, but that the inclination angle may vary as a function of radius. We propose an orbit for the infalling galaxy

that is consistent with the geometry of the warped disk needed to fit our infrared data, rotation observed in the outer part of the galaxy and the location of the stellar shells in the same region.

We model the kinematics of the molecular gas in the nearly edge-on disk in M82, by considering velocity and surface density perturbations caused by a possible rotating kpc long bar. A model with a bar that has an Inner Linblad Resonance at $r \sim 10'' \sim 150$ pc fits the molecular observations of the inner torus. This model is consistent with the angle of the bar inferred from the K (2.2μm) isophotes. The clouds have a cloud-cloud velocity dispersion of $\sim 30\,\mathrm{km\,s}^{-1}$ implying that the disk is unstable to short timescale axisymmetric perturbations. This is consistent with the hypothesis that the high star formation efficiencies in starbursts are due to the the short timescales of gravitational instability. It is likely that the bar has mediated the starburst.

There are serious deviations from our model at large radii. It is likely that there are two components of molecular material which were not considered by our model: (i) a component at large radii that is in the galactic plane and has low line-of-sight velocities due to a larger scale bar or due to the fact that there is a lack of molecular gas over a large range of radius (perhaps due to a previous interaction which caused a large fraction of the gas to sink into the nucleus), and (ii) a molecular wind with velocities of the order of the observed line widths ($80 - 120\,\mathrm{km\,s}^{-1}$). While dense gas can be accelerated in a galactic superwind to velocities of this order of magnitude, it is unclear how this gas interacts with the superwind.

CONTENTS

---

* '.."and what is the use of a book," thought Alice, "without pictures or conversations?"' — Lewis Carroll, *Alice's Adventures in Wonderland*

CHAPTER 1

INTRODUCTION

This thesis reports on a study of the kinematics of the molecular gas and dust in Centaurus A (NGC 5128) and M82. Centaurus A, one of the brightess radio sources in the sky, has double-lobed jets that extend more than 10° on the sky and a compact nuclear source or actice galactic nucleus (AGN) presumably powered by a supermassive black hole. M82 is the brightest extragalactic infrared source; most of this radiation is emitted from its nuclear region (inner kpc) where there is a high rate of star formation. Both of these galaxies are considered 'active'; by 'activity' we mean luminosities that are higher than could be sustained over a Hubble time by a normal population of stars. Because these two galaxies are bright and nearby (at a distance of ~ 3 Mpc), they are studied in all possible wavelengths and provide an opportunity to study in detail the environment where galactic 'activity' is found.

It has often been suggested that interactions between galaxies can cause enhanced galactic activity. By galaxy interactions we mean the full range of phenomena from grazing galaxy-galaxy encounters to highly dissipative mergers. Baade and Minkowski (1954) suggested that because of its prominent dust lane the galaxy NGC 5128 (then identified with the bright radio source Centaurus A) was the product of a merger between a small spiral galaxy and a large elliptical. Tidal interactions between galaxies modeled numerically by Toomre and Toomre (1972) display much of the observed phenomenology (i.e., tails and bridges) of irregular galaxies. Toomre and Toomre also suggested that tidal interactions not only affect the outer parts of galaxies but also may be responsible for fueling of 'activity' and star formation (i.e., "stoking the furnace") in the nuclear region of an interacting galaxy by accretion of gas from the companion or from its own outer disk. Larson and Tinsley (1978) confirmed this suggestion when they found that starbursting galaxies are often associated with evidence of violent galactic dynamical phenomena. More detailed N-body simulations (e.g., Barnes and Hernquist 1991) including hydrodynamics have shown that channeling of gas into the nuclear region of interacting galaxies can be highly efficient. This lends support to the active galactic nucleus (AGN) formation and fueling scenario formulated by Norman and Scoville (1988), Gunn 1979 ("feeding the monster") and others.

1. *Evidence that Activity is Related to Interactions*

Starbursts

Recent work has shown that there is strong observational evidence linking galaxy interactions to activity in starbursting galaxies (see reviews by Heckman 1990 and Kennicutt 1990). There seems to be a preponderance of tidally disturbed pairs of galaxies among samples of starbursting galaxies; "ultraluminous" ($L_{IR} > 10^{12} L_{\odot}$) IRAS galaxies (Soifer *et al.* 1984), and Markarion galaxies (Karachentsev and Karachentseva 1974). 50% of "ultraluminous" galaxies have double nuclei and 50% of IR galaxies with intermediate luminosities are classified as morphologically peculiar. Samples of strongly interacting galaxies have star formation rates that are at least twice as high as normal disk galaxies (see the list of references cited in Heckman 1990).

M82, though not an ultraluminous galaxy, does show evidence of previous interaction. M82 suffered a nearby collision with M81 and NGC3077 approximately 2×10^8 years ago which is responsible for the large steamers and tails of HI observed linking the three galaxies (Yun 1992, Cottrell 1977). The results of a restricted N-body simulation of the three galaxy collision reproduces remarkably well the observed velocities and distribution of this gas (Yun 1992, Brouillet *et al.* 1991). It has been frequently suggested that the tidal interaction between the three galaxies triggered the starburst in the nucleus of M82.

Radio Galaxies

Evidence of previous mergering is also correlated to activity in radio galaxies, though the evidence is less strong than in the case of starbursts. For example, the two nearest radio galaxies (Centaurus A and Fornax A) have both shell–like stellar features and gas. Numerical simulations of galaxy collisions (Hernquist and Quinn 1988, 1989) indeed show shell–like features similar to those observed in the outer parts of Cen A (Malin, Quinn and Graham 1983) and other galaxies. Powerful radio galaxies appear to be in regions of higher galaxy density than less powerful ones (Heckman *et al.* 1985) and many of them have complicated optical morphologies displaying features such as tidal tails, fans, shells and dust features (Heckman *et al.* 1986).

2. *What is Needed to Fuel an AGN or Starburst?*

Fueling Starbursts

If the high rate of star formation observed in starbursts continues then the gas supply would be exhausted in a very short time ($< 10^8$ years). These high star rates cannot be maintained also because the large energy release from supernovae formed after 10^6 years will disrupt the star forming region removing much of the available gas (Chevalier and Clegg 1985) and stabilizing the gas remaining against gravitational collapse. Larson (1987) suggested that in order for a starburst to occur, a substantial fraction of the interstellar medium in a galaxy must accumulate quickly in the nuclear region where the time scale for gravitational collapse is short so that most of the gas mass can be converted efficiently into stars before many supernovae are formed. In order for this to happen, large scale non-circular dissipative motions are required. It has been demonstrated through numerical simulations that non-axisymmetric distortions in the potential of a galaxy caused by galaxy interactions can be very efficient at funneling gas into the nucleus of the galaxy (Barnes and Hernquist 1991, Noguchi 1987,1988).

Fueling AGNs

Fueling of an AGN, presumably powered by a supermassive black hole (Begelman *et al.* 1984) requires transfer of angular momentum from galaxy size scales (kpc) to scales less than a pc. Conventional accretion (in an axisymmetric thin disk with viscous torques) is inefficient at coupling the region further than a pc from the black hole to the inner region. It is unlikely that compact star clusters can be converted into 'digestible' fuel so gas is considered as a form for the fuel and either a large non-local viscosity or a high temperature in the gas disk is required in order to fuel the AGN continuously (see the review by Shlosman 1990).

3. *Why Study Molecular Gas and Dust?*

In the inner kpc of galaxies, the largest fraction of the interstellar medium (ISM) (by mass) is in the form of dense molecular clouds, presumably due to the higher pressures in this region (Elmegreen 1993). Kinematic studies traditionally done through observations of atomic hydrogen are therefore difficult to carry out in this region and do not observe the material in which star formation occurs. Recent innovations in receiver and telescope technology have permitted highly sensitive observations in carbon dioxide (CO) and other molecules; the spectra have the velocity resolution ($< 10\,\mathrm{km\,s^{-1}}$) required in order to carry out a kinematic study that is not easily obtainable through observations of optical emission lines such as Hα (e.g., Bland *et al.* 1987) which also may be hampered by extinction. Because the central regions of 'active' galaxies are shielded by gas, details learned about this gas allows us to attempt to 'unveil' the AGN or starbursting nucleus.

Molecular gas clouds if they collide are highly dissipative, so the gas is expected to settle quickly onto simple closed periodic orbits. A kinematically study permits tracing of the potential of the galaxy, in particular evidence of non-axisymmetric distortions (which can cause gas inflow into the nucleus) may be detectable. At the time that the data in this thesis were obtained, we were restricted to single dish observations and high spatial resolution (interferometric) data were not easily available. The molecular data were complemented with higher resolution near infrared continuum images which trace the gas disk through absorption by dust. At infrared wavelengths because of reduced extinction by dust it is possible to see deeper into the nuclear region than at optical wavelengths. Although the gas in the inner region, may have settled onto periodic orbits, the orientation angle of the gas in the potential varies on a much longer time scale (e.g., Steiman-Cameron and Durisen 1988), and evidence of previous mergers or interactions may still be detectable in the gas.

4. *Outline of Thesis*

In this thesis we concentrate on the environment that galactic activity find itself by studying in detail the kinematics of molecular gas and dust in the two nearby active galaxies Centaurus A (NGC 5128) a radio galaxy, and M82, a starbursting galaxy. In Chapter 2 observations of the emission from the dust lane in Centaurus A in the rotational transition line $J = 2 \rightarrow 1$ of carbon monoxide are presented. A model for the geometry of the gas disk is proposed based on the kinematics of the spectra. In Chapter 3, near infrared continuum images of Centaurus A are presented. The model for the disk is extended to larger radii and a scenario for the merger that resulted in the present appearance of the galaxy is proposed. In Chapter 4, observations of the starbursting region in M82 $J = 3 \rightarrow 2$ and $J = 2 \rightarrow 1$ lines of carbon dioxide are presented. A kinematical model with non-circular motions induced by a rotating bar is found to fit the data.

REFERENCES

Baade, W. & Minkowski, R. 1954, ApJ, 119, 206.

Barnes, J.E. & Hernquist, L.E. 1991, ApJL, 370, L65.

Begelman, M.C., Blandford, R.D & Rees, M.J. 1984, Rev. Mod. Phys., 56, 255.

Bland, J., Taylor, K., & Atherton, P.D. 1987, MNRAS, 228, 595.

Brouillet, N., Combes, F., & Baudry, A. 1991, IAU Symp Vol 146, 347.

Chevalier, R.A., & Clegg, A.W. 1985, Nature, 317, 44.

Cottrell, G.A. 1977, MNRAS, 178, 577.

Elmegreen, B.C. 1993, preprint.

Gunn, J. 1979 In Active Galactic Nuclei, ed. C. Hazard, S. Mitton, p.213 (Cambridge University Press).

Heckman, T.M., Carty, T. J., & Bothum, G.D. 1985, ApJ, 288, 122.

Heckman, T.M., Smith, E.P., Baum, S.A., van Breugel, W.J.M., Miley, G.K., Illingworth, G., Bothum, G.D., & Balick, B. 1986, ApJ, 311, 526.

Heckman T.M 1990, in Paired and Interacting Galaxies, International Astronomical Union Colloquium No. 124, edited by J.W. Sulentic, W.C Keel and C.M Telesco, p359.

Hernquist, L., & Quinn, P.J. 1988, ApJ, 331 , 682.

Hernquist, L., & Quinn, P.J. 1989, ApJ, 342, 1.

Karachentsev and Karachentseva 1974.

Kennicutt R.C Jr 1990, in Paired and Interacting Galaxies, International Astronomical Union Colloquium No. 124, edited by J.W. Sulentic, W.C Keel and C.M Telesco, p269.

Larson, R. 1987, in Starbursts and Galaxy evolution, ed. T. Thuan, T. Montmerle, and T. Tran Thahn Van (Editions Frontieres: Paris), p. 467.

Larson, R. & Tinsley, B. 1978, ApJ, 219, 46

Malin, D.F., Quinn, P.J., & Graham, J.A. 1983, ApJL, 272, L5.

Noguchi, M. 1987, MNRAS, 228, 635.

Noguchi, M. 1988, A& A, 203, 259.

Norman, C. & Scoville, N. 1988, ApJ, 332, 124.

Soifer, B.T., Rowan-Robinson, M., Houck, J.R., DeJong, T., Neugebauer, G., Aumann, H.H., Beichman, C.A., Boggess, N., Clegg, P.E., Emerson, J.P., Gillett, F.C., Habing, H.J., Hauser, M.G., Low, F.J., Miley, G., & Young, E 1984 ApJL, 278, L71.

Shlosman, I. 1990, in Paired and Interacting Galaxies, International Astronomical Union Colloquium No. 124, edited by J.W. Sulentic, W.C Keel and C.M Telesco, p269.

Steiman–Cameron, T.Y., & Durisen, R.H. 1988, ApJ, 325, 26.

Toomre, A. & Toomre, J. 1972, ApJ, 178, 623.

Yun, Min Su, 1992, Ph.D. Dissertation, Harvard University.

CHAPTER 2

THE KINEMATICS OF THE MOLECULAR GAS IN CENTAURUS A

This work originally appeared in
The Astrophysical Journal 1992, **391**,121.

> **'... Alice started to her feet, for it flashed across her mind that she had never before seen a rabbit with either a waistcoat-pocket or a watch to take out of it, and, burning with curiosity, she ran across the field after it, and was just in time to see it pop down a large rabbit-hole under the hedge.**
>
> **In another moment down went Alice after it, never once considering how in the world she was to get out again.'**
>
> **— Lewis Carroll, *Alice's Adventures in Wonderland***

THE KINEMATICS OF THE MOLECULAR GAS IN CENTAURUS A

A. C. Quillen,[1] P. T. de Zeeuw,[2] E. S. Phinney,[1] and T. G. Phillips[3]
California Institute of Technology

Received 1991 March 14; accepted 1991 September 24

ABSTRACT

The CO (2–1) emission along the inner dust lane of Centaurus A, observed with the Caltech Submillimeter Observatory on Mauna Kea, shows the molecular gas to be in a thin disk, with a velocity dispersion of only about 10 km s^{-1}. The observed line profiles are broadened considerably due to beam smearing of the gas velocity field. The profile shapes are inconsistent with planar circular and noncircular motion. However, a warped disk in a prolate potential provides a good fit to the profile shapes. The morphology and kinematics of the molecular gas is similar to that of the ionized material, seen in Hα. The best-fitting warped disk model not only matches the optical appearance of the dust lane but also agrees with the large-scale map of the CO emission and is consistent with H I measurements at larger radii.

Subject headings: galaxies: individual (NGC 5128) — galaxies: kinematics and dynamics — galaxies: ISM — ISM: molecules

1. INTRODUCTION

As the nearest of all the giant radio galaxies, Centaurus A (NGC 5128) provides a unique opportunity to observe in detail the dynamics and morphology of an active galaxy at a variety of different wavelengths. Because of the prominent disk of dust and gas in its central region, Cen A is suspected to be the product of the merging of a small spiral with a larger elliptical galaxy (Baade & Minkowski 1954). Numerical simulations of galaxy collisions (Hernquist & Quinn 1988, 1989) indeed show shell-like features similar to those observed in the outer parts of Cen A (Malin, Quinn, & Graham 1983). By studying the kinematics and morphology of the dust lane, we may hope to learn how the gas in the AGN becomes nonplanar and misaligned from the host galaxy—as it is observed to be in both radio Seyfert galaxies (Unger et al. 1987; Haniff, Wilson, & Ward 1988) and in radio ellipticals galaxies (Sansom et al. 1987), and as it is inferred from the infrared spectra to be in distant quasars (Sanders et al. 1989).

The dust and gas in Cen A have been traced in a variety of different species and wavelengths, including H I (van Gorkom et al. 1990), Hα (Bland, Taylor, & Atherton 1987, hereafter BTA), CO(1–0) emission and far-infrared (Eckart et al. 1990b), CO(2–1) emission (Phillips et al. 1987), near-infrared emission of stars (Harding, Jones, & Rodgers 1981; Giles 1986) and dust (Joy et al. 1988), and also in absorption against the optical light (Dufour et al. 1979), and at millimeter and radio wavelengths (Gardner & Whiteoak 1976; Eckart et al. 1990a; Seaquist & Bell 1990; Israel et al. 1991). Here we present new and more complete measurements of the ^{12}CO(2–1) emission with somewhat higher angular resolution than the CO(1–0) data of Eckart et al. (1990b).

The optical morphology of the warped dust lane has been modeled as a transient by Tubbs (1980) and as an equilibrium structure in a rotating triaxial galaxy by van Albada, Kotanyi, & Schwarzschild (1982). The observed stellar rotation does not support the latter (Wilkinson et al. 1986). Van Gorkom et al. (1990) interpreted the H I 21 cm data by circular motion in a spherical potential. The twisted Hα velocity field of the dust lane (BTA) has been modeled by putting the gas on tilted rings, i.e., the orbits are circles, but the orbital planes have inclination that varies with radius (Nicholson, Bland, & Taylor 1992). This approach is similar to what has long been customary in studies of H I in spiral galaxies (Bosma 1981; Schwarz 1985; Begeman 1987). Asymmetries and twists in the observed velocity field of a galaxy can also be the result of gas on noncircular orbits, such as occur in a triaxial potential. Bertola et al. (1991) have had success modeling the kinematics of the optical emission line gas in NGC 5077 with a triaxial potential, and Lees (1991) has had similar success modeling the H I emission from NGC 4278. In this paper we explore both kinds of models, as have Staveley-Smith et al. (1990) in their recent study of Michigan 160. Specifically, we attempt to interpret our data with three different sets of models: (1) axisymmetric models with gas in a plane on circular orbits, (2) triaxial models with gas in a plane on noncircular orbits, and (3) axisymmetric models with gas on inclined circular orbits.

Hα emission is detectable in the central regions of Cen A with high spatial resolution (BTA). However, the velocity resolution of the Hα data is lower than that of the CO data. We show that the molecular material (CO) and the ionized material (Hα) are dynamically and geometrically identical systems. Since dynamical time scales in the central region are significantly shorter than they are at the larger radii where 21 cm H I is observed, and since the cooling time scale for molecular material is significantly shorter than for ionized material, we expect the molecular gas to be in a more relaxed configuration, i.e., the kinematics should be determined primarily by the potential of the galaxy and not by the initial conditions of the merger. Furthermore, if the galaxy is triaxial, deviations from circular motion generally are expected to be largest in the central regions (de Zeeuw and Franx 1989, hereafter ZF). If the gas were initially in one plane inclined with respect to the principal plane of the galaxy and is now warped as a result of differential precession (Tubbs 1980), the warp should be most severe in the central regions because the differential precession

---

[1] Theoretical Astrophysics, 151–33, California Institute of Technology, Pasadena, CA 91125.

[2] Postal address: Sterrewacht, Huygens Laboratorium, Postbus 9513, 2300 RA Leiden, The Netherlands.

[3] Downs Laboratory of Physics, 320–47, California Institute of Technology, Pasadena, CA 91125.

rate scales with the rate of change of the angular velocity of the gas, which should be largest at about 1 kpc from the nucleus, where the rotation curve begins to flatten out. As a result, CO provides us with an ideal tracer of the galactic potential and the geometry of the gas in the inner kiloparsec of the galaxy.

In § 2 we present new measurements of the ^{12}CO(2–1) emission along the inner part of the dust lane of Cen A. In § 3 we discuss the thickness of the disk. Our kinematic modeling approach is outlined in § 4, and models with gas on circular orbits in a plane are explored in § 5. In § 6 we relax the assumption of circularity and allow planar elliptic orbits in triaxial potentials. In § 7 we relax the assumption that the gas is in a plane but consider only circular orbits in axisymmetric potentials. We summarize our results in § 8.

2. OBSERVATIONS

Observations of Centaurus A in the $J = 2 \rightarrow 1$ transition of ^{12}CO were made at the Caltech Submillimeter Observatory (CSO) on Mauna Kea in 1989 March and 1991 June. A description of the CSO can be found in Phillips et al. (1987). At a rest frequency of 230 GHz, the beam size is 30″ FWHM. The velocity resolution was 1.3 km s^{-1} over a range of 650 km s^{-1}.

Figure 1 shows the CO(2–1) spectra with a linear baseline removed for 18 positions observed in 1989 March along the dust lane at position angle (PA) −63°.5. The central position coincides with the unresolved continuum source in the nucleus of Cen A (van der Hulst, Golisch, & Haschick 1983). The spacing is a half-beam in the inner part of the dust lane and a full beam at the outermost positions. Displayed along with modeled profile shapes in Figures 4*a*, 5*a*, and 8*a* is a mostly filled 11 by 7 grid of positions centered on the nuclear position observed in 1991 June (see Fig. 8*c* for a picture of beam positions). The spacing is a half-beam along PA 26°.5 and a full beam along PA −63°.5. The data were calibrated both by the usual ambient/chopper technique, and by using IRC +10216 as a reference assuming $T_A^* = 24$ K for IRC +10216 in CO(2–1) as determined by previous observation. The data were divided by the main beam efficiency, $\eta_{\rm MB} = 0.72$, as determined by continuum measurements of planets. Figure 2 shows a position-velocity intensity map for the data in Figure 1. Figure 3 shows an integrated intensity map for the data obtained in 1991 June.

Integration times vary from 2.6 minutes for the 12 inner positions to 5 minutes for the outer positions. Since the data were taken on different nights, there may be a relative pointing offset between individual spectra as large as 8″–10″. We checked our pointing every night by making sure that at the nuclear position, we could clearly see the sharp absorption feature at 550 km s^{-1} against the compact continuum source (Israel et al. 1990; Phillips, Sanders, & Sargent 1990), also observed in H I (van der Hulst et al. 1983) and in other molecular lines (Gardner & Whiteoak 1976; Eckart et al. 1990a; Israel et al. 1991).

3. THICKNESS OF THE GAS DISK

A first glance at the CO(2–1) spectra for the outer positions (profiles at offsets −0.90, 0.44 and 0.90, −0.44 in Fig. 1) reveals sharp edges with width less than 10 km s^{-1}. These steep edges set a limit on the velocity dispersion (effective sound speed) σ of the molecular gas clouds $\sigma < 10$ km s^{-1}. This is substantially lower than the value of ~ 60 km s^{-1} estimated by Eckart et al. (1990b) from their CO(1–0) data (see § 8 for further discussion).

Hydrostatic equilibrium of a gas disk in the equatorial plane of an axisymmetric potential to first order yields

$$\frac{h}{R} = \frac{q\sigma}{v}, \tag{3.1}$$

where v is the velocity at radius R in the disk, h is the density

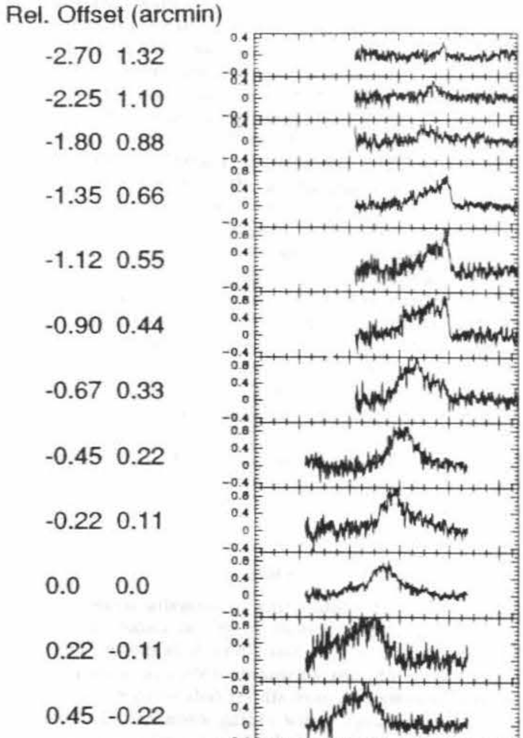

FIG. 1.—^{12}CO(2–1) spectra at PA −63°.5 along the dust lane of Cen A. The vertical axes give the main beam antenna temperature in K. The horizontal axis gives velocity with respect to the local standard of rest, $V_{\rm LSR}$, in km s^{-1}. Relative offsets are in arcminutes from the unresolved H I continuum source (van der Hulst, Golisch, & Haschick 1983) at R.A. = 13^{h}22^{m}31.65, decl. = −42°45′32″.00 (1950).

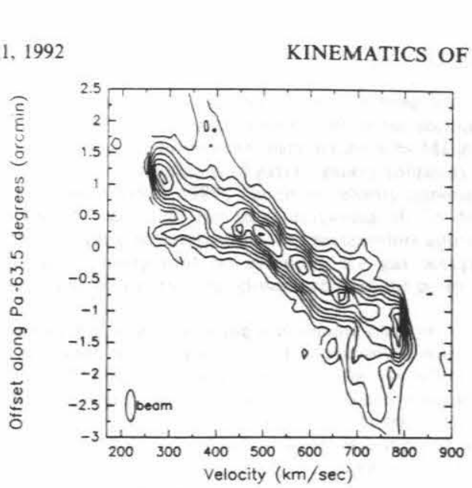

FIG. 2.—Position-velocity intensity map along the dust lane. Relative offsets are along PA −63°.5 from the nucleus of Centaurus A. Velocity resolution has been smoothed to 20 km s^{-1}. Levels begin at 0.1 K with 0.1 K intervals. The 3 σ noise temperature is approximately 0.12 K. Velocity is given with respect to the local standard of rest.

scale height of the disk, and q is the axis ratio of the potential, which, for the nearly spherical systems that we are interested in can be written approximately as a function of $R^2 + z^2/q^2$. Prolate systems have $q > 1$, while oblate systems have $q < 1$. In the central regions of Cen A where the CO is located, $q \sim 1$. Using the peaks of our outer profile shapes, for $R > 60''$ we find a minimum value for v to be 260 km s^{-1} which corresponds to a gas disk at an inclination of 90°. Using this minimum value for v, our limit $\sigma < 10$ km s^{-1} restricts the disk thickness h to less than $h/2''.5$ (35 pc) at $R > 60''$ (900 pc).[4]

Another limit on the thickness of the disk can be obtained from the observation that OB star formation is taking place in the molecular disk at the rate of $\sim 1.6\ M_\odot$ yr^{-1} (Marston & Dickens 1988), so that the disk must be locally Jeans-unstable. This requires (e.g., Binney & Tremaine 1987, eq. [6-49])

$$\frac{\sigma\kappa}{\pi G\Sigma} < 1\,, \tag{3.2}$$

where Σ is the surface density of the disk and κ is the epicyclic frequency. Assuming that the disk is on the limit of stability, and using equation (3.1), then gives

$$h \approx \frac{q\pi G\Sigma}{\Omega\kappa}\,, \tag{3.3}$$

where the angular velocity $\Omega = v/R$. Since galactic disks are observed to lie within a factor of 2–3 of the stability line (Kennicutt 1989), we estimate

$$h < \frac{3q\pi G\Sigma(R = 0)}{\Omega^2(R = 90'')}\,, \tag{3.4}$$

over the range of our data. Whereas it is not evident that Kennicut's result for spiral disks applies to the disk of Cen A, we will show that it is consistent with the observed low velocity dispersion. Here we have used the fact that Σ is largest at $R = 0$, and that $\kappa \sim \Omega$ where the rotation curve flattens. Over the range of our data, Ω is lowest at $R = 90''$. Using $\Sigma(R = 0) = 2\text{–}3 \times 10^8\ M_\odot/[2\pi(60'')^2]$, which is a good fit to the CO(2–1) integrated intensities (Phillips et al. 1987) and $R\Omega = 260$ km s^{-1} (the asymptotic velocity which our data approaches when $R > 60''$) to obtain a lower limit for Ω at $R = 90''$, we find a limit on the thickness of the disk of $h < 25$ pc, and a limit on the velocity dispersion of the gas clouds $\sigma < 7$ km s^{-1}. These limits may be slightly low because we did not consider the fraction of the disk made up of cold (low velocity dispersion) newly formed stars (estimated from the star formation rate to be less than 10%). There should also be corrections of order unity due to the onset of two-fluid instabilities (Jog & Solomon 1984).

The small thickness of the disk that follows from the above arguments is consistent with the conclusion of BTA that the symmetry of their projected velocity field implies that they observe both sides of the disk even though the disk is highly inclined. As BTA conjectured, this is possible only if the disk is thin.

4. KINEMATIC MODELING

Previous attempts at extracting a rotation curve from the gas kinematics of Cen A include fitting the H I velocity field (van Gorkom et al. 1990), and the Hα velocity field (BTA). Van Gorkom et al. (1990) obtained a good fit to their H I data with a rotation curve that results from a model with gas on circular orbits in a spherical galaxy with a light distribution that obeys a de Vaucouleurs law. Nicholson et al. (1992) find good fits to the Hα data of BTA by using an axisymmetric model with a differentially precessing inclined circular disk. Modeling procedures such as these usually compare the data to projected model velocity fields or channel maps (e.g., Begeman 1987; Lees 1991). This is possible because of the sufficiently high spatial resolution (Hα beam $\sim 2''$) and because the data sets fully cover a large area on the sky. In regions where the rotation curve is not linear, the size of the beam also affects measurement of the rotation curve. This effect, known as "beam smearing," can significantly influence the measured shape of the rotation curve even in high-quality H I data (Begeman 1987). Because of the relatively large size of the CSO beam in the CO(2–1) line (FWHM = 30″), the mean velocity at each beam position is a weighted average over a large fraction of the disk and is not very informative. However, the full velocity profile shapes contain much information about the projected velocity field. As a result, we decided to model directly the profile shapes at each position where we took data.

Various authors have estimated the time scale for infalling gas to settle onto the simple closed orbits of a host galaxy to be about 1–3 × 10^9 yr at an effective radius (e.g., Tohline, Simonson, & Caldwell 1982; Habe & Ikeuchi 1985, 1988; Steiman-Cameron & Durisen 1988), but these values are rather

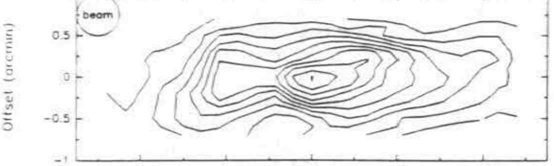

FIG. 3.—Integrated intensity CO(2–1). Contours spaced 10% apart with the lowest contour at 10% of maximum intensity. For a picture of positions observed on the sky, see Fig. 8c.

---

[4] We use 3 Mpc for the distance to Cen A (Tonry & Schechter 1990).

uncertain (de Zeeuw 1990). We note that this time scale is approximately the same as the estimated age of the shell-like stellar features observed in the outer part of Cen A by Malin et al. (1983) and in the simulations of galaxy-galaxy collisions by Hernquist & Quinn (1988, 1989). The small velocity dispersion of the molecular gas, and the small thickness of the disk, suggest that the gas is (nearly) settled, and we therefore approximate the gas velocity field by assuming the gas occupies simple, i.e., non–self-intersecting, closed orbits in the potential of Cen A.

Our procedure consists of doing a simulated observation in which a projected model velocity field is convolved with the beam of the CSO. Around each position on the sky where we have a CO spectrum, we construct a two-dimensional grid. Simultaneously we also make an array of velocity bins. At each position on the grid the line of sight velocity is computed, and a corresponding weight is placed at that location in the velocity bin array. This weight consists of three factors:

1. A factor that depends on the distance between the point of the grid and the center of the beam. For the CSO, a Gaussian representation of the beam is accurate to the 1% level.
2. A factor that depends on the azimuthally averaged intensity of the model disk at that radius. Since the profile shapes on either side of the nucleus are quite similar (see Fig. 4*a*), nonaxisymmetric variations in intensity, such as might be caused by spiral arms, must not be large enough to significantly affect the observed profile shapes. This may be because of the high inclination of the gas disk and the large beam size.
3. A factor which is necessary only for gas either on noncircular orbits or in a warped disk. For gas on closed noncircular orbits (§ 6), this third factor is a surface density correction resulting from the continuity equation and the variation of the gas velocity along the orbit, while for gas in a warped disk (§ 7), this factor depends on the inclination of the gas disk with respect to the line of sight at the point under consideration.

The resulting velocity array is a model profile shape that incorporates the finite size of the CSO beam and can be compared directly to the observations. Since a specific line-of-sight velocity is computed at each position on the grid, not a spread of velocities, we have assumed that the gas disk is infinitely thin and has no velocity dispersion. The limits on the dispersion set in § 3 imply that this should be a very good approximation. The width of the modeled profile shapes results from the finite size of the beam, not the velocity dispersion of the gas clouds.

We discovered that a least mean squared (χ^2) fitting routine is not particularly useful for fitting models to our data. The large number of data points and the numerical nature of the convolution make it time consuming to use a fitting routine which must try out many different models before converging. Although a first glance it seemed that the parameter space was large, we discovered that the fitting is mostly sensitive to two or three parameters, with some of the others heavily constrained by these, and the remaining ones having little influence on the fits. As a result, we manually explored parameter space. Instead of listing formal errors on the derived parameters, we list ranges in which we have found adequate fits to the data. Since our data consist of 57 one-dimensional velocity profile functions, i.e., many hundreds of independent numbers, fitting models requiring 6 to 10 parameters is not unreasonable. Quality of fit was judged both by χ^2 and by consistency with other observations of Cen A such as the position angle of the optical isophotes of the underlying galaxy.

5. CIRCULAR ORBITS IN A PLANE

We start with the simplest models for the CO gas kinematics and assume the gas is on circular orbits in a plane.

5.1. *Rotation Curves*

We examine two families of models with simple rotation curves. The first set has a rotation curve given by

$$v_c(R) = \frac{AR}{(R^2 + c^2)^{1/2}}, \tag{5.1}$$

where A and c are parameters. This rotation curve corresponds to Binney's (1981) logarithmic potential with finite core radius c, and we therefore refer to models of this kind as Binney models. The rotation curve rises linearly in the homogeneous core ($R \ll c$), and asymptotically approaches the value A at large radii, so that the models have infinite total mass. This does not affect our fits because the CO emission is confined to the rising part of the rotation curve. We note that an asymptotically flat rotation curve is not inconsistent with the H I data at larger radii (van Gorkom et al. 1990).

To verify that our conclusions are not unique to models with a finite core radius, we also consider the rotation curve of Hernquist's (1990) spherical model which is a good approximation to a de Vaucouleurs galaxy. In this case the associated density profile diverges as $1/r$ in the center, where r is the spherical radius. The rotation curve is given by

$$v_c(R) = \frac{\sqrt{GMR}}{R + r_0}, \tag{5.2}$$

where G is the gravitational constant, M is the total mass, and r_0 is the scale length of the model. The half-light radius r_e is equal to $1.8153 r_0$. We have replaced r by the cylindrical radius R to indicate that we are interested only in the rotation curve in the equatorial plane ($z = 0$) and do not require that the potential of Cen A is in fact spherical. The rotation curve rises very steeply in the central region ($R \ll r_0$), reaches a maximum at $R = r_0$, and decreases as $1/R^{1/2}$ at large radii.

Figure 4 shows profile shapes, projected velocity field, projected intensity contours, and projected orbits for the Binney model. Though we investigated both models and will discuss both, the profile shapes for the two models are not significantly different, and we include only a figure for the Binney model. The models are normalized such that the peaks of the outer profiles match the peaks of the data; this means adjusting A for the Binney models and M for the Hernquist models. For the Binney models the core radius c was varied also for finding the best fit. For the Hernquist models we could have varied r_0, but we decided to fix it by the observed value of 305″ for the half-light radius of Cen A (Dufour et al. 1979). The intensity of the CO(2–1) disk as a function of radius R in the disk was assumed to be a Gaussian, $\exp(-R^2/2\sigma_s^2)$ with $\sigma_s = 65''$ which is consistent with the observed radial distribution of CO(2–1) (Phillips et al. 1987). V_{sys} was also adjusted. Finally, both the inclination of the disk, ϑ, and the position angle χ of the projected short axis to the gas disk were varied for best fit.

We obtained $V_{sys} = 540 \pm 5$ km s^{-1} with respect to the local standard of rest[5] (532 ± 5 km s^{-1} heliocentric) for both models. The inclination $\vartheta = 80° \pm 3°$, and the position angle of

---

[5] Velocities in this paper are taken to be $(\Delta\nu/\nu_0)c$, where c is the velocity of light, ν_0 is the rest frequency, and $\Delta\nu$ is the frequency shift of the line observed. The difference between our velocity and the optical convention $(\Delta\lambda/\lambda_0)c$ at Cen A is approximately 1 km s^{-1}.

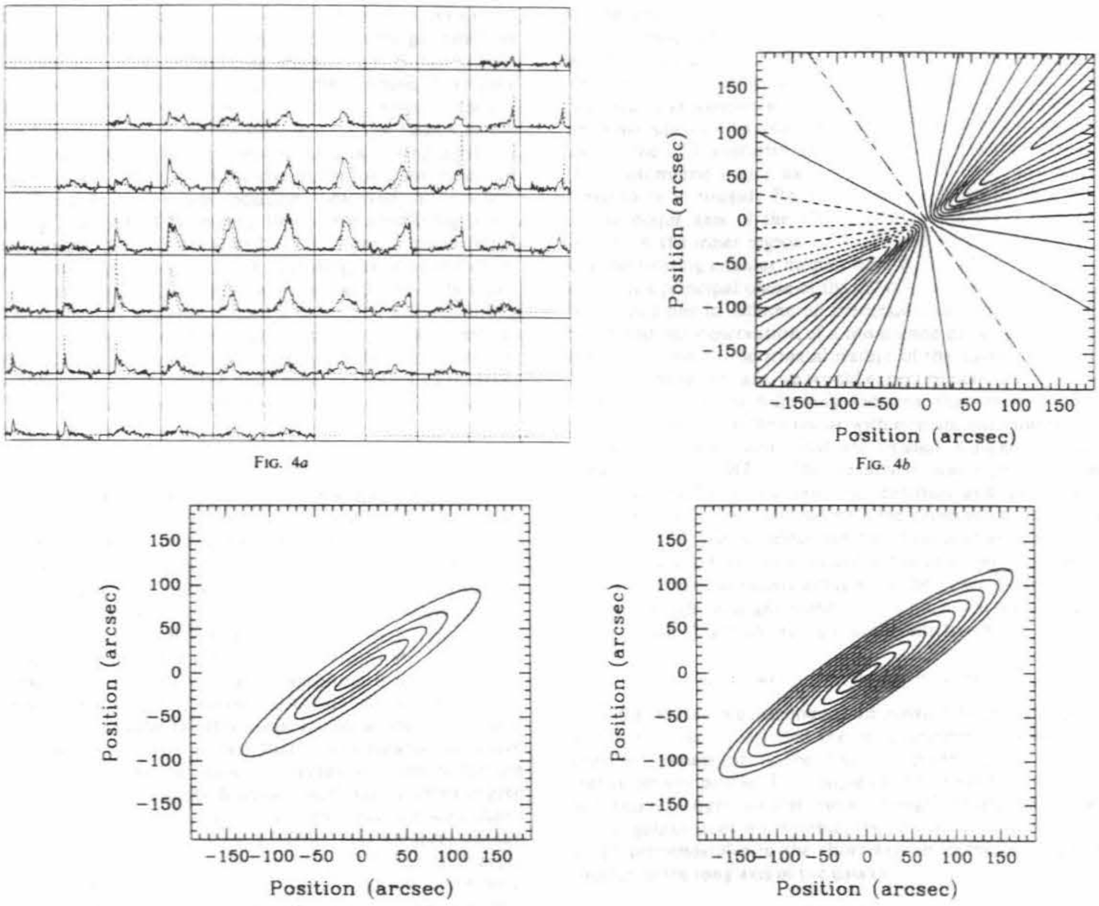

FIG. 4a

FIG. 4b

FIG. 4c

FIG. 4d

FIG. 4.—(*a*) Best-fit model with circular orbits and a Binney rotation curve. Solid lines are the data; dotted lines are the model. Each profile displayed is located at a different position on the sky with the central profile at the nucleus. The spacing is 30" along PA −63°.5 which is the horizontal direction in the figure and is 15" along PA 26°.5 which is the vertical direction in the figure. See Fig. 8*c* for a picture of the beam positions on the sky. The vertical axes give the main beam antenna temperature in K and range from −0.1 to 1.0 K. The horizontal axes give velocity with respect to the local standard of rest, $V_{\rm LSR}$, and range from 170 to 900 km s^{-1}. See text and Table 1 for parameters of the model. (*b*) Projected velocity field. Contours are 25 km s^{-1} apart. The dot-dash contour is at the systemic velocity $V_{\rm sys}$. The dotted contours are at velocities less than $V_{\rm sys}$, and the solid ones indicate velocities larger than $V_{\rm sys}$. (*c*) Intensity contours. Levels are 20% apart and range from 20% to 100% of maximum intensity. (*d*) Projected orbits. Contours are 20" apart and are the radius on the gas plane as seen on the sky. The vertical direction is north.

the short axis of the disk $\chi = 35° \pm 5°$ are constrained tightly. There are no significant differences between the best fits of the two different models. This is not surprising because our spatial resolution is poor; the large beam effectively averages over the range where the two velocity curves are different so that the resulting model profiles differ little.

The parameters of the best-fitting Binney model (Fig. 4) are $A = 290 \pm 20$ km s^{-1} and $c = 40'' \pm 15''$. This corresponds to a mass of $1.1 \times 10^{11}\ M_\odot$ inside 4.5 kpc ($1.2r_e$). The best-fitting Hernquist model has total mass $M = 2.8 \times 10^{11}\ M_\odot$. For the assumed value of r_0, this gives $1.3 \times 10^{11}\ M_\odot$ inside $1.2r_e$. These masses agree with that derived by van Gorkom et al. (1990) by fitting a velocity curve appropriate for a de Vaucouleurs law to the H I data. We find as they do, that the rotation curve in this region is consistent with a roughly constant mass-to-light ratio which is approximately 3 in solar units. Since our CO(2–1) measurements do not extend beyond 1.5 kpc, the above result merely confirms that the CO velocities are consistent with the H I velocities measured at larger radii, a result which is evident on comparing the position-velocity diagrams for both species directly.

5.2. *Temperature and Filling Factor*

Our value for the inclination of the disk allows us to estimate T_n, the temperature that would be observed if a plane of gas that is at uniform velocity with respect to the observer and is of the same temperature and filling factor as the disk were observed face-on.

$$T_n = f_a T_c = \frac{\cos \vartheta}{A(v)} T(v) , \tag{5.3}$$

where $T(v)$ is the antenna temperature observed at velocity v, $A(v)$ is the fractional area of the beam covered by gas emitting at this velocity, T_c is the average temperature of the clouds from which the disk is formed, and f_a is the effective area filling factor of these clouds. We have $f_a = f_v h/r_c$, where f_v is the volume filling factor of the gas clouds, r_c is the radius of the typical cloud and h is the thickness of the disk. Using equation (5.3) we estimate $f_a T_c \approx 1.2$ K for the central position observed and $f_a T_c \approx 0.3$ K for the position observed at $r = 60''$. Assuming $T_c \approx 10$ K (Eckart et al. 1990b), the area filling factor f_a then ranges from 0.03 to 0.12, with slightly lower filling factors for $r > 60''$. For a thin disk, f_a is roughly the same order as f_v, so that these values are consistent with the hypothesis that the molecular material of Cen A is clumpy and has filling factor and average cloud temperature similar to the molecular material of our Galaxy. Such a low filling factor implies that it is possible to see through the disk, even at inclinations larger than 80°. This is consistent with the hypothesis of BTA that the Hα disk is optically thin.

5.3. *Defects of Circular Orbit Models*

It is clear from the fit shown in Figure 4 that our method of modeling the profile shapes is a promising one. The overall profile shapes can be reproduced reasonably well by convolving a projected model velocity field with the CSO beam. The widths of the profile shapes can be reproduced with only a small cloud velocity dispersion. However, there are a number of discrepancies in detail. We discuss them in turn.

Inspection of Figure 4 reveals that positions 30″ to the east and west of the nucleus have mean velocities further from the systemic velocity than observed, although the Binney model fits slightly better than the Hernquist model at these positions. This is due in part to the fact that c was treated as a free parameter for the Binney model, whereas we fixed r_0 for the Hernquist model. Thus, the Binney model has an extra degree of freedom to match the radius at which the velocity curve rounds off. Possibly, the rotation curves that we have chosen are too steep in the central region and do not round off sharply enough. However, significantly changing the shape of the rotation curve would not be consistent with the observation that the radial intensity in the infrared (K) of the central region follows a de Vaucouleurs law to within 1″–2″ of the nucleus (Giles 1986; Frogel, Quillen, & Graham 1992).

The velocity centroids of positions to the north and south of the nucleus are reproduced incorrectly by the circular models. As is clear from the projected velocity field in Figure 4*b*, the models have mirror symmetry with respect to two axes. The zero velocity curve, i.e., the contour at the systemic velocity, is a straight line. The maximum velocity curve is also a straight line, which is perpendicular to the zero velocity line. This is true for any flat circular disk, so changing the rotation curve will not improve the fit at these positions.

The intensities of positions to the north and south of the nucleus are higher than those produced by the models. This could be because we have overestimated the FWHM of the intensity as a function of radius on the disk, or because the inclination of the models is too high. It is impossible to correct for these effects with the circular models since lowering the inclination makes the profile shapes at positions in the inner part of the disk too thin, and increasing the FWHM of the intensity curve makes the profile shapes at positions to the east and west of the nucleus too large.

The position angle χ of the short axis of the gas disk is 35° for the best circular fits. This coincides with the position angle ϑ_s of the photometric major axis of Cen A, which is measured in the optical by fitting ellipses to the isophotes for $70'' < R < 255''$ to be at $\vartheta_s = 35 \pm 3°$ (Dufour et al. 1979). Although our kinematic fit is consistent with placing the disk perpendicular to this axis, neither the dust lane nor the major axis of the CO isophotes are observed to be perpendicular to the photometric major axis. Optically the dust lane is measured to be at roughly PA 116°, whereas the position angle ϑ_d of the major axis of the CO intensity contours varies from $\sim 116°$ in the inner region to $\sim 125°$ beyond 70″ (see Fig. 3). Our best-fitting circular models have $\vartheta_d = 125°$. Either the gas is not in a principal plane of the galaxy, in which case it would be warped due to differential precession, or it is in a principal plane and our observation of a misaligned gas disk is a projection effect due to the triaxial nature of the galaxy (e.g., Stark 1977). In the latter case, we would expect noncircular motions.

We show in the following sections that models with a warped geometry of the disk or with noncircular motions have projected velocity fields that are twisted, similar to what is observed in Hα (BTA). This results in wider profile shapes, systematic shifts in the velocity centroids and gas intensity contours that are not aligned with the projected principal axes of the galaxy. Nevertheless, we find that planar models even with noncircular motions cannot fit the observed CO line profiles while simultaneously explaining the observed orientation of the starlight and gas isophotes. With a warped model, by contrast, we obtain an excellent and predictive fit.

6. NONCIRCULAR ORBITS IN A PLANE

In this section we investigate the possibility that the gas is in a principal plane, and that the misalignment discussed in the previous paragraph is the result of projection of a triaxial stellar density profile. The simple closed orbits for the cold gas are then no longer circular, but are roughly elliptic. If the figure of the galaxy does not tumble, the orbits can lie either in the plane perpendicular to the short axis or in the plane perpendicular to the long axis of the galaxy.

6.1. *Mass Models and Viewing Angles*

We have used two different kinds of triaxial models. The first are separable (Stäckel) models, which are typical of models with homogeneous cores. The simple closed orbits are exact confocal ellipses, and the velocity field can be given by simple analytic expressions (ZF). In the core, the confocal ellipses become highly elongated, and the closed orbit approximation for the gas kinematics becomes unphysical. The specific mass models we have used are the $p = 1$ members of the family described in Appendix B of ZF. In the axisymmetric limit, their rotation curve reduces to that of the Binney model, given in equation (5.1).

The second set of models is defined by taking the potential of the spherical Hernquist model and adding two spherical harmonic terms with a radial fall-off such that the associated density becomes triaxial with roughly elliptic isophotes (see Appendix). The detailed properties of the models are given in Lees & de Zeeuw (1991, hereafter LZ). These models again have a central cusp, and the axis ratios in the center and at large radii can be chosen freely. The closed orbits can be calculated with first-order epicyclic theory (e.g., Gerhard & Vietri 1986) and reach a finite elongation in the center. This approximate description is sufficiently accurate for moderately flattened mass models (LZ), specifically those with axis ratio less than 0.5 on the plane in which the gas is located.

Three viewing angles are needed to specify the orientation of a triaxial galaxy. We choose Cartesian coordinates (x, y, z) along the three principal axes of the system, and we assume the gas is in the (x, y)-plane. Following the convention of ZF (see their Fig. 2), we take ϑ and φ as the usual spherical polar angles of the line of sight, so that as in § 5, ϑ is the inclination of the gas plane, i.e., the angle between the line of sight and the z-axis. For $\vartheta = 0°$ the disk is face-on, and for $\vartheta = 90°$ the disk is edge-on. The angle χ is again the position angle on the sky of the projected z-axis, measured from the north.

We remark that ZF defined the long axis of the galaxy to be always in the x-direction and the short axis to be in the z-direction, and then discussed models with gas in the (x, y)-plane and models with gas in the (y, z)-plane separately. By contrast, we assume the gas is always in the (x, y)-plane and vary the axis ratios of the galaxy (see also Bertola et al. 1991). If a, b, and c denote the semi-axes along the x, y, and z directions, respectively, then ZF have $a > b > c$ always, but we consider both $a > b > c$ and $c > a > b$.

For a triaxial system with ellipsoidal surfaces of constant density, the apparent axis ratio b'/a' of the projected surface density, and the value of Θ^*, the position angle difference between the apparent major axis and the direction of the zero velocity curve at large projected radii, are both functions of the intrinsic axis ratios b/a and c/a and the viewing angles ϑ and φ. ZF (Appendix A) have shown that for given viewing angles ϑ and φ, the observed values of Θ^* and b'/a' may be used to calculate explicitly the corresponding axis ratios b/a and c/a. Once these are known, the gas velocities can be calculated. Thus, in order to fit the velocity fields, we vary the same parameters as for the circular models: A and c for the separable models, and M for the modified Hernquist models. Measurement of Θ^* is difficult from the Hα velocity field, because the zero velocity line is noisy, and because the zero velocity line may not converge asymptotically to a straight line over the scale of this map, though we estimate $\Theta^* = -5° \pm 20°$. As a result Θ^* was among the parameters varied. Also varied were the angles ϑ and χ, and the axis ratio of the potential on the (x, y) (gas) plane. The observed value for b'/a' then fixed the other axis ratio and φ. In addition, for both types of models, the systemic velocity $V_{\rm sys}$ is varied.

6.2. *Triaxial Models with Constant Ellipticity*

Although the optical isophotes of the inner part of Cen A are observed to be round (Dufour et al. 1979), the near-infrared K isophotes have axis ratios of $b'/a' = 0.8$ to within 70″ of the center. Van den Bergh (1976) has suggested that star formation in the disk is responsible for the rounding of the optical isophotes. We first set $b'/a' = 0.8$ and postpone a discussion of models with changing ellipticity to § 6.3.

Gas clouds on closed noncircular orbits are not uniformly distributed around each orbit, because the equation of continuity $\nabla \cdot \Sigma_g \boldsymbol{v} = 0$, where Σ_g is the surface density of the gas, and $\boldsymbol{v}$ is the velocity vector, requires the surface density to vary. We assume that the intensity is proportional to Σ (nonoverlying clouds) and compute the azimuthal variation of Σ_g from the equation of continuity (see ZF, eq. [2.12]). Σ is assumed to decline as a Gaussian function of the semimajor axis of the orbits (see § 5.1), with dispersion $\sigma_s = 60''$.

Figure 5 displays our best-fit Stäckel model, which has $A = 300 \pm 10$ km s^{-1} and $c = 40'' \pm 15''$, and axis ratios $a:b:c = 1:2:2.6$, so that the model is prolate/triaxial. The best-fitting viewing angles are $\chi = 37° \pm 5°$, $\vartheta = 80° \pm 3°$, $\varphi = 20° \pm 8°$. Furthermore, $V_{\rm sys} = 538 \pm 5$ km s^{-1} with respect to the local standard of rest ($V_{\rm sys} = 541 \pm 5$ km s^{-1} heliocentric). The peculiar intensity contours in the center of the model (Fig. 5*c*) are caused by the unphysical nature of the closed orbit approximation in the center (ZF). Since this effect is averaged over the center beam and affects only the center data position, it does not significantly influence our profile shapes or fits, and we ignore it. Figure 6 is our best-fit modified Hernquist model. Only the projected velocity contours and intensity contours are shown since the modeled profile shapes are very similar to those of the Stäckel model. The angular parameters are identical to the parameters for the separable model. The total mass within 4.5 kpc for these models is roughly the same as that of the circular models discussed in § 5.

When gas is on noncircular orbits, there is a component of the velocity in the direction toward the center of the galaxy. When the line-of-sight velocity is compared with that of a circular orbit, this component has the effect of increasing the line-of-sight velocity on two quarters of the orbit and decreasing it on the others. The angle φ determines which part of the orbit has increased line-of-sight velocity. The models with low φ, in which the orbits are seen roughly broadside-on, produce the best fits because the ellipticity of the orbits reduces the velocities at positions to the east and west of the nucleus. Compared with the circular orbit models of § 5, the noncircular model improves the fit at these positions. However, the fit at positions to the northwest and southeast of the nucleus is not improved. Although these models provide no better global fits than the circular model, they are more consistent with other observations of Cen A which are discussed in the following paragraphs.

For our best fits the position angle of the isophote major axis $\vartheta_s = 32°$ is consistent with that observed, $\vartheta_s = 35° \pm 3°$ (Dufour et al. 1979). This implies that the potential axes are at the same orientation in the inner region of the galaxy where there is CO emission as they are in the outer region where the starlight isophote axes can be measured. This is consistent with the fact that no isophote twist has been observed in Cen A.

The position angle ϑ_d of the major axis of the gas isophotes (Figs. 5*c* and 6*b*) of the model is $\sim 125°$ for $R > 60''$, as in the circular models, but in addition ϑ_d twists to a lower position angle in the central regions ($R < 60''$) as observed (see Fig. 3). However, in the central regions, ϑ_d is observed to be 116°, whereas the model has $\vartheta_d \sim 121°$. Although the noncircular orbit model matches the observations in the outer part as well as the circular orbit models do, and qualitatively matches the observations in that ϑ_d becomes lower in the central regions, it does not agree completely with the observations. This could be because we have used too simple a model for the intensity as a function of radius (a molecular ring would also change the observed angle of disk isophotes in the center).

There are a few qualitative features of interest in these noncircular models. The zero-velocity line (the systemic velocity contour on the projected velocity contour plots) in these models is curved and not aligned with the position angle of the axis perpendicular to the gas plane on the sky (see Figs. 5*b* and 6*a*), whereas for the circular models, the zero-velocity line is straight and aligned with the projected short axis of the disk. The maximum velocity curve for the noncircular models is not perpendicular to the zero velocity curve. Since the velocity field does not have mirror symmetry, there is a higher density of

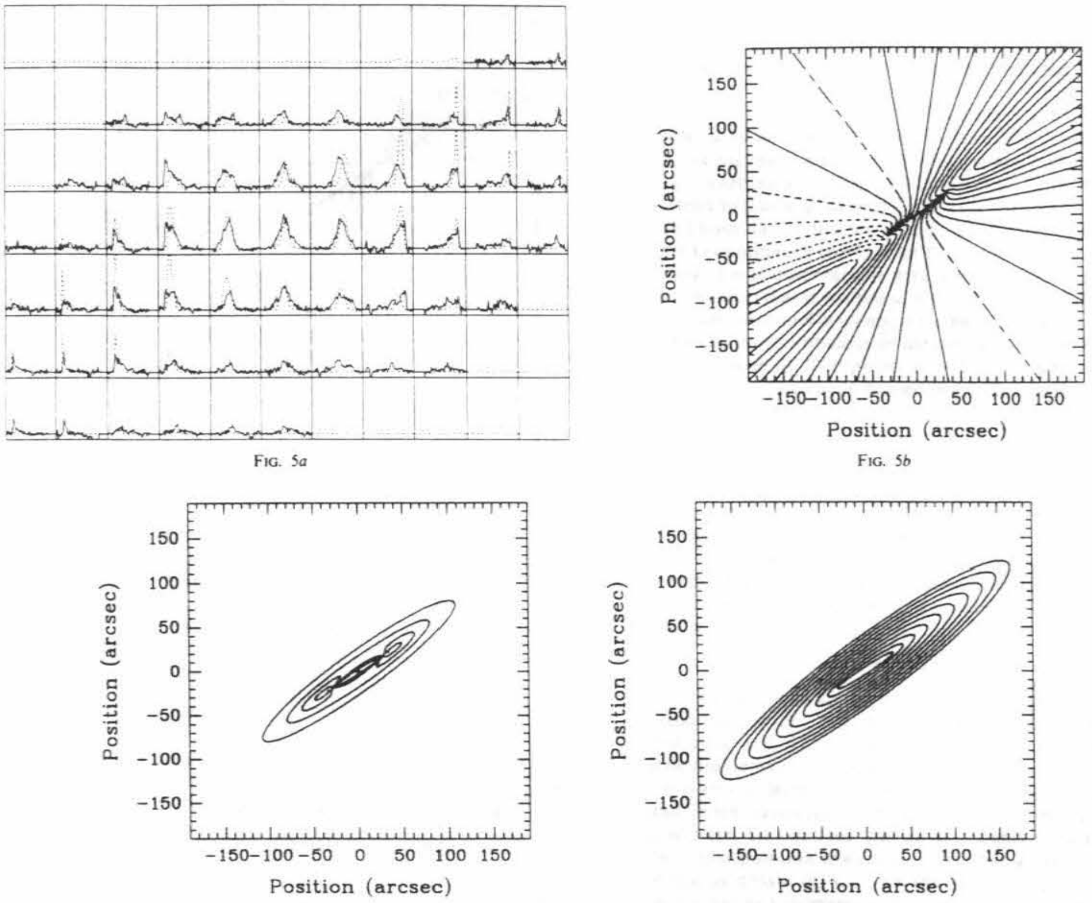

FIG. 5a

FIG. 5b

FIG. 5c

FIG. 5d

FIG. 5.—Best-fit triaxial Stäckel model. (*a*) Profiles. (*b*) Projected model velocity field. (*c*) Model intensity contours. (*d*) Projected closed orbits for the gas. See Fig. 4 legend, Table 1, and text for further details.

contours per unit area of the velocity field. Because of this, each beam sees a larger velocity range, and the profile shapes are slightly wider. Unfortunately, most of the effects of noncircular motion are masked in Cen A by the high inclination of this particular system. This is because most of the twisting of the velocity field contours is concentrated in a small area on the sky, so that the effects of the noncircular motion are averaged away by the finite resolution of observation. Large deviations from circular motion would be more apparent in a system with a less inclined gas disk.

6.3. *Triaxial Models with Changing Ellipticity*

Changing the axis ratios of the triaxial model as a function of radius such that the isophotes become flatter with increasing radius makes the closed orbits for the gas more circular in the center and less circular in the outer regions of the gas disk. The resulting maximum velocity line will curve out further away from the minor axis of the galaxy in the outer region. We therefore investigate the possibility that a model with changing ellipticity could account for the curved maximum velocity line observed in Hα (BTA) and to see if our profile shapes can be better fit with such a model.

We use the modified Hernquist models so that the effects of the changing ellipticity in the central region are not obscured by the unphysical nature of the Binney models in this region. We set Θ^* to be constant, so that the isophotes do not twist, and vary the observed b'/a' as a function of radius. We find that the maximum velocity line for these models does indeed twist. A slightly twisted maximum velocity curve could be modeled by a triaxial model with changing axis ratios, though a severely twisted one cannot be modeled this way. Thus these models are qualitatively right, but none of them have a twist in the maximum velocity line as large as that observed in the Hα data. No model was found that fits our data better than the modified Hernquist models of § 6.2. The higher the inclination of the system, the less freedom there is to model twists in the velocity contour map as a triaxial system with gas on noncircular orbits (assuming that the axis ratios of the triaxial system are all greater than 0.3). This is because at high inclination, the twisting of the velocity field is concentrated in a much smaller area on the sky.

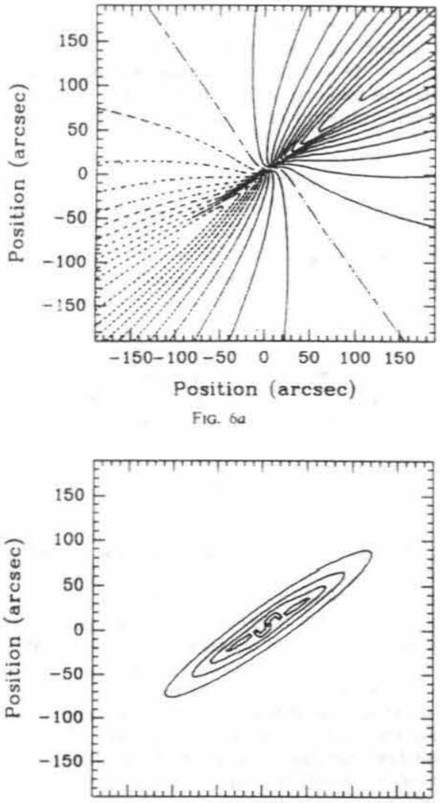

FIG. 6a

FIG. 6b

FIG. 6.—Best-fit modified Hernquist model. (*a*) Projected model velocity field. (*b*) Model intensity contours.

7. WARPED DISKS

In this section we return to axisymmetric models, but relax the constraint that the gas lie in the equatorial plane, and consider warped configurations.

7.1. *Tilted Rings*

For gas close to the equatorial plane in a moderately flattened axisymmetric potential, we can think of a warp as a set of smoothly connected inclined rings, where each ring is centered on the nucleus of the galaxy with radius r the distance from the nucleus (e.g., Sparke 1986). We describe the geometry and orientation of the warp with four angles, two of which are a function of r. We again use the angles χ and ϑ to describe the orientation of the axisymmetric potential. We denote by z' the rotational axis of symmetry of the ring at radius r, and let ω be the angle between the z- and the z'-axis. We define α to be the angle in the equatorial plane of the projection of z' onto this plane minus the angle of the projection of the line of sight (see Fig. 7). A disk which was once in a single plane inclined with respect to the principal plane of the potential will at a later time have undergone differential precession. If there has not been settling onto the principal plane of the potential, then at this later time ω will be constant and α will vary as a function of r.

Previous work on fitting a collection of tilted rings to kinematic data involved simultaneously fitting continuous curves for the inclination and the precession angle as a function of r (e.g., Begeman 1987; Staveley-Smith et al. 1990). We attempted instead to find a set of simple curves for $\alpha(r)$ and $\omega(r)$ so that we can fit our data with a few parameters instead of fitting $\alpha(r)$ and $\omega(r)$ as continuous curves. Our first experiment was to see if we could fit our observations with a disk of constant inclination (ω constant) that is warped as a result of differential precession. This simple model is identical to the one used by Tubbs (1980) to model the morphology of the optical dustlane. In an axisymmetric potential of ellipticity $\epsilon_p = 1 - 1/q$, where q is the axis ratio of the potential as defined in § 3, the precession rate $d\alpha/dt$ is approximately

$$\frac{d\alpha}{dt} \sim \frac{\epsilon_p v}{r} . \tag{7.1}$$

The precession is prograde for a prolate potential ($q > 1$) and is retrograde for an oblate potential ($q < 1$). Assuming that the disk is initially in a plane at constant inclination [$\omega(r)$ constant], and that there is minimal settling onto the principal plane, minimal inflow, and ϵ_p is constant as a function of time, after a time Δt

$$\alpha(r) = \epsilon_p \Omega \Delta t + \alpha_0 . \tag{7.2}$$

If this model is to apply, the direction of the warp on the Hα projected velocity field (see BTA, Fig. 5 and Plate 2) implies that $d\alpha/dr < 0$. This assumes that the axis of symmetry of the potential (z-axis) is pointing toward us, where the direction of the z-axis is determined by ensuring that the rotation of the disk when projected on to the equatorial plane is counterclockwise. This implies that for Ω roughly constant and with the z-axis pointing toward us, either the galaxy in the central region is oblate ($\epsilon_p < 0$), or the galaxy is prolate and ϵ_p is decreasing as r increases so that $d\epsilon_p \Omega/dr < 0$ over the range of the Hα data. We consider two types of models: oblate models

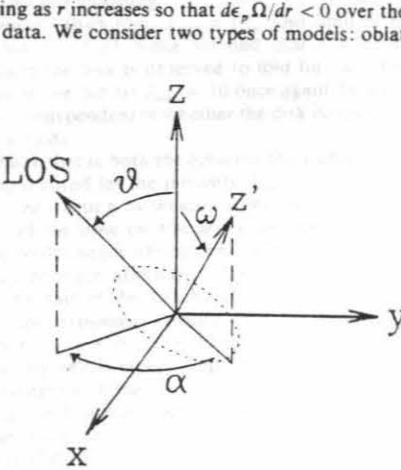

FIG. 7.—Definition of angles used in the warped disk models. The x, y, and z axes principal axes of the potential. The z' axis is the axis of symmetry of the ring represented by the dotted ellipse. LOS is the line of sight. See text for further details.

with constant ϵ_p and prolate models with $\epsilon_p = \epsilon_\infty[1 - \exp(-r^3/\sigma_e^3)]$, where σ_e is a parameter that we can roughly estimate from the infrared (K) isophote axis ratios, $40'' < \sigma_e < 80''$ (Frogel et al. 1992). We used a cubic exponential because we did not obtain good fits to our data with smoother, less steep functions.

7.2. *Projected Velocity Field*

Changing coordinates from the coordinate system of the gas disk to sky coordinates consists of doing four rotations, one for each of the angles χ, ϑ, $\alpha(r)$, and $\omega(r)$. This angle $i(r)$ between the axis of rotation z' for a disk of radius r and the line of sight is given by

$$\cos i = \cos \vartheta \cos \omega - \cos \alpha \sin \vartheta \sin \omega \,, \tag{7.3}$$

where $\cos i$ is the component of the z'-axis in the direction of the line of sight. Note that $i(r)$ is not the inclination of the surface. The projection of the z'-axis on the sky is at position angle $\beta(r)$ given by

$$\sin(\beta - \chi) = \frac{\sin \alpha \sin \omega}{\sin i} \,. \tag{7.4}$$

The zero-velocity line of the projected velocity field is the set of points $[r \sin i(r), \beta(r)]$, where $r \sin i(r)$ is the distance on the projected velocity field from the point to the nucleus and $\beta(r)$ can be read off as the position angle of the vector from the nucleus to the zero-velocity point on the sky. The maximum velocity line on the projected velocity field is the set of points $[r, \beta(r) + (\pi/2)]$. Information about the inclination of z' as a function of r can be found by matching points on the maximum velocity line and the zero-velocity line that are perpendicular to each other on the projected velocity field. Specifically, if $D(r)$ is the distance to points on the zero-velocity curve that are perpendicular to points on the maximum velocity curve that are r away from the nucleus, then $D(r)/r = \sin i(r)$. If the disk is folded with respect to the line of sight (see below), accurately measuring $D(r)$ may be difficult since the zero velocity line may loop; in other words, it is possible that $dD(r)/dr < 0$. It may also be difficult to locate accurately the maximum velocity line since it too may be obscured by the folding of the disk and the finite resolution of the observed projected velocity field. We note that these equations will not be accurate for gas on noncircular orbits.

For a potential with nonzero inclination ($\vartheta \neq 0$) and a gas disk with $\omega(r) \neq 0$ and varying $\alpha(r)$, generally the line of sight intersects the disk more than once. If the gas is clumpy with a low filling factor, we will see through the gas disk to other parts of the disk. In fact, splitting of the Hα line (emission from different places of the disk at one position on the sky) has been observed in the Hα spectra of Cen A (BTA). In order to generate profile shapes, it is therefore necessary to convolve the beam of the CSO with each fold of the disk separately, since clouds on different folds contribute independently to the profiles. As described in § 4, the algorithm for convolving the beam with the projected velocity field involves assigning the projected velocity field at each point on the sky a weight consisting of three factors. The first two factors are identical to those used in § 4. The third factor is necessary for a disk with changing inclination, and equals the Jacobian $J = \partial(x, y)_{\rm disk}/\partial(x, y)_{\rm sky}$, where $(x, y)_{\rm disk}$ is a local Cartesian coordinate system on the disk and $(x, y)_{\rm sky}$ is a Cartesian coordinate system on the sky. A point at which the line of sight is tangent to the surface of the disk has $1/J = 0$. A locus of such points will form a boundary, where on one side of the boundary the line of sight will intersect the disk two more times than on the other side of the boundary. Since J diverges at these points, it is necessary to use a cutoff $J \leq J_{\rm max}$, where $J_{\rm max}$ is the maximum intensity that a disk can have at the points where it folds.

We observed that models with $J_{\rm max} > 20$ produced spikes in the profiles that were not observed in our data set. These spikes resulted from the large intensities from the points at which the disk folded over as seen from the line of sight. This maximum allowable value for $J_{\rm max}$ allows us to put limits on the thickness of the disk or on the filling factor of the disk, depending upon whether the folds are optically thick (meaning that it is not possible to see through them) or optically thin. At a fold of curvature r, the line of sight intersects the disk with length approximately $(rh)^{1/2}$. The disk will be observed to be optically thick when the intersection of the line of sight with the disk is approximately of length h/f_a, where f_a is the effective area filling factor of the gas clouds of the disk, and h is the thickness of the disk. By comparing these two lengths we see that

$$f_a^2 < h/r \,, \tag{7.5}$$

if the disk is to be optically thin at the folds. Using our previous estimates for h and f_a discussed in §§ 3 and 5.2, $0.03 < f_a < 0.12$, we find that the disk is optically thin at the folds. However since these estimates are not very accurate, it is possible that the folds are optically thick, though since f_a is low, it is likely that the disk is optically thin everywhere else. Therefore, we discuss both cases.

For optically thin folds $J_{\rm max} \approx (r/h)^{1/2}$. Our limit $J_{\rm max} < 20$ implies that $r/h < 400$ which gives us a lower limit for h, the thickness of the disk, and σ, the velocity dispersion of the gas clouds making up the disk, $h > r/400$ or $\sigma > v/400$ for r where there are folds at positions where we took data. Our limit of $J_{\rm max} = 20$ is equivalent to antenna temperatures of ≈ 23 K. Since the maximum temperature at these points cannot be greater than the expected temperature of the clouds themselves which we estimated to be ≈ 10 K (§ 5.2), we adopt the limit $J_{\rm max} = 10$ for our modeling.

For optically thick folds $J_{\rm max} \approx 1/f_a$. Our limit of $J_{\rm max} < 20$ implies that $f_a > 1/20$. Since we find that $f_a \approx 0.1$ over the region where the disk is observed to fold for our models (see Figs. 8 and 9), we can set $J_{\rm max} = 10$ once again. In this way our modeling is independent of whether the disk is optically thin or thick at the folds.

We remark that in both the optically thick and optically thin case, using a cutoff for the intensity $J_{\rm max}$ is an approximation. However, the fraction by which the intensity is overestimated is small and the area on the sky where this occurs is small compared to our beam size, so that the modeled profile shapes should not be much affected by this approximation. Obscuration of one part of the disk by another will cause an asymmetry in the projected velocity field: in other words the symmetry $r \to -r$, $v \to -v$ will be broken. Since the Hα projected velocity field is highly symmetrical, this effect cannot be large, consistent with the low covering factor and high clumpiness we derive. For more detailed models, it will be necessary to take into account obscuration of one part of the disk by other parts of the disk.

7.3. *Oblate and Prolate Models*

Using equations (7.3) and (7.4), rough constraints and starting points for fitting the CO profiles can be found from the Hα

projected velocity field. At the radius r_z where the maximum velocity line crosses the line on the sky perpendicular to χ, $\alpha(r_z)$ is either 0 or 180° and

$$\vartheta + \omega(r_z) \cos \alpha(r_z) = i(r_z) . \tag{7.6}$$

At the radius r_m where angle between the maximum velocity line and χ is smallest, $\alpha(r_m) = \pm 90°$, and

$$\vartheta = i(r_m) \quad \text{and} \quad \beta(r_m) = \omega(r_m) . \tag{7.7}$$

Applying these constraints to the Hα velocity field, we find that $r_z \sim 100''$, $r_m \sim 60''$, and for $\omega(r)$ constant we find that $\omega = \beta(r_m) = \vartheta - i(r_z) \sim 25°$ and $\vartheta = i(r_m) \sim 60°$. We used these values as starting points for fitting and to solve for $\epsilon_p \Delta t$, and α_0 for our models.

For our tilted ring models, we used the Binney velocity curve (eq. [5.1]) with $c = 40''$ and we took χ to be $35° \pm 5°$. The parameters in common with the circular models of § 5 were chosen to be roughly the same values as those for the best-fit circular models. See Table 1 for comparison of models with Binney rotation curves. Figure 8 displays our fit for a prolate model with $\epsilon_p = \epsilon_\infty[1 - \exp(-r^3/\sigma_e^3)]$, where σ_e was varied for best fit. Where the line of sight intersects the disk more than once, the velocity displayed in the projected velocity field of Figure 8*b* is the intensity-weighted average of the velocity of each point intersected. The intensity shown in Figure 8*c* is the sum of the intensities at each point of the disk intersected by the line of sight. For the oblate model, the best fit was found for $\vartheta = 60° \pm 7°$, $\omega = 25° + 5°$, $r_z = 100''$, $r_m = 50''$ and $\sigma_s = 65''$. For the prolate model, $\vartheta = 60° \pm 7°$, $\omega = 25° \pm 5°$, $r_z = 90''$ and $120''$, $r_m = 53''$, and $\sigma_s = 80''$. For both models, $\chi = 35° \pm 5°$, $A = 290$ km s^{-1}, $c = 40''$, and $V_{\rm sys} = 538$ km s^{-1} with respect to the local standard of rest (541 km s^{-1} heliocentric). Using equation (7.2), we found $\epsilon_p \Delta t = -1.2 \times 10^7$ yr and $\alpha_0 = 131.^\circ 8$ for the oblate model with ϵ_p constant, and $\epsilon_\infty \Delta t = 2 \times 10^7$ yr and $\alpha_0 = -182°$ for the prolate model with $\epsilon_p = \epsilon_\infty[1 - \exp(-r^3/\sigma_e^3)]$ and $\sigma_e = 80''$. Since the infrared isophotes in the central region of the galaxy ($r < 60''$) are not significantly flattened, the ellipticity of the potential in this region must be very small. For an oblate model with $\epsilon_p = -0.01$ or axis ratio $q \approx 0.99$, $\Delta t = 1.2 \times 10^9$ yr. For a prolate model with $\epsilon_\infty = 0.2$, roughly equivalent to an axis ratio $1/q = b'/a' = 0.8$ as observed from the optical isophotes, we found $\Delta t = 1 \times 10^8$ yr. This time scale agrees with that estimated by Tubbs (1980). These models have a mass of $1.1 \times 10^{11} M_\odot$ inside 4.5 kpc which is the same as that of the circular models discussed in § 5 and that derived by van Gorkom et al. (1990).

TABLE 1

BEST-FIT MODELS WITH BINNEY ROTATION CURVES

PARAMETER	GEOMETRY AND ORBITS		
	Planar, circular	Planar, noncircular	Warped, circular
$V_{\rm sys}$ (km s^{-1})[a]	540 ± 5	538 ± 5	538 ± 5
ϑ	80° ± 3°	80° ± 3°	60° ± 7°
φ	...	20° ± 8°	...
θ[a]	...	−5°	...
b/a	...	0.5	...
χ	35° ± 5°	37° ± 5°	35° ± 5°
A (km s^{-1})	290 ± 20	300 ± 20	290 ± 20
c	40" ± 15"	40" ± 15"	40" ± 15"
σ_s	65"	60"	80"
σ_e	...	...	80"
α_0	...	...	−182°
$\epsilon_\infty \Delta t$ (yr)	...	...	2 × 10^7
ω	...	...	25° ± 5°

[a] $V_{\rm LSR}$.

We note that for a plane at an angle ω from the principal plane the contours of constant potential have ellipticity $\sim \epsilon_p \sin^2 \omega$, so that the orbits of the gas on this plane for both the oblate and prolate model with $\omega = 25°$ should be very nearly circular, so that our approximation of circular orbits is accurate for these models.

7.4. *Discussion*

Since we obtained good fits using models whose constraints are taken from the Hα data, we conclude that the dynamics and geometry of the molecular material is identical to that of the ionized material seen in Hα. Specifically, our best-fit prolate model (Fig. 8) fits the data surprisingly well. There are some differences which can be mostly explained by pointing errors in the data. Differences may also be caused by nonaxisymmetric variations in intensity on the disk such as might by caused by spiral arms. The parameters for this model were determined initially by fitting to the data obtained in 1989 March which consisted only of positions along the major and minor axes of the dust lane. The additional data obtained in 1991 June at the request of the referee fit remarkably well without adjustment of parameters; in fact, we were unable to improve the quality of the fit by adjusting the parameters. This gives confidence in the predictive power of the model. The best-fit oblate model (not displayed) fit the data well only in the inner regions (less than 60" from the nucleus). Use of a rotation curve without a core (eq. [5.2]) does not improve the fit to the data in the central regions. Models with lower α_0 fit better in the center than models with higher α_0, though they fit the data in the outer regions less well. By using a more accurate model for $\alpha(r)$, a model which fits the data better everywhere could be made. However, in order to do this, we would need to know better $\epsilon_p(r)$, the rotation curve, and the intensity as a function of radius. Even with models with lower α_0, there remain high-velocity tails in the data in the positions 0"–30" from the nucleus that were not present in the model profiles (these tails were also observed by Israel et al. 1990, 1991). As a result, there may be a dynamically independent system in the central region of Cen A. One possible explanation for this could be a circumnuclear disk (Israel et al. 1990, 1991), which would be responsible for the higher velocity wings of the central positions.

Steiman-Cameron & Durisen (1988) showed that the inclination $i(t)$ of a gas disk that is settling in a scale-free potential is given by

$$i(t) = i_0 \exp(-t/\tau_e)^3 , \tag{7.8}$$

where i_0 is the initial inclination, and τ_e is the settling time scale,

$$\tau_e = \left(\frac{v}{6}\right)^{-1/3} \left(\frac{\partial \dot{\alpha}}{\partial r}\right)^{-2/3} , \tag{7.9}$$

where v is the coefficient of kinematic viscosity $v = \alpha_v \sigma h$, $\dot{\alpha}$ is the precession rate (see eq. [7.1]) and $\alpha_v \approx f_a$ for clouds with low area filling factor f_a (Goldreich & Tremaine 1983). We note that in the inner regions ($r < 50''$), the potential is not scale free. However, the time scale for settling should be close to that of

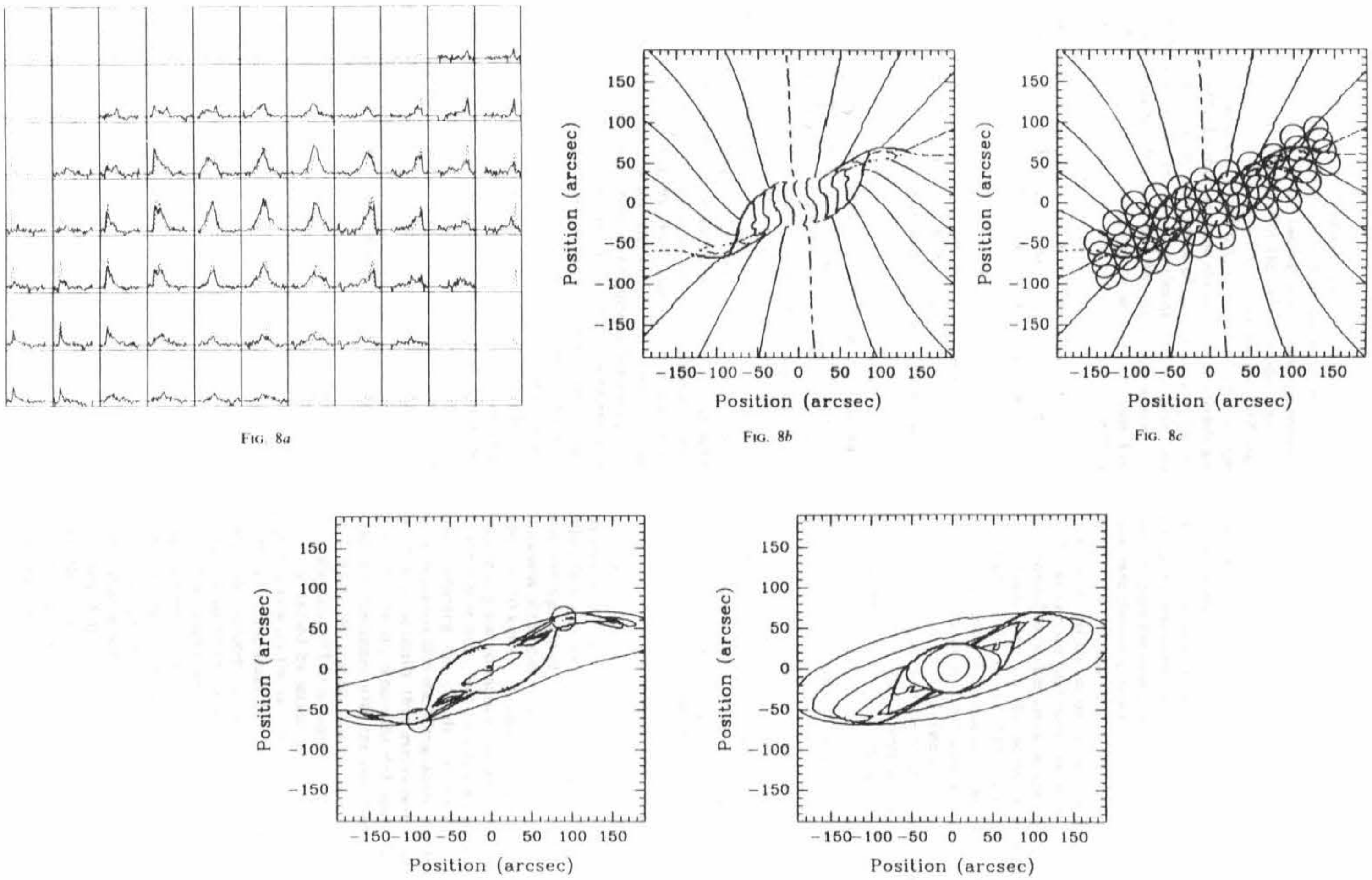

FIG. 8*a*

FIG. 8*b*

FIG. 8*c*

FIG. 8*d*

FIG. 8*e*

FIG. 8.—Inclined ring model for a prolate potential with ellipticity $\epsilon_p = \epsilon_\infty [1 - \exp(-r^3/\sigma_e^3)]$. (*a*) Profiles. (*b*) Projected model velocity field. Contours are 50 km s^{-1} apart. (*c*) Beam positions superposed on the projected velocity field. (*d*) Intensity contours. Contours are at 2%, 6%, 18%, and 26% of maximum intensity level (determined by $J_{\max}$; see text for details). The small circles represent the approximate location of the peaks of the H I column density distribution (van Gorkom et al. 1990). (*e*) Projected orbits.

equation (7.9), and the inclination (eq. [7.8]) should settle exponentially though probably not to the third power of t. We estimated this time scale by taking the velocity dispersion $\sigma \approx 10$ km s^{-1} and $\alpha_v \approx 0.1$. For the oblate model with constant ellipticity $1.6 \times 10^9 < \tau_e < 4 \times 10^9$ yr for $r < 100''$, and for the prolate model $6 \times 10^8 < \tau_e < 1.2 \times 10^9$ yr over the same region where the shortest time scales for both models are at $r \approx 40''$. Since Δt is the same order of magnitude as τ_e for the oblate model with constant ϵ_p, a significant amount of settling should have occurred. We conclude that this model is inconsistent with the initial condition of gas on an inclined plane. For an oblate model with a lower ellipticity, and longer settling time scale (so that the disk would not have settled onto the principal plane of the potential), Δt would be larger than 10^9 yr, which seems rather long compared with the likely age of the merger. In order to consistently model the warp in an oblate potential, the inclination of the warp as a function of radius $\omega(r)$ would have to be modeled as well as $\alpha(r)$. However, $\Delta t < \tau_e$ for the prolate model, so this model is consistent with our initial hypothesis that the warp is the result of differential precession of gas that was initially on a plane with respect to the principal plane of the potential. We note that even though settling at this time scale may not have taken place, there may have still been a significant amount of inflow, which could have affected the shape of the warp. In addition we suspect that the rounding of the ellipticity of the potential in the central region of the galaxy may be a result of the gas disk falling into the center of the galaxy. The ellipticity of the central regions may not only be a function of radius but also of time. A more detailed model would have to take these factors into account.

In order to compare our prolate model with the large scale CO emission (Fig. 3), we made an integrated intensity map from our model (see Fig. 9). Note that the resemblance to Figure 3 is good, including an extension to the lowest contour level roughly 140″ on either side of the nucleus. We notice that the intensity of our model on the sky is primarily determined by the inclination of the surface of the warp, not by the surface density of the disk as a function of distance from the nucleus. Peaks in the emission can be located simply where there are folds in the disk. Figure 9 has peaks at $\approx 50''$ on either side of the nucleus. Similar features were also observed by Eckart et al. (1990b) in the CO(1–0) integrated intensity map. These features, which resemble the intensity contours of a molecular ring, may also be caused by the changing inclination of the warped molecular disk. The excess emission observed at the nucleus which is not present in the model is due to higher velocity wings which have been interpreted as evidence for a circumnuclear disk (Israel et al. 1990, 1991).

The overall shape of the intensity contours coincides both with the location of the optical dust lane and the H I emission. The two small circles in Figure 8c, at 109″ from the nucleus, indicate the locations of the peaks of the H I column density distribution (see Fig. 3 of van Gorkom et al. 1990), and they coincide nicely with the warp. The position angle of the H I emission on either side runs approximately east-west and so follows our intensity contours. We note that the overall shape of the model intensity distribution coincides with the optical dust lane as well. Because of its low filling factor, a significant fraction (dependent on the inclination of the disk) of the starlight behind the disk is visible. The optical appearance of the dust lane therefore depends on the transmission of the disk, as well as on its location in the galaxy. Figure 10 shows an overlay of this model on an optical image of Cen A (Graham 1979) we can see that portions of the disk at high inclination correspond to darker areas on the south side of the dust lane. Absorption seen on the north side cannot be due to gas described by this model. There is a fold in the disk at roughly 12″ to the south of the nucleus. This fold, which is nearer to us than the nucleus, is observable as a line of absorption in the near-infrared (J and H) (see Joy et al. 1991, Fig. 1). The Hα emission is brighter on the northern side of the dust lane (BTA) because there is less absorption on this side, rather than because the northern side is closer to us.

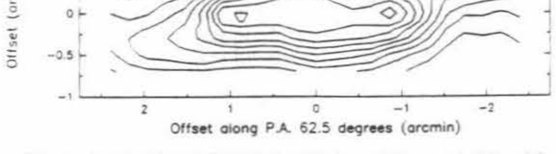

FIG. 9.—Integrated intensity contours for the prolate model of Fig. 8 for comparison with Fig. 3. Contours are at the same levels as in Fig. 3.

Finally, we note that although one of the three molecular absorption lines observed against SN 1986G by d'Odorico et al. (1989) correspond to the line-of-sight velocity of our modeled warp at the location of the supernova, the other two do not. As these authors discuss, it may be possible for a warped model, when extended out to radii beyond 300″, to match the velocities of these absorption lines. Since our CO data do not extend beyond 120″, our best-fitting model cannot be applied with any confidence at such large radii.

8. SUMMARY AND CONCLUSIONS

Using a rough estimate of the inclination of the disk ($\sim 80°$) derived from the best-fit circular models, we estimate the area filling factor of the molecular disk $0.03 < f_a < 0.12$ for $R < 60''$ and average cloud temperatures ≈ 10 K. We find that the thickness of the disk is less than 35 pc, and the velocity dispersion $\sigma < 10$ km s^{-1}. Using the Jeans stability limit for a disk undergoing star formation, we were able to extend these limits to the whole disk. Not only is the disk surprisingly thin and cold (meaning the clouds composing it have low velocity dispersion) but also the filling factor is so low that the molecular disk is optically thin everywhere except possibly at the points on the sky where the disk folds. Both of these conclusions are consistent with the observed Hα projected velocity field (BTA). We suspect that the Hα measurement of the velocity dispersion (BTA) is higher than our limit because of line blending caused by seeing more than one fold of the disk at each position on the sky. We note that they did observe line splitting in some areas. Eckart et al. (1990b) may have overestimated the velocity dispersion necessary to reproduce the CO(1–0) data for the same reason (see § 3).

In § 5 we found that circular orbits in a plane do not fit our data particularly well. Models of this kind are inconsistent with the observed position angles of the axes of the CO isophotes and the optical isophotes. In § 6 we discussed planar noncircular models (gas on the principal plane in a triaxial potential). With these models, we were not able to improve our fits to the data, though the alignment of the axes of the predicted and observed CO isophotes and the optical isophotes is somewhat improved by using these models. Allowing the ellip-

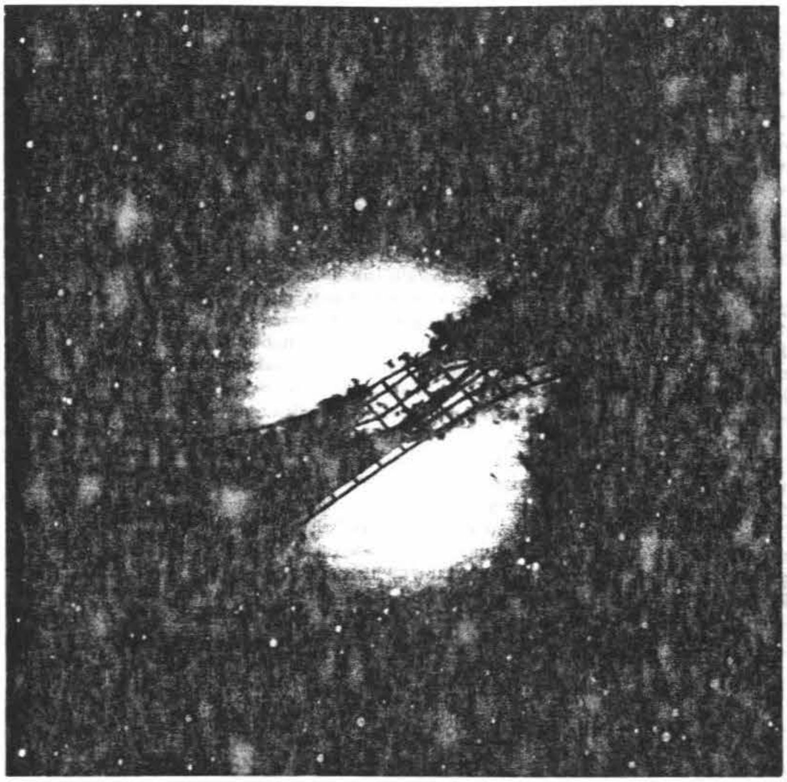

FIG. 10.—Overlay of the prolate model of Fig. 9 on an optical image of Cen A (Sandage 1961). The fold in the disk about 12″ south of the nucleus is observable as the line of absorption in the near-infrared (*J* and *H*) (see Joy et al. 1991, Fig. 1).

ticity of the potential to change as a function of distance from the nucleus does not improve the fits, although qualitatively such models have many of the same features that are observed in the Hα projected velocity field.

In § 7 we derived a simple model for a disk that has evolved from a planar system as a result of differential precession (Tubbs 1980). Using constraints derived from the Hα data we were able to find starting points for fitting. Because this was successful, we conclude that the ionized material seen in Hα is dynamically and geometrically identical to the molecular material observed in CO. Our best-fit model with an oblate potential is inconsistent with our initial assumptions (the gas should have settled onto the principal plane of the potential at the time scale needed in order to form the warp). In addition, the fit to the data for this model in the outer regions (more than 60″ from the nucleus) is not good. Our best-fit model with a prolate potential with ellipticity varying as a function of radius (Fig. 8) fits the data well and also shows agreement with the CO(2–1) integrated intensity contour map. Convolution of the intensity map of our model produces peaks in the integrated intensity contours that were observed by Eckart et al. (1990b) in CO(1–0). These features are not caused by a molecular ring or hole in the CO material in the center of the galaxy, but are caused by the changing inclination of the disk. The peak of the H I emission lands on the highest intensity contours of our warp model, and the intensity contours also follow the shape of the optical contours of the dust lane. Areas of the disk at high inclination correspond to darker areas of the dustlane as observed optically. There is a fold in the disk of our model roughly 12″ to the south that is coincident with the line of absorption in the near-infrared (*J* and *H*) observed by Joy et al. (1991). Wilkinson et al. (1986) found that an effectively stationary prolate model such as ours is consistent with their observation of the stellar velocity field of Cen A if the jet direction is not associated with an axis of symmetry of the galaxy. For this model, the inclination of the major axis of the potential is 60° ± 7° with the gas at an angle of 25° ± 5° above the equatorial plane of the potential, with the southern side nearest to us. This model would be tested further by comparison with a more spatially filled and more extended data set in CO(2–1), with higher resolution in CO(3–2) and by modeling the Hα data cube of BTA.

Since our warped model consists of clouds in circular orbits, it is not possible to obtain absorption lines at velocities other than the systemic velocity against the nuclear compact continuum source from the material in the warped disk. We note that it is possible that the gas disk is not only warped (not on a principal plane plane with respect to the potential), but that the potential is triaxial in which case the orbits of the gas could be significantly noncircular. In this case, one expects absorption lines against the nucleus at velocities that are either higher or lower than the systemic velocity, depending upon the direction of viewing. Because of numerous high-density molecular absorption lines and high-velocity wings in observed CO lines at the central positions in Cen A (Israel et al. 1991), it is more likely that there is a dynamically distinct system in the nucleus.

Gas warps, like the one we find in Cen A, may be responsible for much of the infrared emission from AGNs (Phinney 1989; Sanders et al. 1989). They may also provide a more dynamically plausible alternative to thick tori (Krolik & Begelman 1988) as a means of hiding the soft (but not the hard) X-ray emission (Koyama et al. 1989; Warwick et al. 1989) and the broad-line region of type II Seyfert and narrow-line radio galaxies. Morganti et al. (1990) have shown that the optical filaments of Cen A must be photoionized by a nuclear continuum source that is either hidden or highly anisotropic. These authors furthermore find that if this nuclear continuum is relativistically beamed, then Cen A may have beam power similar to that of BL Lac. Our best-fitting warp (consistent with both CO and infrared data) does not obscure the center of Cen A. Thus a torus or warped disk at radii much less than 20″ (300 pc) from the center seems required to obscure the active center of Cen A. There may also be gas outside the scale of our model ($r > 90''$) that obscures the nucleus.

The time scale estimated to create the warp is 10^8 yr. This time scale roughly agrees with that originally estimated by Tubbs (1980) for a transient warp. A more detailed model with a more accurate rotation and ellipticity curve which includes settling, inflow, and possible changing ellipticity as a function of time may somewhat alter the time scale. Since this time scale is shorter than the time scale from the initial galaxy-galaxy collision as estimated from the location of the thin stellar shells seen in the outer parts of the galaxy ($[2 \times 10^8]$–$[6 \times 10^8]$ yr; Malin et al. 1983), we suggest that the process of the merger be modeled to estimate the time scale for a small galaxy to sink into the center of a larger elliptical and to see in detail the state of the dust after this occurs. Improvements in numerical methods and hydrodynamical codes in the past decade might make reexamination of these issues fruitful. We suspect that the impact parameter and angle of impact of the initial collision can be estimated from the stellar rotation that has been observed at larger radii (beyond 5′ from the nucleus) as determined from the radial velocities of planetary nebulae (Ford et al. 1989; Hui 1990), whereas the angular momentum vector and mass of the colliding spiral galaxy can be estimated from the molecular material in the center since no settling can have taken place on that time scale. With this knowledge, it should be possible to reconstruct the process of the merger.

It is a pleasure to thank Bharat Ratra and Ewine van Dishoeck for comments on the manuscript. We also acknowledge useful discussions with Robert Emmering, Connie Walker, Curt Cutler, and Garrett Biehle. We also acknowledge the anonymous referee whose detailed comments helped to improve the presentation of this paper. This research was supported in part by NSF grant AST 88-15132, NASA grants NAGW-2144 and NAGW-2142, and the Alfred P. Sloan Foundation (E. S. P.).

APPENDIX

MODIFIED HERNQUIST MODEL

Hernquist (1990) has introduced a simple spherical mass model with a projected surface density that closely resembles a de Vaucouleurs law and hence is useful for description of elliptical galaxies. Here we present a triaxial modification of this model, by defining its gravitational potential in spherical coordinates (r, θ, ϕ) as

$$V(r, \theta, \phi) = u(r) - v(r) Y_2^0(\theta, \phi) + w(r) Y_2^2(\theta, \phi) , \qquad \text{(A1)}$$

with $Y_2^0 = 3/2 \cos^2 \theta - 1/2$ and $Y_2^2 = 3 \sin^2 \theta \cos 2\phi$ the usual spherical harmonics. We choose

$$u(r) = -\frac{GM}{r + r_0} , \qquad v(r) = -\frac{GMr_1 r}{(r + r_2)^3} , \qquad w(r) = -\frac{GMr_3 r}{(r + r_4)^3} , \qquad \text{(A2)}$$

where $r_0, \ldots, r_4$ are constants, G is the gravitational constant, and M is the total mass of the model. The function $u(r)$ is the potential of the spherical Hernquist model.

The parameter r_0 is a density scale length, which can be related to the radius R_e which contains half of the projected surface density. In the spherical limit $R_e = 1.8153 r_0$. The remaining four parameters can be expressed in terms of the axis ratios of the density distribution at small and at large radii, where the surfaces of constant density are approximately ellipsoidal, i.e., $\rho \sim \rho(m^2)$ with $m^2 = x^2 + (y^2/p^2) + (z^2/q^2)$. The density falls off as $1/r^4$ at large radii and diverges as $1/r$ in the center.

At large radii, the modified Hernquist potential becomes Keplerian, and the closed orbits are nearly circular. At small radii, the potential becomes scale-free, and the orbits near the (x, y)-plane reach a limiting ellipticity ϵ given by

$$\epsilon = \frac{6(1 - p_0)}{1 + p_0 + 2q_0} \qquad \text{(A3)}$$

where p_0 and q_0 are the central values of the axis scale lengths p and q.

REFERENCES

Baade, W., & Minkowski, R. 1954, ApJ, 119, 215
Begeman, K. 1987, Ph.D. thesis, Rijksuniversiteit, Groningen
Bertola, F., Bettoni, D., Danziger, I. J., Sadler, E. M., Sparke, L. S., & de Zeeuw, P. T. 1991, ApJ, 373, 369
Binney, J. J. 1981, MNRAS, 196, 455
Binney, J., & Tremaine, S. 1987, Galactic Dynamics (Princeton: Princeton University Press)
Bland, J., Taylor, K., & Atherton, P. D. 1987, MNRAS, 228, 595 (BTA)
Bosma, A. 1981, AJ, 86, 1791
d'Odorico, S., di Seregho Alighieri, S., Pettini, M., Magain, P., Nissen, P. E., & Panagia, N. 1989, A&A, 215, 21
de Zeeuw, P. T. 1990, in Dynamics and Interactions of Galaxies, ed. R. Wielen (Berlin: Springer), 263
de Zeeuw, P. T., & Franx, M. 1989, ApJ, 343, 617 (ZF)

Dufour, R. J., van den Bergh, S., Harvel, C. A., Martins, D. H., Schiffer, F. H., Talbot, R. J., Talent, D. L., & Wells, D. C. 1979, AJ, 84, 284

Eckart, A., Cameron, M., Genzel, R., Jackson, J. M., Rothermel, H., Stutzki, J., Rydbeck, G., & Wiklind, T. 1990a, ApJ, 365, 522

Eckart, A., Cameron, M., Rothermel, H., Wild, W., Zinnecker, H., Rydbeck, G., Olberg, M., & Wiklind, T. 1990b, ApJ, 363, 451

Ford, H. C., Ciardullo, R., Jacoby, G. H., & Hui, X. 1989, in IAU Symp. 131, Planetary Nebulae, ed. S. Torres-Peimbert (Dordrecht: Reidel), 335

Frogel, J., Quillen, A. C., & Graham, J. R. 1992, in preparation

Gardner, F. F., & Whiteoak, J. B. 1976, MNRAS, 175, 9P

Gerhard, O. E., & Vietri, M. 1986, MNRAS, 223, 377

Giles, A. B. 1986, MNRAS, 218, 615

Goldreich, P., & Tremaine, S. 1982, ARA&A, 20, 249

Graham, J. A. 1979, ApJ, 232, 60

Habe, A., & Ikeuchi, S. 1985, ApJ, 289, 540

———. 1988, ApJ, 326, 84

Harding, P., Jones, T. J., & Rodgers, A. W. 1981, ApJ, 251, 530

Haniff, C. A., Wilson, A. S., & Ward, M. J. 1988, ApJ, 334, 104

Hernquist, L. 1990, ApJ, 356, 359

Hernquist, L., & Quinn, P. J. 1988, ApJ, 331, 682

———. 1989, ApJ, 342, 1

Hui, X. 1990, talk presented at Aspen Workshop on Structure and Dynamics of Galaxies

Israel, F. P., van Dishoeck, E. F., Baas, F., de Graauw, Th., & Phillips, T. G. 1991, A&A, 245, L13

Israel, F. P., van Dishoeck, E. F., Baas, F., Koornneef, J., Black, J. H., & de Graauw, Th. 1990, A&A, 227, 342

Jog, J. C., & Solomon, P. M. 1984, ApJ, 276, 114

Joy, M., Harvey, P. M., Tollestrup, E. V., Sellgren, K., McGregor, P. J., & Hyland, A. R. 1991, ApJ, 366, 82

Joy, M., Lester, D. F., Harvey, P. M., & Ellis, H. B. 1988, ApJ, 326, 662

Kennicutt, R. C., Jr. 1989, ApJ, 344, 685

Koyama, K., Inoue, H., Tanaka, Y., Awaki, H., Tanako, S., Ohashi, T., & Matsuoka, M. 1989, PASJ, 41, 731

Krolik, J. H., & Begelman, M. C. 1988, ApJ, 329, 702

Lees, J. F. 1991, in Warped Disks and Inclined Rings around Galaxies, ed. S. Casertano, F. Briggs, & P. Sackett (New York: Cambridge Univ. Press), 50

Lees, J. F., & de Zeeuw, P. T. 1991, in preparation

Malin, D. F., Quinn, P. J., & Graham, J. A. 1983, ApJ, 272, L5

Marston, A. P., & Dickens, R. J. 1988, A&A, 193, 27

Morganti, R., Robinson, A., Fosbury, R. A. E., di Serego Alighieri, S., Tadhunter, C. N., & Malin, D. F. 1991, MNRAS, 249, 91

Nicholson, R. A., Bland-Hawthorne, J., & Taylor, K. 1992, 387, 503

Phillips, T. G., et al. 1987, ApJ, 322, L73

Phillips, T. G., Sanders, D. B., & Sargent, A. I. 1990, in Submillimetre Astronomy: Proc. of Kona Symposium, ed. G. D. Watt & A. S. Webster (Dordrecht: Kluwer), 223

Phinney, E. S. 1989, in Theory of Accretion Disks, ed. F. Meyer, W. J. Duschl, J. Frank, & E. Meyer-Hofmeister (Dordrecht: Kluwer), 457

Sandage, A. 1961, The Hubble Atlas of Galaxies (Washington: Carnegie Institution of Washington)

Sanders, D. B., Phinney, E. S., Neugebauer, G., Soifer, B. T., & Matthews, K. 1989, ApJ, 347, 29

Sansom, A. E., et al. 1987, MNRAS, 229, 15

Seaquist, E. R., & Bell, M. B. 1990, ApJ, 364, 94

Schwarz, U. J. 1985, A&A, 142, 273

Sparke, L. S. 1986, MNRAS, 219, 657

Stark, A. A. 1977, ApJ, 213, 368

Staveley-Smith, L., Bland, J., Axon, D. J., & Davies, R. D. 1990, ApJ, 364, 23

Steiman-Cameron, T. Y., & Durisen, R. H. 1988, ApJ, 325, 26

Tohline, J. E., Simonson, G. F., & Caldwell, N. 1982, ApJ, 252, 92

Tonry, J. L., & Schechter, P. L. 1990, AJ, 100, 1794

Tubbs, A. D. 1980, ApJ, 241, 969

Unger, S. W., Pedlar, A., Axon, D. J., Whittle, M., Meurs, E. J. A., & Ward, M. J. 1987, MNRAS, 228, 671

van Albada, T. S., Kotanyi, C. G., & Schwarzschild, M. 1982, MNRAS, 198, 303

van den Bergh, S. 1976, ApJ, 208, 673

van der Hulst, J. M., Golisch, W. F., & Haschick, A. D. 1983, ApJ, 264, L37

van Gorkom, J. H., van der Hulst, J. M., Haschick, A. D., & Tubbs, A. D. 1990, AJ, 99, 1781

Warwick, R. S., Koyama, K., Inoue, H., Tanako, S., Awaki, H., & Hoshi, R. 1989, PASJ, 41, 739

Wilkinson, A., Sharples, R. M., Fosbury, R. A. E., & Wallace, P. T. 1986, MNRAS, 218, 297

> **'... "Well!" thought Alice to herself, "after such a fall as this, I shall think nothing of tumbling down stairs! How brave they'll all think me at home! Why, I wouldn't say anything about it, even if I fell off the top of the house!" (which was very likely true.)'**
>
> **— Lewis Carroll, *Alice's Adventures in Wonderland***

CHAPTER 3

THE WARPED DISK OF CENTAURUS A IN THE NEAR INFRARED

A.C. Quillen,[1] *James R. Graham,*[2,3] *Jay. A. Frogel*[4]

Accepted for Publication in
The Astrophysical Journal
July 20, 1993 issue

---

[1] Theoretical Astrophysics, 130-33, California Institute of Technology, Pasadena, CA 91125

[2] Astronomy Dept., University of California, Berkeley, CA 94720

[3] Alfred P. Sloan Research Fellow

[4] Ohio State University, Dept. Astronomy, 174 W. 18th Ave., Columbus, OH 43210

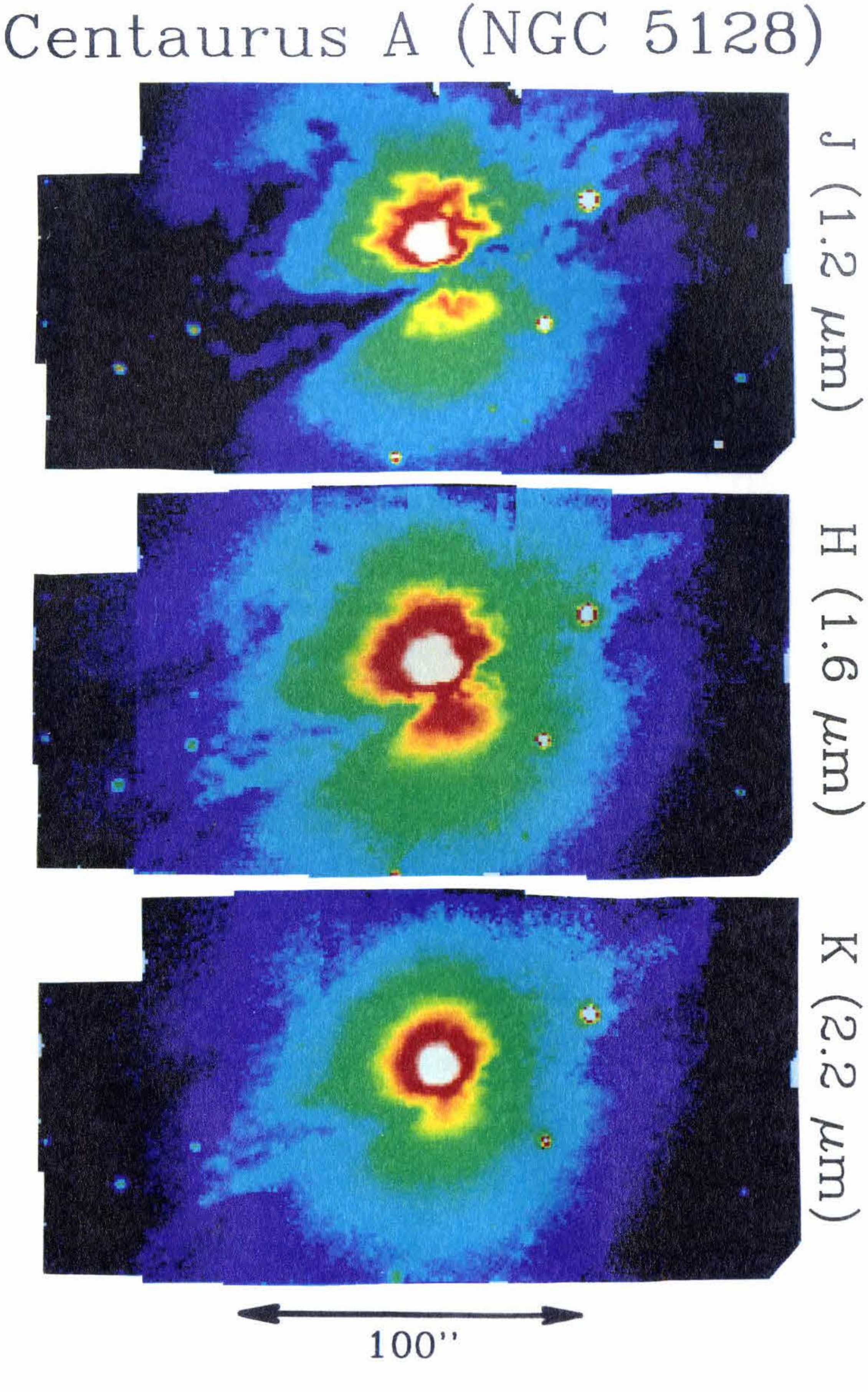
Centaurus A (NGC 5128)
J (1.2 μm)
H (1.6 μm)
K (2.2 μm)
100''

' "Curiouser and curiouser!" cried Alice (she was so much surprised, that for the moment she quite forgot how to speak good English). "Now I'm opening out like the largest telescope that ever was! Good-bye feet!" '

— Lewis Carroll, *Alice's Adventures in Wonderland*

ABSTRACT

We present infrared images of Cen A (NGC5128) in the J,H, and K bands. The infrared morphology is primarily determined by the presence of a thin absorptive warped disk. By integrating the light of the underlying prolate galaxy through such a disk, we construct models which we compare with infrared and X-ray data. The geometry of the warped disk needed to fit the IR data is consistent with a warped disk which has evolved as a result of differential precession in a prolate potential. The disk has an inclination, with respect to the principal axis of the underlying elliptical galaxy, that is higher at large radii than in the inner region.

A scenario is proposed where a small gas rich galaxy infalling under the force of dynamical friction is tidally stripped. Stripping occurs at different times during its infall. The orientation of the resulting gas disk depends upon the angular momentum of the infalling galaxy. We find that the resulting precession angle of the disk is well described by the precession model, but that the inclination angle may vary as a function of radius. We propose an orbit for the infalling galaxy that is consistent with the geometry of the warped disk needed to fit our infrared data, rotation observed in the outer part of the galaxy and the location of the stellar shells in the same region.

Subject headings: galaxies: individual (NGC 5128) – galaxies: kinematics and dynamics – galaxies: ISM – ISM: dust

1. INTRODUCTION

The nearest of all the giant radio galaxies,[5] Centaurus A (NGC 5128, Cen A), provides a unique opportunity to observe the dynamics and morphology of an active galaxy at a variety of different wavelengths. Because of the disk of gas and dust in its central region, Cen A is suspected to be the product of the merging of a small gas rich spiral galaxy with a larger elliptical galaxy (Baade and Minkowski 1954). Shell–like features predicted in numerical simulations of galaxy collisions (Hernquist and Quinn 1988,1989) have actually been observed in Cen A over a large range of distance from the nucleus (Malin, Quinn and Graham 1983). Evidence of merging is correlated to activity in radio galaxies; for example, the two nearest radio galaxies (Cen A and Fornax A) have both shell–like stellar features and gas. Powerful radio galaxies appear to be in regions of higher galaxy density than less powerful ones (Heckman *et al.* 1985). Many of them have complicated optical morphologies displaying features such as tidal tails, fans, shells and dust features (Heckman *et al.* 1986). By studying the kinematics and morphology of the dust lane of Cen A, we may hope to learn how a merger could have caused the overall appearance of Cen A.

The dust and gas in Cen A have been traced in a variety of different wavelengths and species over a large range of radii from the nucleus, including HI (van Gorkom *et al.* 1990), Hα (Bland, Taylor and Atherton 1987), CO(2-1) (Phillips, *et al.* 1987, Quillen *et al.* 1992 hereafter QZPP), near-infrared (Giles *et al.* 1986, Joy *et al.* 1991, Turner *et al.* 1992), far infrared (Eckart *et al.* 1990, Marston and Dickens 1988 and Joy, Lester, Harvey and Ellis 1988), in absorption against the optical light of the inner region (Dufour *et al.* 1979), and out to 10kpc from the nucleus (Malin, Quinn and Graham 1983). Here we present large scale infrared mosaics in the J (1.24μm), H (1.65μm), and K (2.16μm) bands of the inner region containing the dust lane.

---

[5] We use a distance of 3 Mpc to Cen A (Tonry and Schechter 1990)

The optical morphology of the dust lane has been modeled as a transient by Tubbs (1980), and as an equilibrium structure in a rotating triaxial galaxy by van Albada, Kotanyi and Schwarzschild (1982). The observed stellar rotation does not support the latter interpretation (Wilkinson *et al.* 1986). QZPP found that the kinematics of the CO gas in the inner region ($r < 70''$) (where r is the distance from the nucleus of the galaxy) was not consistent with non-circular motion on a principal plane of a triaxial galaxy. However, Nicholson *et al.* (1992) and QZPP find that the kinematics of both the ionized and molecular gas is well modeled by a warped disk composed of connected rings undergoing circular motion. In Tubbs' (1980) model, the gas disk is assumed to be initially on a plane that is not a principal plane of the underlying galaxy. The gas disk then evolves into a warped shape as a result of differential precession. This type of model was successfully used to fit the CO data of Cen A in the inner region ($r < 70''$) (QZPP) and has reproduced the morphology of other galaxies, most notably the remarkably twisted disk of NGC 4753 (Steiman-Cameron, Kormendy and Durisen 1992).

Nicholson *et al.* 's (1992) model for the warped disk has an outer fold which is consistent with the optical appearance of the dust lane and an inner fold (at $\sim 30''$) which corresponds to a fold at the same radius in the model of QZPP, but differs from QZPP by having the northern side of this fold towards us instead of away from us. Because the disk is both geometrically thin and optically thin in both CO (QZPP) and Hα (Bland *et al.* 1987), the velocities fields from the CO and Hα are symmetrical about the origin and it is difficult to determine which side of the disk is towards us. However, in the near infrared, it is possible to see through the outer fold (prominent optically) into the inner region ($r < 70''$). Since the morphology in the near infrared is determined primarily by the absorptive properties of the disk, the morphology is not symmetrical about the nucleus. It is possible to compare to the models derived from kinematic data and resolve their differences. Our near infrared data extends previous images of the nucleus of Cen A in the near infrared (Giles 1986, Joy *et al.* 1991, Turner *et al.* 1992) and has a field of view large enough to cover both the optical dust lane and the region observed in CO and Hα.

Since the morphology of the infrared data is determined primarily by the warped disk, we devote the first half of our paper to verifying the geometry of the warp, and to determining the opacity of the warped disk. In order to do this, we integrate the light of the galaxy using a purely absorptive model for the warped dusty disk (described in §3), and compare the results of the integration with our data (§4). Our model for the geometry of the gas disk is based upon the model used to fit the CO data (QZPP). A modification of this model, in which the gas disk is at a higher inclination (with respect to the axis of symmetry of the potential) at large radii ($r > 80''$) than in the inner region fits the infrared morphology and colors remarkably well.

Much of the interpretation of observations in the nuclear region of Cen A relies on accurate knowledge of the location and opacity of the gas disk. In §4 we discuss the differences between the data and our model and predictions for X-ray absorption. We find that observation of a one-sided X-ray jet cannot be accounted for by absorption of X-rays on the other side of the nucleus by the gas disk. Since our models do not have an elongation of the J and H isophotes at the nucleus which is seen in our data, we support Joy *et al.* 's (1991) interpretation of this elongation as evidence for an infrared jet. We interpret extended features observed in the K isophotes $30 - 50''$ from the nucleus that are not predicted in our purely absorptive model for the disk, as emission in K from the disk. In §4.1 possible emission sources are discussed.

In §5, we propose a scenario for the merger, based on the infall by dynamical friction of a spiral galaxy into a large elliptical. We find an orbit for the infalling spiral that is consistent with our model for the data constructed in §3. A discussion follows in §6.

2. OBSERVATIONS

We obtained near-infrared images of Cen A with the IR imager at CTIO on May 7-9 1989. with the 1.5 meter telescope. Each pixel of the imager projects to $0.89''$ on the sky and the resultant field of view is $51.6'' \times 55.2''$. Images were obtained in the standard J(1.24μm), H(1.65μm) and K(2.16μm) photometric bands.

Most of the data presented here were obtained on May 7 and 9. The photometric stability was determined from photometry of the Elias *et al.* (1982) standards GL390, HD161743, and HD106965, which demonstrated that the photometric zero point was stable to better than 0.15 magnitudes. This level of photometric accuracy is sufficient for the current study of Cen A, which is primarily morphological. The seeing was typically $1.7''$ (full width half max after a 60 second integration in J and H). The observations were combined into mosaics, presented in Figures 1,2, and 3 after correction for the slight non-linearity of the array, sky subtraction, flat-fielding, and correction for residual sky background variations. In Figures 1-3 the maximum and minimum surface brightness levels where chosen in order to show the dust features at high contrast. See Figures 7a-9a (contour plots) for detail at the nucleus.

Data were obtained in pairs of object–sky fields. Each frame in H and J consists of three 60 second exposures and in K consists of six 30 second exposures. The position for the sky frames was $\simeq 30'$ either to the east or west from the nucleus of the galaxy so that the sky frames are uncontaminated by galaxian light. The first stage of reduction was to perform pair–wise subtraction of the adjacent sky frames. Gain variations across the detector array were then corrected by dividing by dome flats. As a consistency check we compared the dome flats with a flat made from a dark subtracted average sky, and found no significant difference.

The area observed was covered using a rectangular RA–DEC grid of three rows. Each row was observed with an offset in RA of $\simeq 25''$, or approximately half the field of view. The DEC offset between the rows was also $\simeq 25''$. Therefore the central $\simeq 50''$ is covered 4 times, and most of the edges twice. A total of 20 frames in each band were obtained. Telescope offsets were unreliable and therefore the relative positions of the fields comprising the mosaic were determined from the position of stars in the individual frames. The resultant registration is good to $1''$ over the entire mosaic. Registration offsets degraded the resolution of the mosaics to $2-3''$ (full width half max of a point source).

Despite our efforts to ensure accurate sky subtraction by obtaining sky measurement immediately after the object frames, residual sky variations are present in the reduced frames. Therefore, in constructing the final mosaic we adjusted the background level in each frame until the difference between overlap regions was zero. This process was successful, and frame boundaries are difficult to see in Figures 1,2 and 3. The sum of the frame offsets is constrained to be zero so that no spurious sky offset is introduced, and the sky level in the final mosaic is as close to zero as permitted by sky level variation during the observations. The resultant sky level uncertainty corresponds to 16.6 mag/square arcsecond at K, 16.5 mag/square arcsecond at H, and 18.1 mag/square arcsecond at J.

Some additional data were obtained on May 8. This night was mostly cloudy, except for a brief clear spell during which the three frames which complete the NW corner of each mosaic were obtained. These data are clearly inferior to the data obtained on the May 7 and 9 due to large transparency variations. They are included in the mosaic for completeness after making a crude compensation for transmission based on standard stars. Inspection of the mosaic shows that this is apparently successful because these frames blend seamlessly with the rest of the mosaic. However, we place low significance on the morphology and colors in this part of the mosaic, and no conclusions are based on that part of the image.

In order to improve our photometric accuracy, calibration was done by matching to the aperture photometry of Turner *et al.* (1992) at the position of the 2.2μm nucleus. Their photometric accuracy was uncertain by 0.18 magnitudes in J and H and by 0.13 magnitudes in K.

The morphology of our data is primarily determined by the presence of an absorptive thin dusty warped gas disk. Such a disk at high inclination with respect to the line of sight presents higher optical depth at folds where the disk becomes tangent to the line of sight. Since the gas disk of Cen A is at high inclination we expect the prominent features of the infrared mosaics to correspond to folds in the gas disk. In Figure 1, lines of sight of higher optical depth are apparent both above and below the nucleus. The fainter fold seen primarily on the northeast side corresponds to a fold described by Nicholson *et al.* (1992) which from their Hα velocity field, they found to be at a radius from the nucleus of approximately $100''$. This outer fold is prominent in optical pictures of Cen A, and forms the northern boundary of the dust lane. On the southern side of the nucleus, there is a more prominent fold (which we expect is closer to the nucleus) which has been seen in the near infrared previously by Giles *et al.* (1986) and Joy *et al.* (1991). Nicholson *et al.* (1992)'s model for the warped disk, depicted this inner fold so that the southern side was away from us instead of towards us as we observe it. Because of the symmetry of the Hα velocity field, it is not possible to determine from these data which side of the disk is closer to us. We suspect that the intensity of the Hα emission on the southern side is dimmer because there is more absorption from dust in the inner region ($r < 100''$) on the southern side of the disk. We note that the orientation of this inner fold is consistent with the model for the warp derived from the CO data, which was consistent with the shape of the southern side of the dust lane as seen in the optical. We expect this model to fit our infrared data well in the inner region where a good fit was found to the CO data ($r < 70''$). However, this model does not have an outer fold that corresponds to the northern fold observed in the infrared (at $r \approx 100''$) which forms the northern side of the dust lane. Therefore in order to fit the infrared data, the model must be modified for $r > 70''$ to include an outer fold.

Also observed in our data is an elongation to the NE (on a scale of $3'' - 10''$) of the isophotes at the position of the nucleus in J, and H, that is aligned with the direction of the soft X-ray jet (Feigelson *et al.* 1981). This elongation has been interpreted as evidence for a one-sided infrared jet by Joy *et al.* (1991). In §4.2, by comparing with the results of our models we attempt to determine whether this feature is an artifact of absorption through a warped dusty disk.

In K, extensions of the isophotes are observed to the SE and NW $30'' - 50''$ from the nucleus that are not observable in the J and H mosaics. It is possible that these features are due to some emission from the disk. In §4.1, possible emission sources are discussed.

The opacity of the dust is much less in K than at in J and H. Primarily what is observed (except for at the location of the nucleus and the features discussed previously) is the old stellar population of the background elliptical galaxy. In the next section we use the surface brightness in K to determine the light distribution which we use to integrate the light of the galaxy through an absorptive warped disk. The resulting models can then be compared to our mosaics.

3. INTEGRATION OF LIGHT

In this section we discuss how the light from the underlying galaxy is integrated to simulate the infrared observations. Our simple model integrates starlight along the line of sight in steps of 45 pc which corresponds to $3''$ square pixels on the sky, given a density as a function of radius for the light of the background galaxy. The density function used is discussed in §3.1. When integrating along the line of sight, every time the dusty disk is encountered, we multiply by a transmission coefficient. In §3.2 we discuss the absorptive properties of the dusty disk which determine the transmission coefficients in J,H and K. In §3.3 we describe our model for the geometry of the warped gas disk.

3.1 *Background Galaxy*

In the K band the opacity of the dust is much less than in J or H and therefore gives the best measurement of the the old stellar population of the background elliptical galaxy (except perhaps at the position of the nucleus ($r < 5''$) where the extinction is high, and there may be emission from an active nucleus). We use the surface brightness in K to determine the light distribution of the background galaxy. In Figure 4, surface brightness at K in magnitudes per square arcsecond is plotted against $r^{1/4}$ for an average of pixels in a narrow wedge of our data 10 degrees wide extending from the nucleus to the eastern edge of the mosaic. We chose this region of the data because it was least contaminated by the dustlane. Pixels in the dust lane at the same radius are at most 0.6 magnitudes per square arcsecond fainter than the points shown in Figure 4. The size of the error bars is determined by the uncertainty in the underlying sky level of the mosaic and the root mean square variation of the pixels used in the average. A variation in the base underlying sky level would cause a change in curvature primarily at large radii ($r > 40''$) on this plot.

We need a simple analytic form for the density of the galaxy light. Figure 4 shows that the data at K obey a de Vaucouleurs ($r^{1/4}$) law (previously noted by Giles 1986) but with a smaller effective radius than is observed optically in the outer regions ($r > 80''$) of the galaxy (Dufour *et al.* 1979). This suggests that we use a Hernquist model (Hernquist 1990), which has a density distribution $\rho(r)$ described by

$$\rho(r) = \frac{M}{2\pi} \frac{r_0}{r(r + r_0)^3}, \tag{3.1}$$

where r_0 is the effective scale length, and M is the mass of the galaxy. The scale length r_0 is related to the effective radius r_e of the deVaucouleurs law by $r_0 = 1.8 r_e$. However the Hernquist model is only a good approximation to a deVaucouleurs law over the range $0.1 < r/r_e < 16$ and we have data at $r/r_e < 0.1$. Therefore we model the background galaxy as the sum of two Hernquist models. We parametrize the sum of the two models with effective scale lengths r_0 and r_1

and the ratio μ of the two masses of the Hernquist models comprising the sum. We determined the larger scale length to be $r_0 = 168''$ from the effective radius observed optically in the outer part of the galaxy (Dufour *et al.* 1979). By varying r_1 and the ratio μ we found a good fit to the data assuming that the galaxy has constant mass to light ratio over the scale of our data, with $r_1 = 15''$ and $\mu = 0.05$. The resulting model is displayed as the solid line in Figure 4. The values we found for r_1 and μ are not significant because of the uncertainty in surface brightness of our data, but we give their values in order to describe the function we used for the density distribution.

The solid line in Figure 4 shows the integrated surface brightness of the density function chosen to model the background galaxy. This density function fits the data well. Since the surface brightness in the outer part of the mosaic is uncertain (due to a possible sky offset), the surface brightness of our model in the outer region is also uncertain. However, information inferred from morphological changes caused by absorption from the dusty warped disk, should be unaffected by the uncertainty in the absolute magnitude of the model in this region. By choosing this function for the light density of the galaxy, our model is consistent with both the effective radius observed from the deVaucouleurs law optically in the outer region of the galaxy and the deVaucouleurs law observed from infrared observations in the inner region. In addition, the rotation curve of Cen A as observed in HI is consistent with this model for the density (van Gorkom *et al.* 1990) assuming the approximately constant mass to light ratio observed by van Gorkom *et al.* (1990). We note that the rotation curve for this potential does not differ significantly over the range of radii of our data from the rotation curve we chose to describe the warp (see next section).

In order to integrate the light in J and H we assumed that the background galaxy had no color gradient and had colors $J - K = 1.2$ mag. and $H - K = 0.30$ mag. which match the colors observed at the top left-hand corner of the mosaics (see Figures 10a-12a) where there is little dust reddening. Within the photometric accuracy of our mosaics, these colors are the same as typical old stellar population colors (Frogel *et al.* 1978).

3.2 *Disk Absorption*

In Figure 5 we show a J-H, H-K color–color plot for all the pixels in the J,H and K mosaics. The offset from the color of a typical old stellar population is probably due to zero-point errors in our photometry. Since pixels mostly lie close to the reddening line (displayed as a solid line in Figure 5), we use a purely absorptive model for the gas disk. We assume that there is no extinction anywhere but in the gas disk, and that the disk is thin (see discussion in QZPP for estimates of the thickness of the molecular disk). Our model ignores scattering by the dust.

Every time a fold of the warp is encountered the integrated intensity is multiplied by a transmission coefficient T where $T = e^{-\tau}$ and τ is the opacity of the disk. The extinction $A(\lambda)$ at wavelength λ is given by $A(\lambda) \approx 1.08\tau(\lambda)$. We note that if the gas is patchy and can be described as having an area filling factor f_a, the transmission coefficient would be $T = 1 - f_a(1 - e^{-\tau})$. For small values of f_a and τ the transmission can be approximated as $T \approx e^{-f_a\tau}$ so that $A(\lambda) \approx f_a\tau(\lambda)$ and $A(\lambda_1)/A(\lambda_2) = \tau(\lambda_1)/\tau(\lambda_2)$ for different wavelengths λ_1 and λ_2, which is independent of the filling factor. Since the molecular material in the disk has low area filling factor ($f_a < 0.1$, QZPP), and pixels in our data have colors primarily close to the typical galactic reddening line (see Figure 5), we suspect that this is a reasonable approximation. We note that if individual dust clouds absorbing light are optically thick, this approximation would not be valid. The extinction, $A(J)$, was varied for best fit to the morphology of the J mosaic, and the typical galactic extinction ratios from Mathis (1990) $A(K)/A(J) = 0.38$ and $A(H)/A(J) = 0.62$ were used to determine the absorption coefficients for H and K.

Since the disk is optically thin (in CO and Hα) except possibly at the folds (Bland *et al.* 1987 and QZPP), it is necessary to consider the opacity of the disk (or transmission coefficient in our integration) as a function of the local slope of the disk with respect to the line of sight. We can measure the local slope of the disk by computing a Jacobian, given by $J = \partial(x,y)_{disk}/\partial(x,y)_{sky}$ where $(x,y)_{disk}$ is a local coordinate system on the gas disk, and $(x,y)_{sky}$ is a Cartesian coordinate system on the sky. The Jacobian is the ratio of the projected area of a small piece on the disk to its real area. For $J < 2$, when the disk is close to face–on, in our integration we use a transmission coefficient $T = e^{-\tau}$ where $\tau = J\tau_p$, and τ_p is the opacity of the disk if it were viewed face–on. For $J > 2$, when the disk is at high inclination with respect to the line of sight, we use the transmission coefficient τ_p for a grid resolution element (used in integration). We assume that the thickness of the disk is smaller than our grid size. This represents the opacity per unit length of a thick slab viewed edge–on.

We chose a simple function for the dust distribution as a function of radius r from the nucleus that decays exponentially at large radii, yet is not sharply peaked in the center. In our models the face–on absorption of the disk at J as a function of radius is given by

$$\tau_p(r) = \frac{B_J}{\exp((r-b)/\sigma_\tau)+1} \tag{3.2}$$

with constants B_J, b and σ_τ. B_J is the optical depth of the disk at J at the nucleus if the disk were observed face–on, b is the radius at which the opacity of the disk begins to decay, and σ_τ is its exponential decay rate.

3.3 *Tilted Ring Model, Precession from a Plane*

Our model for the geometry of the warped disk is based upon a model (QZPP) for the gas that gives the best fit to to the ^{12}CO(2–1) data. This model, which fits the CO data well for $r < 70''$, is derived assuming that the gas has evolved from a planar system as a result of differential precession in a prolate potential

(Tubbs 1980). It assumes that the inclination of the gas rings with respect to the principal axes of the potential is a constant as a function of radius and time.

We describe the orientation of the potential with the two angles ϑ and χ, where χ is the position angle on the sky of the projected axis of symmetry (z-axis) of the prolate potential, measured from North and ϑ is the angle between the line of sight and the z-axis (i.e., the inclination of the galaxy). We describe the geometry of the warp with two additional angles which are functions of r, the distance from the nucleus. We can think of a warp as a set of smoothly connected inclined rings each centered on the nucleus of the galaxy (e.g., Sparke 1986). We denote z' as the rotational axis of symmetry of a ring at radius r, and let $\omega(r)$ be the angle between the z and z'-axes. We define $\alpha(r)$ to be the angle in the equatorial plane of the galaxy of the projection of z' onto this plane minus the angle of the projection of the line of sight (see Figure 6 for a pictorial representation of these angles). In an axisymmetric potential of ellipticity ϵ_p, the precession rate $d\alpha/dt$ is approximately

$$\frac{d\alpha}{dt} \sim \frac{\epsilon_p v_c}{r} \tag{3.3}$$

where v_c is the circular velocity at radius r. The ellipticity ϵ_p, is given by $\epsilon_p = 1 - 1/q$ where q is the axis ratio of the potential which for the nearly spherical systems that we are interested in, can be written approximately as a function of $x^2 + y^2 + z^2/q^2$. Prolate systems have $q > 1$ while oblate systems have $q < 1$. After a time Δt,

$$\alpha(r) = \epsilon_p \Omega \Delta t + \alpha_0 \tag{3.4}$$

where $\Omega = v_c/r$. We used the following rotation curve for the circular velocity v_c

$$v_c = \frac{Ar}{\sqrt{r^2 + c^2}} \tag{3.5}$$

with constants A and c. For large radii ($r \gg a$), this rotation curve approaches a flat rotation curve, the rotation curve of an isothermal sphere with velocity dispersion $\sigma = v_c/\sqrt{2}$. We note that the velocity curve of a galaxy with constant mass to light ratio and a surface density that follows a deVaucouleurs $r^{1/4}$ law (as Cen A is observed to be (van Gorkom *et al.* 1990 and Dufour *et al.* 1979)) is a reasonable approximation to the above rotation curve for non–large radii ($r \not\gg c$). We found a good fit to the CO data using a potential with a varying ellipticity $\epsilon_p = \epsilon_\infty(1 - \exp(-r^3/\sigma_{el}^3))$ where ϵ_∞ is the ellipticity far away from the nucleus, and σ_{el} gives the radius at which the ellipticity begins to decay. We note that it is evident from the K mosaic, that Cen A becomes more spherical in the central regions, though because of the dust, it is difficult to accurately measure the ellipticity as a function of radius. See Table 1 for the parameters of the best fit to the CO data (QZPP).

4. RESULTS OF MODELING

We found that the model from QZPP displays the morphology of the infrared data quite well in the central region ($r < 70''$) of the galaxy. The best fit to the CO data found that the inclination of the principal axes of the potential with respect to the line of sight was $\vartheta = 65°$ and that the gas has an inclination of $\omega = 25 \pm 5°$ with respect to the principal axes of the potential. However the geometry of the dust is different than that predicted by this model for $r > 70''$. In particular the fold of gas observed on the northern side of the nucleus (see Figure 1) that is also prominent optically and forms the northern side of the dust lane, is not seen in our model (see discussion in QZPP). From their Hα velocity field, Nicholson *et al.* (1992) found that the gas in this fold was at an inclination with respect to the line of sight of $i \approx 105°$. The gas in this outer fold is at inclination of at least $\omega = i - \vartheta \approx 40°$ degrees with respect to the principal axes of the potential. This inclination is significantly higher than that predicted by QZPP model for $r < 70''$. Because of this discrepancy, we find that the configuration of the gas in Cen A *is inconsistent with one of the assumptions of our previous model. Either the gas was not initially in a plane ($\omega(r)$ varies as a function of r) or $\omega(r)$ evolved with time.*

One mechanism that would account for large changes in the inclination of the gas rings with radius would be settling caused by viscosity between differentially rotating gas rings. However the timescale $\Delta T \sim 10^8$ yr to create the warp by differential precession that we derived from fitting to the CO data with our previous model was less than the settling timescale derived by Steiman–Cameron and Durisen (1988) (see QZPP for further details).

Another possibility is that the inclination of the gas resulted in some non-trivial way from the dynamics of the merger. If this were true, we would expect $\omega(r)$ to vary as a function of r. We found that we could reproduce the features of our infrared data by using a model with precession angle $\alpha(r)$ described by equation (3.4) but with inclination angle ω that increases from 20° to 40° at $r \approx 150''$. This new model is still consistent with the model derived from the CO data in the inner region ($r < 70''$), and has the outer fold at $\sim 100''$ that is observable in our infrared data. In §5 we discuss a scenario for the merging of a small spiral galaxy with a larger elliptical. We propose that changes in the inclination of the gas disk can result from variations in the orbital angular momentum of the infalling spiral galaxy.

The results of integrating the light of the galaxy at a resolution of $3''$ per pixel in the near infrared for our new model are displayed in Figures 7-9 along with data at the same contour levels on the same scale. We chose this value for the resolution of the models in order to match the resolution of the mosaics. Color maps are shown in Figures 10-12. Parameters for constructing these models can be found in Table 1. The parameters for the geometry of the warp are mostly identical to those that gave the best fit to the CO data (from QZPP) (also shown in Table 1) except that the inclination angle, $\omega(r)$ is no longer a constant as a function of radius. The function for $\omega(r)$ is displayed as the dotted line in Figure 14a. There are slight differences in the orientation angles of the underlying galaxy, χ and ϑ, between our infrared model and the older CO model. Parameters for the light distribution of underlying galaxy (discussed in §3.1) and absorptive properties of the disk (discussed in §3.2) are also found in Table 1. Qualitatively our models agree very nicely with the data (see Figures 7-12). The fold on the northern side of the dust lane that is at high inclination in our model is very similar to that observed in the data. Using the galactic extinction ratio to model the absorption of the disk in the different wavelengths seems to have reproduced the colors of the disk remarkably well.

The morphology of these models is primarily determined by the opacity of the disk at the folds. A good fit to the morphology of the data was found for $B_J = 0.15$. In our models we assumed that the the thickness of the disk is less than a model resolution element ($h < 3''$), which is not an unreasonably small value (see QZPP for limits on the thickness of the molecular disk.) Since the outer fold is more pronounced in the models than the data, it is likely that the disk is somewhat thicker than $3''$ in the outer region ($r > 75''$). We note that the outer fold is visibly clumpy (see Figures 1-3). Since our model assumed a smooth distribution for the gas, this may partly explain why this fold is more pronounced in the models. If the disk at large radii is not completely relaxed after the merger at larger radii (which could happen if the individual clouds composing the disk had low volume filling factor) we would expect the disk to be thicker in the outer regions. This would make the outer fold appear to be less sharp. The morphology of the inner fold seems to be well reproduced by the model, so that we doubt that the disk is thicker than $3''$ in the inner region ($r < 70''$). Because of the poor resolution of our mosaics, we cannot determine if the disk is thinner than $3''$ in the inner region. We note that models with $h = 2''$ at a resolution of $2''$ have quite a bit more structure than is predicted in the $3''$ resolution models.

4.1 *Disk Emission*

Our model does not show extensions in the higher magnitude K isophotes that are observed in the data along the disk $30'' - 50''$ to the southeast and northwest of the nucleus. It is possible that these extensions, seen only in K, are due to emission from the warped disk. Due to the large scatter of the pixels in our color-color plot (Figure 5), we cannot determine if the pixels in this region of the disk have different colors than expected from a purely absorptive model for the disk. However, since the purely absorptive model for the disk reproduces the colors and morphology of the rest of the data remarkably well, it is likely that these extensions in K are due to some emission from the disk. We estimate that ~ 17 magnitudes per square arcsec emission in K from the disk is necessary in order to account for the observed elongation of the isophotes in these features. We consider three possible emission sources: free-free and bound-free emission from HII regions in the disk, emission from bright giants and supergiants from the young stellar population in the disk, and emission from small hot grains of dust.

From an estimate of the maximum observed surface brightness in Hα of an HII region, we may estimate an upper limit for the maximum possible brightness expected from free-free and bound-free emission in the K band. Joss Bland-Hawthorn (private communication) estimates that the surface brightness in Hα is at most 4×10^{-14} ergs cm^{-2} s^{-1} arcsec^{-2} per individual HII region. Phillips (1981) has observed that the HII regions in Cen A are primarily low ionization regions with excitation temperature $T_e \sim 6500K$, and emissivity ratio $\gamma_{\mathrm{H}\alpha}/\gamma_{\mathrm{H}\beta} \sim 3$. Using an estimate of $\gamma_K/\gamma_{\mathrm{H}\beta} \sim 2 \times 10^{14}$Hz for these low excitation temperatures, (Joy and Lester 1988), and multiplying these factors together, we find that the surface brightness in K must be less than 7μJy arcsec^{-2} or greater than 20 magnitudes per square arcsec. Since the highest contour in our mosaic is at 16 magnitudes per square arcsec, even if the Hα flux were reddened by a few magnitudes, it is unlikely that we would detect emission from HII regions. We note that a Brγ observation in the disk would make this limit more convincing.

From a measurement of the star formation rate in the disk, we may estimate the maximum expected luminosity from the stellar component of the disk (as in Telesco and Gatley 1984). Marston *et al.* (1988) from the far-infrared emission from the disk estimate that the star formation rate is $\dot{M} = 1.6 \times 10^{-5} M_\odot$ yr^{-1}

arcsec^{-2} in the central region of the disk. Using this, the Salpeter initial mass function, and an estimate of the post-main-sequence lifetime as a function of stellar mass, $t_{pms} = 1.7 \times 10^9 (m/M_\odot)^{-2.7}$ yr (Renzini 1981), we find that the number of post-main-sequence stars with mass greater than $4M_\odot$ (the main sequence cutoff mass after 10^8 yr) expected is approximately 10 per square arcsec. If these stars are giants with absolute magnitude in K of -6, with a distance modulus of 27 to Cen A, we find that the maximum surface brightness from these stars in K would be $\sim$ 18 magnitudes per square arcsec which would be undetectable in our K mosaic. Similarly we estimate the number of post-main-sequence stars with mass larger than $10M_\odot$ to be 0.1 per square arcsecond. If these were all red supergiants of luminosity $10^6 L_\odot$ and effective temperatures of $\sim 3000K$ then the maximum surface brightness from these stars in K would be $\sim$ 18 magnitudes per square arcsec which would also be undetectable in our mosaic. We note that luminosity from the main sequence is also negligible assuming that there was 10^8 years of star formation at the star formation rate given above. If the star formation rate were higher in the recent past than is now observed, it is possible that giants and supergiants could account for the excess emission. Older stars should not be present in the disk since the time since the merger is of order 10^8 years, and stars captured from a merging galaxy cannot settle onto a disk. We find that it is unlikely that any observed emission from the disk in K is due to emission from giants and supergiants in the disk.

Sellgren *et al.* (1984) in their observations of reflection nebulae note that under special physical conditions, the amount of UV radiation is sufficient to produce observable near-infrared emission from thermally fluctuating small dust grains, yet insufficient to create an HII region. It is possible that Cen A could satisfy these conditions since the observed HII regions are mostly low ionization regions, yet it is evident from the far-infrared flux (Marston *et al.* 1988) that there is a significant amount of UV emission from newly forming stars in the disk. Existing aperture photometry in the L (3.5μm) band allows us to estimate how much emission is due to small hot dust grains. Using photometry from Becklin *et* *al.* (1971) we find that the difference between the 33″ aperture magnitude and the 67″ magnitude gives a flux of $\sim 500\mu$Jy per arcsecond in the annulus. If the flux level were a factor of 5 lower in K than at L (as is observed in reflection nebulae Sellgren *et al.* 1984) we would measure a surface brightness of 17 magnitudes per square arcsecond, which would be detectable in our mosaic. It is possible that we could be observing emission from small dust grains in K; however more data is needed to verify this. Usually excess brightness at K in star forming galaxies is due to red giants and supergiants. It is therefore unexpected that dust emission is a more likely source for this emission in the disk of Cen A. It is surprising that the peculiar conditions in reflection nebulae could possibly be found on a galactic scale in the disk of Cen A.

4.2 *The Nucleus of Cen A*

The location of the peak surface brightness at the nucleus in Cen A is a function of wavelength in the near infrared (Giles 1986). See Table 2 for nuclear offsets from Star A which has position RA 13h 22m 27.72s ±0.03 and Dec $-42^\circ 45' 19''.39 \pm 0.35$ (1950) (Griffin 1963). Within the listed errors, the nuclear position in K agrees with that reported by Giles (1986). However, our model does not predict any difference of position between the J, H and K peaks (even when integrated at higher resolution). We note that the displacement of the color peaks from the position of the K nucleus (see Figures 10-12) is reproduced by our model. In our model the gas disk in the inner region only partially shields the nucleus (although it covers the nucleus at larger radii $r > 90''$). In order to account for changes in the position of the nucleus, there must be either a thick circumnuclear disk or extra folds of the warp near the nucleus. It is possible that the changing position of the nucleus is due to the circumnuclear disk (Israel *et al.* 1990) observed in absorption against the continuum source. The function we used for the dust surface density as a function of radius (equation 3.2) is almost flat for $r < 60''$. However, the 2.5 magnitudes high color peak at the nucleus observed in J-K color is apparent in our model (see Figure 12), and is $\sim 4''$ south of the K nucleus (as it is observed). Therefore the observed maximum in J-K color is caused by absorption through a disk of almost constant dust surface density that is close to edge–on, not by an increase in the quantity of dust near the nucleus. The dust surface density must increase sharply at small radii ($r < 5''$) where the circumnuclear disk is located, in order to account for the peak offsets yet not effect the colors and morphology observed outside this radius.

As have Joy *et al.* 1991, we observe elongation (on a scale of $3 - 10''$) of the nucleus along the direction of the X-ray jet in the J and H mosaics. This elongation was interpreted by Joy *et al.* 1991 as evidence for an infrared jet. Since our model does not predict any such elongation, it is probable that excess emission along the direction of the jet is necessary in order to account for this elongation.

4.3 *X-ray Absorption*

In this subsection we use our best fit model for the geometry and distribution of the dust and gas to create a transmission map for X-rays which we can then compare to existing X-ray maps of Cen A. By integrating from the plane perpendicular to the line of sight containing the nucleus of Cen A out towards us we estimate an opacity $A(J)$ for every location on the sky. We expect most of the X-ray emission to be coming either from the nucleus, or from a cylinder along the direction of the jet that is lying in a plane that is close to perpendicular to the line of sight. Using $A(J)/N_H = 1.5 \times 10^{-22}\mathrm{mag\ cm^2 H\ atom^{-1}}$ (Mathis 1990), we may estimate the column density N_H of hydrogen atoms. A rough fit to the column density at which $\tau = 1$ (Gursky 1973) (assuming solar abundances) is

$$\log_{10}(N_H) = 2.7 \log_{10}(E/\mathrm{eV}) + 13.7, \tag{4.1}$$

where E is the energy in eV and N_H is the column density of hydrogen atoms in units of H atoms/cm^2. Thus we may estimate at each position on the sky the energy at which the gas would become optically thick to X-rays. The result of this integration of our model is displayed as a contour plot in Figure 13.

As is predicted by our model, diffuse soft X-ray emission (< 2 keV) from EXOSAT is observed to the north and south on either side of the disk (Morini *et al.* 1989). At higher resolution with Einstein's HRI (Feigelson *et al.* 1981) in the $0.5 - 4.5$ keV band, a jet is observed that is one sided (Feigelson *et al.* 1981). The jet is observed above and below the ridge of opacity caused by the fold in the disk that runs east–west and is located $\sim 30''$ north of the nucleus. This emission along the jet must be primarily soft X-rays because it is absorbed by this fold in the disk which is not opaque to hard X-rays. Because of the high inclination of the gas disk, it is not possible to block soft X-rays over a large area on the sky. The fact that a soft X-ray jet is only observed on one side of the nucleus is not explained by our model.

At the position of maximum infrared opacity we estimate $N_H = 2 \times 10^{22}\mathrm{cm}^{-2}$ which is lower than the measurement at the position of the nucleus of Morini *et al.* (1989) of $N_H = 1.5 \times 10^{23}\mathrm{cm}^{-2}$. We note that the position of maximum infrared opacity is $\approx 4''$ to the south of the position of the K nucleus in our model. We inferred in the previous subsection that there is probably a circumnuclear disk that is not included in our model which should contribute to the opacity in front of the nucleus. This may partially explain why our estimate is so low. We note that some of the X-ray opacity near the nucleus comes from a fold in the disk that is lying almost on top of the nucleus. If Cen A were at a different orientation with respect to us, it is likely that the opacity near the nucleus would be reduced.

5. DYNAMICS OF THE MERGER

In §3.3 we reviewed the model that we successfully used to fit CO data in the inner regions of Cen A (QZPP). This model assumed that the gas has evolved from a planar system as a result of differential precession (Tubbs 1980). The model that reproduced the infrared morphology had a precession angle $\alpha(r)$ described by equation (3.4), yet large changes in inclination angle, $\omega(r)$, were necessary in order to reproduce the outer fold at $r \approx 100''$ from the nucleus. *This model is therefore inconsistent with evolution by differential precession from an initially planar system.* Since the timescale for creating the warp in Cen A is short ($\sim 10^8$ yr), it is unlikely that settling onto the principal plane of the galaxy could have caused these large changes in inclination (QZPP). In this section we will discuss the possibility that the changes in inclination of the gas resulted from the dynamics of the merger.

Malin *et al.* (1983) have observed there is a single stellar shell at $\sim 3'$ from the nucleus of Cen A, and about 20 shells in a range of $7 - 15'$ from the nucleus. They found that it is difficult to produce such a gap between stellar shells with a single accretion event. However Dupraz and Combes (1987) find that multiple events of stripping as the galaxy spirals in under the force of dynamical friction can account for the location of shells in the inner regions of galaxies. Simulations of galaxy mergers show that multiple systems of shells over a large range of radii may be produced (Salmon *et al.* 1989). Huang and Stewart (1987) found in their simulations that material stripped continuously will also form a sequence of stellar shells.

Because gas clouds dissipate energy during collisions, gas evolves into a configuration in which the collision rate is a minimum, such as a ring. Gas stripped tidally from a small gas rich spiral, while spiraling into a larger elliptical galaxy, is sheared by the differential rotation rate into rings which then precess according to equation (3.3). It is likely that the radius and orientation of these rings are determined by the angular momentum of the gas at the time of stripping. Because the underlying elliptical galaxy is not spherical, the orbit of the infalling galaxy is not constrained to lie in a plane, and so the resulting gas configuration may have large changes in inclination as a function of radius. Using these simple assumptions, we can determine the geometry of the gas from an integration of the orbit of the infalling galaxy. The resulting warped gas geometry can then be compared to the geometry needed to model our infrared mosaics. We expect the actual gas dynamics during the merger to be far more complicated than what is presented here, so we intend this scenario to only be a test of our simplifying assumptions.

In §5.1 we discuss a scenario for creating the warped configuration of gas and dust based upon the reconstruction of the merger of a small spiral with a large elliptical galaxy. Gas stripped tidally from an infalling galaxy is expected to shear out into a disk or ring in a few rotation periods (Tubbs 1980). This has since been observed in smooth particle hydrodynamic simulations (Habe and Ikeuchi 1988). The orientation and radius of the gas rings are determined by the angular momentum of the gas when it is stripped from the infalling spiral galaxy. In §5.1 we discuss the process of infall due to dynamical friction assuming that both the spiral galaxy and the elliptical can be approximated by isothermal spheres. For the merger that resulted in Cen A, we find that the spin angular momentum of the spiral galaxy can be neglected, and that the shearing timescale for the gas to spread out into a plane after stripping is of the same order of magnitude as that proposed by Tubbs (1980). We find that when the orbit of the infalling galaxy remains on a plane and the underlying galaxy has constant ellipticity, the resulting configuration of the gas is identical to that described by the model discussed in §(3.1) where the gas was initially in a plane.

In §5.2 we discuss a numerical integration of the orbit of the infalling galaxy, and the initial conditions used for our integration. The effects on the integration of the prolate shape of the underlying galaxy and possible high ellipticity of the orbit are explored. We find an orbit that not only reproduces the changes in inclination observed in our infrared mosaics, but also reproduces the gap in the stellar shells observed by Malin *et al.* (1983).

5.1 *The Scenario*

In order to model the dynamics of the infalling galaxy, we need to estimate the mass of the spiral remaining after tidal stripping during the encounter. This treatment is similar to that presented by Dupraz and Combes (1987). The mass of the spiral left after stripping is determined roughly by the radius r_s from the nucleus of the spiral at which the tidal force of the elliptical on the spiral is equal to its binding force

$$\frac{M_e(D)r_s}{D^3} = \frac{M_s(r_s)}{r_s^2}, \tag{5.1}$$

where $M_e(D)$ is the mass of the elliptical galaxy inside radius D, the distance of the spiral from the nucleus of the elliptical, and $M_s(r_s)$ is the mass of the spiral inside radius r_s (which can be thought of as a stripping radius). Since spiral galaxies commonly have a flat rotation over a wide range of radii, we may approximate the spiral galaxy as an isothermal sphere. The rotation curve (assuming constant mass to light ratio) that corresponds to the observed de Vaucoulers luminosity profile of NGC5128 (Dufour *et al.* 1979) is close to flat from $r \approx 70''$ to $r \approx 15'$ (the location of outermost stellar shell (Malin *et al.* 1983) from which we estimate the impact parameter of the collision that resulted in the merger). Over this range of radii, the elliptical galaxy may also be approximated as an isothermal sphere. The mass inside radius r for an isothermal sphere with velocity dispersion σ, is

$$M(r) = \frac{2\sigma^2 r}{G}. \tag{5.2}$$

Approximating both galaxies as isothermal spheres we estimate r_s to be

$$r_s = \frac{\sigma_s}{\sigma_e} D \tag{5.3}$$

where σ_e and σ_s are the velocity dispersions of the elliptical and and spiral respectively. Using the two previous equations we find that $M_s(D)$, the mass of the spiral galaxy, when it is at distance D is

$$M_s(D) = \frac{2\sigma_s^2 r_s}{G} = \frac{2\sigma_s^2 D}{G}(\frac{\sigma_s}{\sigma_e}). \tag{5.4}$$

The mass stripped from the spiral dM as it falls a distance dD is

$$\frac{dM}{dD} = \frac{2\sigma_s^2}{G}(\frac{\sigma_s}{\sigma_e}). \tag{5.5}$$

From this we can see that dM/dD is roughly constant, and that material from the spiral galaxy will be at a radius in the elliptical galaxy that is a factor of σ_e/σ_s larger than the distance that it was from the center of the spiral galaxy before stripping. Because of this we expect there to be gas quite far out in the elliptical galaxy, as is observed by Malin, Quinn and Graham 1983 (out to 11 kpc), and in other galaxies that are the results of mergers (e.g., NGC4753 Steiman-Cameron, Kormendy and Durisen 1992).

The geometry of the gas will be primarily determined by the angular momentum of the gas during stripping. The resulting angular momentum per unit mass of the gas after stripping is $L_{orb} + L_{spin}$ where L_{orb} is the orbit angular momentum per unit mass of the infalling galaxy and L_{spin} is the spin angular momentum per unit mass of the gas at the stripping radius of the infalling spiral galaxy. The amount of molecular material in Cen A, 2×10^8 M$\odot$ (Phillips *et al.* 1987), is roughly 1/5 of that found in our Galaxy. Assuming that both our Galaxy and the small spiral believed to have fallen into the center of Cen A, are isothermal spheres, that galactic mass scales with gas mass, and that the circular velocity of our galaxy in the outer regions is approximately 220 km s^{-1} , we estimate the velocity dispersion of the small spiral σ_s to be roughly 70 km s^{-1}. We have assumed that the amount of the molecular gas that has been disassociated during the merger is not significant. The velocity dispersion of Cen A has been measured to be 150 km s^{-1} (Wilkinson *et al.* 1986), whereas the circular rotation speed has been measured to be approximately 300 km s^{-1} (QZPP). Wilkinson *et al.* (1986) demonstrate by simulating the effect of the dust lane on their observations, that the dust lane can cause the velocity dispersion to be underestimated, so it is likely that their measurement σ_e is lower than the real value. Taking $\sigma_e = v_c/\sqrt{2}$, we infer that $\sigma_e/\sigma_s \approx 3$. We note that using the Tully-Fisher relation to estimate the mass of the small spiral galaxy would have lowered this ratio. The orbital angular momentum per unit mass of the infalling galaxy is approximately $L_{orb} \approx Dv_c$. The spin angular momentum per unit mass of gas stripped from the infalling galaxy at the stripping radius r_s is approximately $L_{spin} \approx (\sigma_s/\sigma_e)v_c r_s$. Using equation (5.3) we find that

$$L_{spin}/L_{orb} \approx (\frac{\sigma_s}{\sigma_e})^2 \approx \frac{1}{9}, \tag{5.6}$$

so that for Cen A, the angular momentum and resulting geometry of the gas is primarily determined by the orbit of the infalling galaxy. As a result we neglect the spin angular momentum in our models.

It has been proposed by Tubbs (1980) (and later observed in smooth particle hydrodynamic simulations Habe and Ikeuchi 1988) that smearing of captured gas into a disk or ring should occur over a few orbital periods. After stripping we expect the gas to be in a stream of width of order r_s. The shearing timescale t_{shear} or the timescale for a blob of gas of width r_s at distance D from the nucleus to be sheared by differential rotation is of order

$$t_{shear} \sim t_D \frac{D}{r_s} \sim t_D \frac{\sigma_e}{\sigma_s} \tag{5.7}$$

which is consistent with the timescale proposed by Tubbs (1980).

A generalization of the model discussed in §3.3 can be made by assuming that the length of time a ring at radius r has precessed depends upon the time since the gas in the ring was stripped from the infalling galaxy, and that the radius and initial angles of the ring depend upon the angular momentum of the gas at stripping. This is equivalent to assuming that Δt, and α_0 of equation (3.4) are functions of r. In this case equation (3.4) becomes

$$\alpha(r) = \alpha_0(r) + \epsilon_p \Omega \Delta t(r) \tag{5.8}$$

for $\Delta t(r) = \Delta t_0 + t_{sink}(r)$ where Δt_0 is the time since the infalling galaxy reached the nucleus, $t_{sink}(r)$ is the time the spiral took to spiral into radius r, and $\alpha_0(r)$ is determined from the angular momentum vector of the gas when it was stripped.

In order to estimate $t_{sink}(r)$ we must integrate the equations of motion of the spiral galaxy as it is spiralling into the elliptical under the force of dynamical friction. Since the frictional force is tangential, the spiral galaxy looses angular momentum. If the orbit is close to circular we may estimate that

$$D\frac{dD}{dt} = -0.428\frac{GM_s(D)}{v_c}\ln\Lambda \tag{5.9}$$

(Binney and Tremaine 1987), where for elliptical galaxies, the Coulomb logarithm $\ln\Lambda$, is typically of order 21. Using our previous estimate for $M_s(D)$ we obtain

$$\frac{dD}{dt} = -0.428\ln\Lambda(\frac{\sigma_s}{\sigma_e})^3 v_c \tag{5.10}$$

for the infall rate which is approximately constant. The resulting orbit for the infalling spiral galaxy is a logarithmic spiral. $t_{sink}(D)$, the time for the spiral to fall into the nucleus from radius D is

$$t_{sink}(D) = \frac{D}{dD/dt} = t_D(\frac{\sigma_e}{\sigma_s})^3\frac{1}{0.428\ln\Lambda} \tag{5.11}$$

where $t_D = 1/\Omega$ is the dynamical timescale at radius D. Numerical simulations of dynamical infall timescales in a self–consistent potential agree with this expression to within an order of magnitude (Sterl Phinney private communication).

Using the previous expression for t_{sink} and equation (5.8) we find that

$$\alpha(r) = \alpha_0(r) + \epsilon_p\Omega\Delta t_0 + \frac{1}{0.428\ln\Lambda}(\frac{\sigma_e}{\sigma_s})^3\epsilon_p. \tag{5.12}$$

If the background galaxy has constant ellipticity ϵ_p, and if $w(r)$ and $\alpha_0(r)$ are constant, then the third term in the previous equation is a constant, and the resulting models are identical to those discussed in §3.3 where we assumed that the gas was initially on a plane. This would be the result of a planar orbit where the orientation of angular momentum vector of the infalling galaxy is roughly conserved. At time Δt_0, when the infalling galaxy reaches the nucleus, the gas stripped from the galaxy would be lying in a plane. This may partially explain why Tubbs's (1980) model in which the initial configuration for the gas is in a plane has been so successful. Over a limited range of radii where the orbit of the infalling galaxy remains on a plane, we expect Tubbs's model to give a good approximation for $\alpha(r)$. This may explain why we previously found such a good fit to our CO data (see QZPP) using this model and why it has been so successful in modeling the morphology of other galaxies (e.g., the remarkably twisted disk of (Steiman-Cameron *et al.* 1992)). We note that small variations in ϵ_p with radius can produce large variations in $\alpha(r)$. In the central regions ($r < 70''$ where the rotation curve drops), the potential of the elliptical galaxy cannot be approximated as an isothermal sphere, and the previous equation is no longer valid.

5.2 *Numerical Integration of Infalling Orbit*

In a non-spherical galaxy it is necessary to numerically integrate the equation of motion in order to determine the orbit of an infalling galaxy. In this section we give the equation of motion, and describe our choice of initial conditions for the integration.

Using a fourth order Runge-Kutta numerical integrator integrator with adaptive step size, we integrated the equation of motion of the infalling galaxy that spirals into the elliptical galaxy under the force of dynamical friction. The potential used for the elliptical galaxy is that of a logarithmic prolate, $\varphi(\vec{x}) = v_c^2 \ln s$, where $\vec{x} = (x, y, z)$ and $s = \sqrt{x^2 + y^2 + z^2/q^2}$. For a prolate potential $q > 1$ and $\epsilon_p = 1 - 1/q > 0$. The equation of motion for the spiral galaxy is

$$\frac{d\vec{v}}{dt} = -\vec{\nabla}\varphi(\vec{x}) - \eta 4\pi (\ln\Lambda) G^2 \rho(\vec{x}) M_s(\vec{x}) \left(\mathrm{erf}(X) - \frac{2X}{\sqrt{\pi}} e^{-X^2} \right) \frac{\vec{v}}{|v|^3} \qquad (5.13)$$

where $\vec{v}$ is the velocity of the spiral, $\vec{x}$ is its position in the elliptical, $X = |\vec{v}|/v_c$, $\rho(\vec{x}) = \nabla^2\varphi(\vec{x})/4\pi G$ is the density of the background elliptical galaxy at $\vec{x}$, and $M_s(\vec{x})$, the mass of the spiral when it is at $\vec{x}$, approximated by

$$M_s(\vec{x}) = (\frac{\sigma_s}{\sigma_e}) \frac{2\sigma_s^2 s}{G}. \qquad (5.14)$$

The dynamical friction term in equation (5.13) is derived from the Chandrasekhar dynamical friction formula assuming that the velocity distribution of the background galaxy is both isotropic and Gaussian (Binney and Tremaine, 1987 equation 7-18). η represents a correction factor to the size of the dynamical friction term in order to compensate for the fact that the velocity dispersion of a self-consistent model for the galaxy would be smaller than that of an isothermal sphere. We chose $\eta = 2.0$ since the velocity dispersion of the Hernquist model (Hernquist 1990) for the range of radii of our integration gives this factor difference in the equation of motion (equation 5.13). Integration of these equations of motion using a anisotropic velocity dispersion did not significantly change the shape of the resulting orbit (for $\sigma_x/\sigma_z \sim 1/q \sim 0.8$). This is not surprising because the difference in the dynamical friction force is of quadrupole order in the integral over the stellar velocity distribution (see equation 7-14 Binney and Tremaine). If the orbit is highly elliptical, stripping will not proceed at a constant rate. When s increased, we did not allow the mass of the infalling galaxy to increase.

From the integration of the orbit of the infalling galaxy we determine the configuration of the gas stripped along the orbit. The angular momentum per unit mass of material stripped at any point on the orbit of the infalling galaxy is $\vec{L} = \vec{x} \times \vec{v}$. Material stripped will form a ring at radius r which we estimate to be at $r = |\vec{L}|/v_c$. The inclination $\omega(r)$ of the resulting gas ring is given by

$$\cos(\omega(r)) = L_z/|\vec{L}| \tag{5.15}$$

and the angle $\alpha_0(r)$ at the time of stripping is given by

$$\cos(\alpha_0(r)) = \frac{L_x}{|\vec{L}|\sin\omega(r)}. \tag{5.16}$$

Since angular momentum of an orbit is not conserved in a non-spherical potential, the resulting inclination of gas stripped from the infalling galaxy $\omega(r)$ will not in general be constant. After stripping, the gas ring is free to precess as in our previous model with precession rate given by equation (3.3), so that the angle $\alpha(r)$ for the system at a later time is

$$\alpha(r) = \alpha_0(r) + \epsilon_p \Omega(t_{sink}(r) + \Delta t_0) \tag{5.17}$$

(see analogous equation (3.4)). We note that the integration for $r < 100''$ (near where the rotation curve begins to drop) is not accurate because Chandrasekhar's dynamical friction formula is no longer valid when the mass of the infalling object at radius r is small when compared to the mass of the surrounding galaxy inside r. Therefore we used $t_{sink}(r)$ to be the time since the infalling galaxy deposited material at $r = 120''$, and we used Δt_0 to be the time since the infalling galaxy deposited material at $r = 120''$.

In order to reduce the number of possible parameters, we decided to restrict the starting point of the numerical integration to the particular family of initial conditions described below. We began our orbit at a radius from the nucleus that is of the same order as the impact parameter of the encounter which is estimated to be roughly $b = 15'$ from the nucleus. Close to circular orbits for the infalling galaxy were chosen, since Huang and Stewart (1987) found that coherent and concentric shell structures (as observed in Cen A) resulted from this type of orbit. We assume our potential was prolate with z-axis along the extended direction. Because the potential we used is rotationally symmetric, we only consider incoming trajectories with a velocity vector that lies in the $x - z$ plane

$$\vec{v} = v_0(\sin\delta, 0, \cos\delta), \tag{5.18}$$

where δ is the angle between the velocity vector and the z axis. For a straight-line trajectory, the position of closest approach, $\vec{b}$, can be parametrized by b_0 and ϵ, where ϵ is the angle between b and the x-axis and $\vec{b}$ is given by

$$\vec{b} = b_0(\sin\epsilon\cos\delta, \cos\epsilon, -\sin\epsilon\sin\delta). \tag{5.19}$$

We arbitrarily began our integrations at this point $\vec{b}$ with velocity $\vec{v}$ and mass M_s given by equation (5.14). We treated b_0, v_0, δ and ω_0 as free parameters, where the initial inclination, ω_0, of the orbit is given by $\cos\omega_0 = -\cos\epsilon\sin\delta$. We searched parameter space for orbits that displayed inclination changes similar to those needed to model our infrared data.

Figure 14 shows the results of an integration for the orbit with initial conditions and parameters summarized in Table 3. For our integration we chose $\sigma_s/\sigma_e = 1/3$ (see §5.1 for discussion), and $q = 1/0.8$ (0.8 is the axis ratio of of the optical isophotes (Dufour *et al.* 1979). Since the approximations that went into this integration were crude, our results are intended to be mostly illustrative rather than predictive.

Figure 14a shows $\omega(r)$ (solid line) from the integration and the function (dotted line) we used to generate our infrared models (Figures 7b-12b). Large changes in inclination are present in this integration, in particular the inclination is much higher at large radii than at smaller radii. In a galaxy in which the velocity dispersion is close to isotropic, dynamical friction not only circularizes an orbit (Casertano, Phinney and Villumsen 1987), but also may cause an orbit to settle onto the principal plane of a galaxy.

Figure 14b shows the mass density as a function of radius of material stripped from the infalling galaxy. Material is stripped continuously at radii greater than $r = 7'$ and dM/dD is roughly constant, as we estimated in §5.1. There is also material stripped at radii less than $3'$, the location of the innermost shell (Malin *et al.* 1983), and where the dust lane is found. However there is a gap in radii where no material is stripped for $r = 3' - 7'$. This gap results from an apocenter in the infalling orbit. When the orbit of the infalling galaxy is sufficiently elliptical, there can be regions of the orbit that are far enough away from the nucleus that stripping will cease (Dupraz and Combes 1987). We note that Malin *et al.* (1983) had difficulty accounting for the location of this inner shell and the size of the gap separating it from the others assuming that Cen A resulted from one accretion event. The results of our integration seem to provide a natural explanation for this gap.

Figure 14c displays $\alpha(r)$ at the present time (solid line) with $t(r = 120'') = 6.0 \times 10^7$ yr since the infalling galaxy was at $r = 120''$. The dotted line in this figure is $\alpha(r)$ from our previous model (equation 3.4). A constant has been added to the result of the integration in order to match the precession angle of our previous model at $r = 120''$. The resulting precession angle $\alpha(r)$ is well fitted by a function that is proportional to of the angular rotation rate Ω and so is consistent with the precession model (Tubbs 1980), (and the geometry we used to model the infrared data) but has been generated by our integration which allows the gas to precess since the time of stripping. Our integration confirms our result of §5.1 that the precession angle can be well described by a function that is identical to the precession model in which the initial condition is a planar configuration for the gas. The primary difference between the results of the integration and our previous model (§3.1) consists of changes in inclination.

Material from the infalling galaxy currently at radius r has angular momentum vector given by $\alpha(r)$ (Figure 14c) and $\omega(r)$ (Figure 14a). At a radius $r \sim 6'$, the orientation of the angular momentum vector has $\omega = 45^\circ$ and $\alpha \approx 240^\circ$. Using equations (7.3) and (7.4) from (QZPP) we find this vector has a position angle on the sky of $\sim -20^\circ$ which is consistent with the rotation axis of planetary nebulae at $8' < r < 20'$ observed by (Ford *et al.* 1989 and Hui 1990) at a position angle of about -25° and the rotation axis observed from HI in this same region (J. van Gorkom private communication). We note that this axis of rotation is coincident with the direction of stellar rotation observed by Wilkinson *et al.* (1986). Our integration is also consistent with the rotation axis of the gas in the inner region ($r < 70''$) which has a position angle of $\sim 30^\circ$. We find that our integration provides a natural explanation for the observed large change in the position angle of the rotation axis.

From our integration we estimate that the time since the spiral galaxy was at the position of the outer stellar shells at $\sim 15'$ (Malin *et al.* 1983) was 1.6×10^8 yr. At this radius the dynamical time $t_D \approx 4.5 \times 10^7$. This time is shorter than our estimate given in equation (5.11). Huang and Stewart (1987) found that sinking times in non-spherical potentials were significantly smaller than those in spherical ones. We note that our estimated time is not long enough to produce the number of observed stellar shells at this radius ($r \sim 15'$) assuming that these shells originated from one accretion event. However, if material is stripped at a variety of different radii (as is seen in our integration) more shells would be produced. At this timescale, the gas has not had time to shear out completely into a ring, and so the individual gas clouds stripped should not have collided with themselves. We do not expect the gas at this radius to have settled onto a planar surface. Emission from atomic hydrogen emission observed aligned with these shells (J. van Gorkom, talk given at the Third Teton Astronomy Conference July 1992, private communication) supports our short estimate for the timescale since the merger, since we would expect the gas to be on the same orbits as stars stripped from the infalling galaxy.

6. DISCUSSION AND SUMMARY

In this paper we present new large scale infrared mosaics in J,H and K of the dust lane of Cen A. By integrating the light of the galaxy through an absorptive warped disk, we successfully model the morphology and colors of our data. The model we used for the geometry of the warped disk is consistent with kinematics of the CO (QZPP) and Hα (Nicholson *et al.* 1992) data.

Elongation along the direction of the soft X-ray jet in the isophotes at J and H is not predicted at the nucleus in our models, so we support the interpretation (Joy *et al.* 1991) of this elongation as evidence for an infrared jet. We do not observe a shift in the position of the nucleus (reported by Giles 1986) with respect to the K nucleus in our models at J and H. This shift could be caused by the circumnuclear disk observed by (Israel *et al.* 1990), which is not part of our model.

Observed extensions of the K isophotes $30 - 50''$ from the nucleus, are not predicted in our model. A likely explanation is that they are caused by emission from the disk. We find that it is unlikely that this emission is from HII regions or from red giants and supergiants in the disk, but that this emission may be from thermally fluctuating small hot dust grains. This is unexpected since excess brightness at K in star forming galaxies is usually due to red giants and supergiants. It is surprising that the physical conditions in the disk of Cen A could be similar to those found in reflection nebulae, but on a galactic scale. Higher quality near and far infrared observations of the disk of Cen A are needed to confirm this possibility.

Our model is consistent with existing X-ray observations of Cen A. In Figure 13, we show an X-ray transmission map predicted by the model, that can be compared to future higher resolution X-ray observations of Cen A. We find that some of the high X-ray opacity near the nucleus is caused by the location of a fold in the gas and dust disk near the nucleus. If the orientation of the galaxy with respect to us were slightly different, we would expect the X-ray opacity at the nucleus to be reduced. Observation of a one–sided soft X-ray jet (Feigelson *et al.* 1981) is not explained by our model.

We find that the model for the geometry of the warp needed to reproduce the morphology of our near-infrared mosaics, has a precession angle identical to that successfully used to model the kinematics of the CO data (QZPP) for $r < 70''$, which is derived assuming that the disk has evolved as result of differential precession (Tubbs 1980). However, the disk has an inclination, with respect to the principal axes that is higher at larger radii than in the inner region, and so is inconsistent with precession from an initially planar system. Since the timescale needed to create the warp is short ($\approx 10^8$ years) (Tubbs 1980, QZPP), it is unlikely that settling onto the principal plane of the galaxy could have occurred on this timescale.

In §5, we propose a scenario in which gas stripped tidally from an infalling galaxy forms a ring with radius and orientation determined by the angular momentum of the infalling galaxy at the time of stripping. Afterward, the gas rings are free to precess in the potential of the underlying galaxy. Stripping at different times during the infall produces a smoothly connected system of rings, or a warped geometry for the gas. In a non-spherical potential, the orbit of the infalling galaxy is not constrained to lie on a plane, so that the resulting inclination of the gas rings with respect to the principal axes of the potential is not expected to be constant as a function of radius.

In §5, by considering the infall under dynamical friction of a small isothermal sphere into a larger one, we find that under certain conditions (the orbit of the infalling galaxy is close to circular and is on a plane, and the underlying galaxy has constant ellipticity), the resulting gas configuration is identical to that described by the precession model in which the gas is assumed to be initially on a plane (Tubbs 1980). By numerically integrating an orbit, we find that there can be large changes in inclination of the gas as a function of radius, but that the precession angle can still be described by the precession model (Tubbs 1980). We find an orbit that not only reproduces the changes in inclination needed to reproduce the morphology of our mosaics, but also reproduces the gap in the stellar shells observed by Malin *et al.* (1983). This orbit also provides a natural explanation for the difference in the rotation axis observed from planetary nebulae, (Ford *et al.* 1989 and Hui 1990) and HI (J. van Gorkom, private communication) in the outer part of the galaxy, and the rotation axis of the gas in the inner region ($r < 70''$). From our orbit we find that the time since the merger (since the infalling galaxy was at $\sim 15'$ from the nucleus) is remarkably short (1.6×10^8 years). While observations of HI aligned with stellar shells in this region (J. van Gorkom, private communication) suggest a short timescale, it is possible that we could have underestimated the timescale due to the crudeness of the numerical integration of our orbit.

The gas in AGNs is observed to be nonplanar and misaligned from the host galaxy in both radio Seyferts (Unger *et al.* 1987; Haniff, Wilson and Ward 1988), and in radio ellipticals (Sansom *et al.* 1987). Our scenario suggests one mechanism for how gas can become nonplanar and misaligned within the host galaxy.

It has recently been proposed by Thomson (1992) that part of the spiral galaxy that was involved in the merger of Cen A was ejected and formed the Fourcade Figueroa shred (an apparently irregular blue galaxy a few hundred kiloparsecs from Cen A). This is a fascinating possibility. In their scenario, the core of the spiral galaxy escapes after the collision and forms a dwarf elliptical galaxy. While it is possible that material could have been ejected during the merger, it is unlikely that the core of the spiral galaxy did not merge into the large elliptical galaxy.

It has been suggested that warped disks could be used to probe the three-dimensional mass distribution of galaxies (Steiman-Cameron *et al.* 1990). We find that in a galaxy in which the warped disk resulted from a merger, such a study may be complicated by the dependence on the final configuration of the disk on the details of the merger. Attempts to probe the potential of host galaxies using stellar shells will be subject to the same complications.

The approximations that went into our numerical integration of the orbit of the infalling galaxy were crude. We hope that the process of the merger of Cen A be will modeled numerically with an N–body code which includes gas particles. Such an experiment could verify our scenario, as well as investigate what happens when the infalling galaxy reaches the nuclear region of the underlying galaxy. Improvements in N-body numerical methods and hydrodynamical codes in the past decade, along with the present detailed knowledge of the gas and stars in Cen A might make reexamination of these issues exciting.

We gratefully thank Daren DePoy and the CTIO staff for help with the observations. Tim de Zeeuw provided the original motivation for this work. This paper could not have been written without his help. I thank the Submillimeter and Infrared Research Groups at Caltech for their support and help. I also acknowledge useful discussions and correspondence with Tim de Zeeuw, E.S. Phinney, Joss Bland-Hawthorn, Jacqueline van Gorkom, S. Sridhar and Bharat Ratra. This research was supported in part by NSF grant AST 90-15755, and NASA grants NAGW-2144 and NAGW-2142.

APPENDIX A. COMPARISON OF CO AND IR MODELS

In this section the infrared warped model is compared to the warped prolate CO model of Chapter 2. In §A.1 predictions for H column density based on the two models are compared. In §A.2 a function for the CO integrated intensity that decays exponentially at large radii is fit to the CO data. In §A.3 the kinematics of the infrared model is discussed.

A.1 *H Column Density*

In this subsection we compare the hydrogen number densities predicted from the CO model integrated intensity (Chapter 2) and the infrared model dust opacity. Our infrared model has opacity at J of $\tau \sim 0.15$ for the disk if it were observed face on for $r < 60''$ (see Table 1 and §3.2). Using the conversion $7 \times 10^{21} N_{\mathrm{H\ atom}} \mathrm{cm}^{-2}/A(J)$ mag (Mathis 1990), we estimate from our model infrared opacity that $N_{\mathrm{H\ atom}} \sim 10^{21}\mathrm{cm}^{-2}$. Since the colors of our infrared models roughly match the colors of the data, our infrared opacity is consistent with the line-of-sight hydrogen column densities estimated by Harding *et al.* (1981) $(4 - 8 \times 10^{21}\mathrm{cm}^{-2})$.

From our fit to the CO data we found an integrated intensity for the disk of $\sim 15 K\,\mathrm{km\,s}^{-1}$ (if observed face on in the same region). Using the conversion factor cited in equation 5.2 of Chapter 4, we find $N_{\mathrm{H\ atom}} \sim 8 \times 10^{21}\mathrm{cm}^{-2}$ which is consistent with the line-of-sight estimate of Phillips *et al.* (1988) and the estimate of Marston and Dickens (1988) from their far infrared observations; (assuming a typical galactic dust to gas mass ratio of 160, they find find a column density of $N_H \sim 10^{22}\mathrm{cm}^{-2}$). The estimate for N_H based on the dust opacity is lower than that based on CO emission.

Since the molecular clouds in the disk have a low area filling factor, which would have a high infrared (and X-ray) opacity, one possibility is that the average infrared (and X-ray) opacity is primarily determined by a more diffuse component of the ISM. This would explain why using the galactic extinction ratios (see §3.2) (which would not be consistent with optically thick 'bricks') is successful at reproducing the morphology of the infrared mosaics in the three colors. The assumption of a one component opacity for the infrared models then can underestimate the gas density in the disk. We note that the FWHM of the function used to describe the dust opacity as a function of radius (equation 3.2) is much wider than FWHM of the function used to described the CO integrated intensity (see §5.1 Chapter 2). When using a function proportional to equation (3.2) to describe the CO integrated intensity, predicts an excess of CO emission at large radii when compared to the observations. This suggests that the less dense component of the ISM extends to larger radii than where we detect CO emission. We note that the estimate for N_H based on the infrared opacity is consistent with HI observations outside where we detect CO (line-of-sight column densities of $10^{21}-10^{22}\mathrm{cm}^{-2}$, van Gorkom *et al.* 1990). Our infrared model did not include scattering by the dust, or the stellar component of the disk. Consideration of these processes should also increase an estimate of the N_H based on the near infrared transmission properties of the disk.

A.2 *CO Surface Intensity Variation*

In this subsection we vary the form of the azimuthally averaged CO surface intensity as a function of radius. In our CO models we assumed a form for this function that was Gaussian (a function parametrized by only the dispersion). We chose this function originally because it is possible to fit previous CO observations (Phillips *et al.* 1987) of the integrated CO intensity as a function of distance from the nucleus with a Gaussian. However these observations were done with a beam size of 30" (FWHM) and so the integrated intensity per beam does not provide much information about the form of the integrated intensity function. We might hope that our increased understanding of the disk geometry coupled with a fit to the shapes of the spectra, might be able to constrain the shape of this function.

We consider a form for the integrated intensity that decays exponentially at large radii, yet is not peaked in the center (equation 3.2). This function is described by two constants: b, the radius at which the function begins to decay and an exponential decay rate, σ_{CO} (which is denoted by σ_τ in equation 3.2). As stated in the previous subsection, we found that a function for the CO surface intensity that is directly proportional to our model J opacity ($b = 80$, $\sigma_\tau = 80$) predicted more CO emission at large radii than is observed. A slight increase in the quality of the fit (which is not significant) is found with $b = 40''$ and $\sigma_{CO} = 40''$. A function with a molecular ring (which would require even more parameters to describe) was not explored. The CO intensity and near infrared opacity of the disk is largest at the folds of the disk. A better model for the warp which more precisely determines the location and extent of the folds is required in order to measure variations in the azimuthally averaged CO surface intensity or dust opacity as a function of radius.

A.3 *Kinematics of the Infrared Model*

With the code that constructed the CO models (Chapter 2), we compute the line-of-sight velocities with the geometry for the warp used to construct the near infrared model. Athough the inclination of the disk for the infrared model rises at small radii, the inclination angle of the potential (θ) is slightly lower (by 5°) than for the CO model (see Table 1), so the average inclination angle of the disk is similar to that of the CO model. Figure 15 displays the line-of-sight velocities and integrated intensities for this model. The velocity field in the inner region is similar to the velocity field of the prolate CO model discussed in Chapter 2 (displayed in Figure 8) and so agrees with the Hα velocity field (Bland *et al.* 1987). However, the integrated intensity of the model is concentrated over a smaller area on the sky, and so provides an inferior fit to the CO data. A combined fit to both the infrared and CO data with a more realistic form for the ellipticity of the potential used to parametrize the warp would provide a better fit to both data sets.

> ‘ “I know what you’re thinking about,” said Tweedledum; “but it isn’t so, no-how.” “Contrariwise,” continued Tweedledee, “if it was so, it might be; and if it were so, it would be; but as it ain’t, it ain’t. That’s logic.” ’
>
> — Lewis Carroll, *Through the Looking Glass*

TABLE 1

MODEL PARAMETERS

Background Galaxy Parameters[1]		
μ	0.05	
r_0	$168''$	
r_1	$15''$	
Dust Parameters[2]		
B_J	0.15	
b	$80''$	
σ_τ	$80''$	
Warp Parameters[3]		
	Infrared model[4]	CO model[5]
ϑ	$65°$	$60°$
χ	$30°$	$35°$
A (km s^{-1})	300	300
c	$40''$	$40''$
σ_{el}	$80''$	$80''$
α_0	$-182°$	$-182°$
$\epsilon_\infty \Delta t$ (years)	2×10^7	2×10^7
ω	——[6]	$25 \pm 5°$

[1] See §3.1 for description of parameters. [2] See §3.2. [3] See §3.3. [4] Displayed in Figures 7-13. [5] From QZPP. [6] See function shown in Figure 14a.

TABLE 2

Nuclear Offsets from Star A

	$b = 2$			$b = 5$		
Filter	ΔRA	ΔDec	Uncertainty	ΔRA	ΔDec	Uncertainty
J	42.89	13.08	±0.3	42.61	12.68	±0.3
H	41.52	13.59	±0.2	41.72	13.67	±0.2
K	41.02	13.53	±0.2	41.22	13.48	±0.2

Star A is the bright star approximately 42″ West and 13″ North of the nucleus. The location of the nuclear position is the centroid in a box of width b in pixels. A pixel is 0.89″. Offsets are in arcsecs.

TABLE 3

Parameters for Integration of Orbit[1]

ω_0	35°
δ	65°
b_0	45′
v_0 (km s^{-1})	410
η	2
σ_s/σ_e	1/3
q	1.2
[2]$t(r = 120'')$ (years)	6×10^7

[1] Displayed in Figure 14. See §5 for details. [2] Time since the infalling galaxy reached $r = 120''$ from the nucleus.

REFERENCES

Baade, W., & Minkowski, R. 1954, *Ap. J.*, 119, 215

Becklin, E.E., Frogel, J.A., Kleinmann, D.E., Neugebauer, G., Ney, E.P., & Strecker, D.W. 1971, *Ap. J.*, 170, L15.

Begeman, K. 1987, *HI Rotation Curves of Spiral Galaxies*, PhD Thesis, Rijksuniversiteit Groningen

Binney, J., & Tremaine, S. 1987, *Galactic Dynamics* (Princeton U. Press).

Bland, J., Taylor, K., & Atherton, P.D. 1987, *M.N.R.A.S.*, 228, 595 (BTA).

Casertano, S., Phinney, E.S., & Villumsen, J.V. 1987, in IAU Symposium No. 127, Structure and Dynamics of Elliptical Galaxies, ed. P.T. de Zeeuw (Dordrecht: Reidel), p. 474.

Dufour, R.J., van den Bergh, S., Harvel, C.A., Martins, D.H., Schiffer, F.H., Talbot, R.J., Talent, D.L., & Wells, D.C. 1979, *A. J.*, 84, 284.

Dupraz, C., & Combes, F. 1987, *Astr. Ap.*, 185, L1.

Eckart, A., Cameron, M., Rothermel, H., Wild, W., Zinnecker, H., Rydbeck, G., Olberg, M., & Wiklind, T. 1990, *Ap. J.*, 363, 451.

Elias, J.H., Frogel, J.A., Matthews, K. & Neugebauer, G. 1982, *A. J.*, 87, 1031.

Feigelson, E.D., Schreier, E.J., Delvaille, J.P., Giacconi, R., Grindlay, J.E. & Lightman A.P. 1981, *Ap. J.*, 251, 31.

Ford, H.C., Ciardullo, R., Jacoby, G.H., & Hui, X. 1989, In IAU Symposium 131, Planetary Nebulae, ed. S. Torres–Peimbert (Dordrecht: Reidel), p. 335.

Frogel, J.A., Persson, S.E., Aaronson, M., & Mathews, K. 1978, *Ap. J.*, 220, 75.

Giles, A.B. 1986, *M.N.R.A.S.*, 218, 615.

Griffin, R.F. 1963, *A. J.*, 68, 421.

Gurskey, H. 1973, "Observations of X-ray Sources" in Black Holes, ed. by C. De Witt and B.S. De Witt, Gordon and Breach New York, p302.

Habe, A., & Ikeuchi, S. 1988, *Ap. J.*, 326, 84.

Haniff, C.A., Wilson, A.S., & Ward, M.J. 1988, *Ap. J.*, 334, 104.

Heckman, T.M., Carty, T. J., & Bothum, G.D. 1985, *Ap. J.*, 288,122.

Heckman, T.M., Smith, E.P., Baum, S.A., van Breugel, W.J.M., Miley, G.K., Illingworth, G., Bothum, G.D., & Balick, B. 1986, *Ap. J.*, 311,526.

Hernquist, L. 1990, *Ap. J.*, 356, 359.

Hernquist, L., & Quinn, P.J. 1988, *Ap. J.*, 331, 682.

Hernquist, L., & Quinn, P.J. 1989, *Ap. J.*, 342, 1.

Huang, S-N. & Stewart, P. 1987, *Astr. Ap.*, 174, 13.

Hui, X. 1990, talk presented at Aspen Workshop on Structure and Dynamics of Galaxies.

Israel, F.P., van Dishoeck, E.F., Baas, F., Koorneef, J., Black, J.H., & de Graauw, Th. 1990, *Astr. Ap.*, 227, 342.

Joy, M., Lester, D.F., Harvey, P.M., & Ellis, H.B. 1988, *Ap. J.*, 326, 662.

Joy, M., & Lester, D.F. 1988, *Ap. J.*, 331, 145.

Joy, M., Harvey, P.M., Tollestrup, E.V., Sellgren, K., Mc Gregor, P.J., & Hyland, A.R. 1991, *Ap. J.*, 366, 82.

Malin, D.F., Quinn, P.J., & Graham, J.A. 1983, ApJ, 272, L5.

Marston, A.P., & Dickens, R.J. 1988, *Astr. Ap.*, 193, 27.

Mathis, J.S. 1990, *Ann. Rev. Astr. Astrophys.*, , 28, 37.

Morini, M., Anselmo, F., & Molteni, D. 1989, *Ap. J.*, 347,750.

Nicholson, R.A., Bland-Hawthorne, J. & Taylor, K. 1992, *Ap. J.*, 387, 503.

Phillips, M.M. 1981, *M.N.R.A.S.*, 197, 659.

Phillips, T.G., Ellison, B.N., Keene, J.B., Leighton, R.B., Howard, R.J., Masson, C.R., Sanders, D.B., Veidt, B., & Young, K. 1987, ApJ, 322, L73.

Quillen, A.C., de Zeeuw, P.T., Phinney, E.S., & Phillips, T.G. 1992, *Ap. J.*, 391, 121 (QZPP).

Renzini, A. 1981 Annales de Physique 6, 87.

Salmon, J.K., Quinn, P.J., & Warren, M. 1989 preprint.

Sansom, A.E., Danziger, I.J., Ekers, R.D., Fosbury, R.A.E., Goss, W.M., Monk, A.S., Shaver, P.A., Sparks, W.B., & Wall, J.V. 1987, *M.N.R.A.S.*, 229, 15.

Sellgren, K. 1984, *Ap. J.*, 277, 623.

Sparke, L.S. 1986, *M.N.R.A.S.*, 219, 657.

Steiman–Cameron, T.Y., & Durisen, R.H. 1988, *Ap. J.*, 325, 26.

Steiman–Cameron, T.Y., Kormendy, J., & Durisen, R.H. 1992 ,*A. J.*, 104, 1339.

Telesco, C.M. & Gatley, I. 1984, *Ap. J.*, 284, 557.

Thomson, R.C. 1992, *M.N.R.A.S.*, 257, 689.

Tonry, J.L. & Schechter, P.L. 1990, *A. J.*, 100, 1794.

Tubbs, A.D. 1980, *Ap. J.*, 241, 969.

Turner, P.C., Forrest, W.J., Pipher, J.L., & Shure, M.A. 1992, *Ap. J.*, 393 , 648.

Unger, S.W., Pedlar, A., Axon, D.J., Whittle, M., Meurs, E.J.A., & Ward, M.J. 1987, *M.N.R.A.S.*, 228, 671.

van Albada, T.S., Kotanyi, C.G., & Schwarzschild, M. 1982, *M.N.R.A.S.*, 198, 303.

van Gorkom, J.H., van der Hulst, J.M., Haschick, A.D., & Tubbs, A.D. 1990, *A. J.*, 99, 1781.

Wilkinson, A., Sharples, R.M., Fosbury, R.A.E., & Wallace, P.T. 1986, *M.N.R.A.S.*, 218, 297.

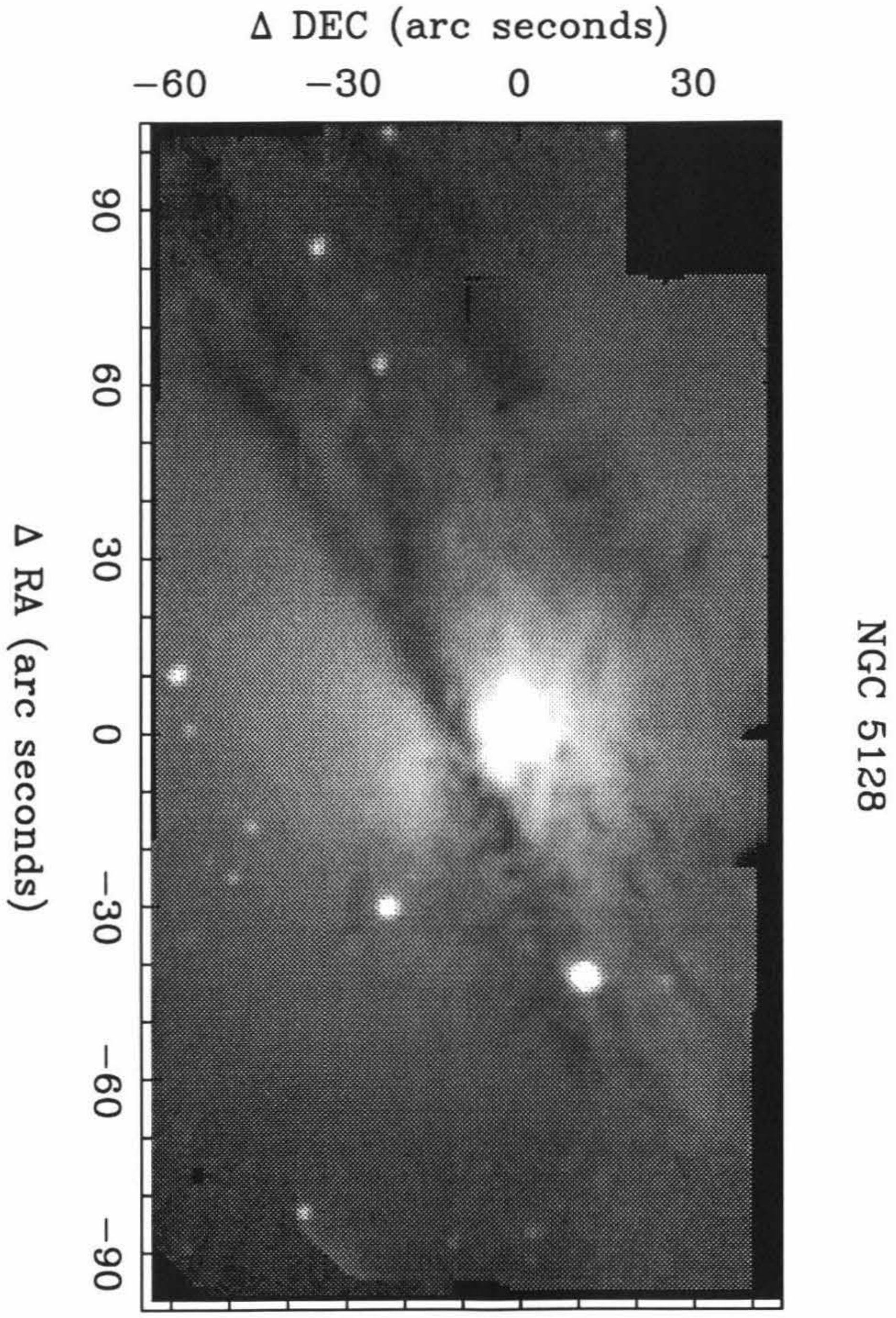

Figure 1. J (1.24 μm) mosaic in magnitudes per square arcsec. The range shown is 15.0 to 18.0 magnitudes per square arcsec. See Figure 7a for detail at the nucleus.

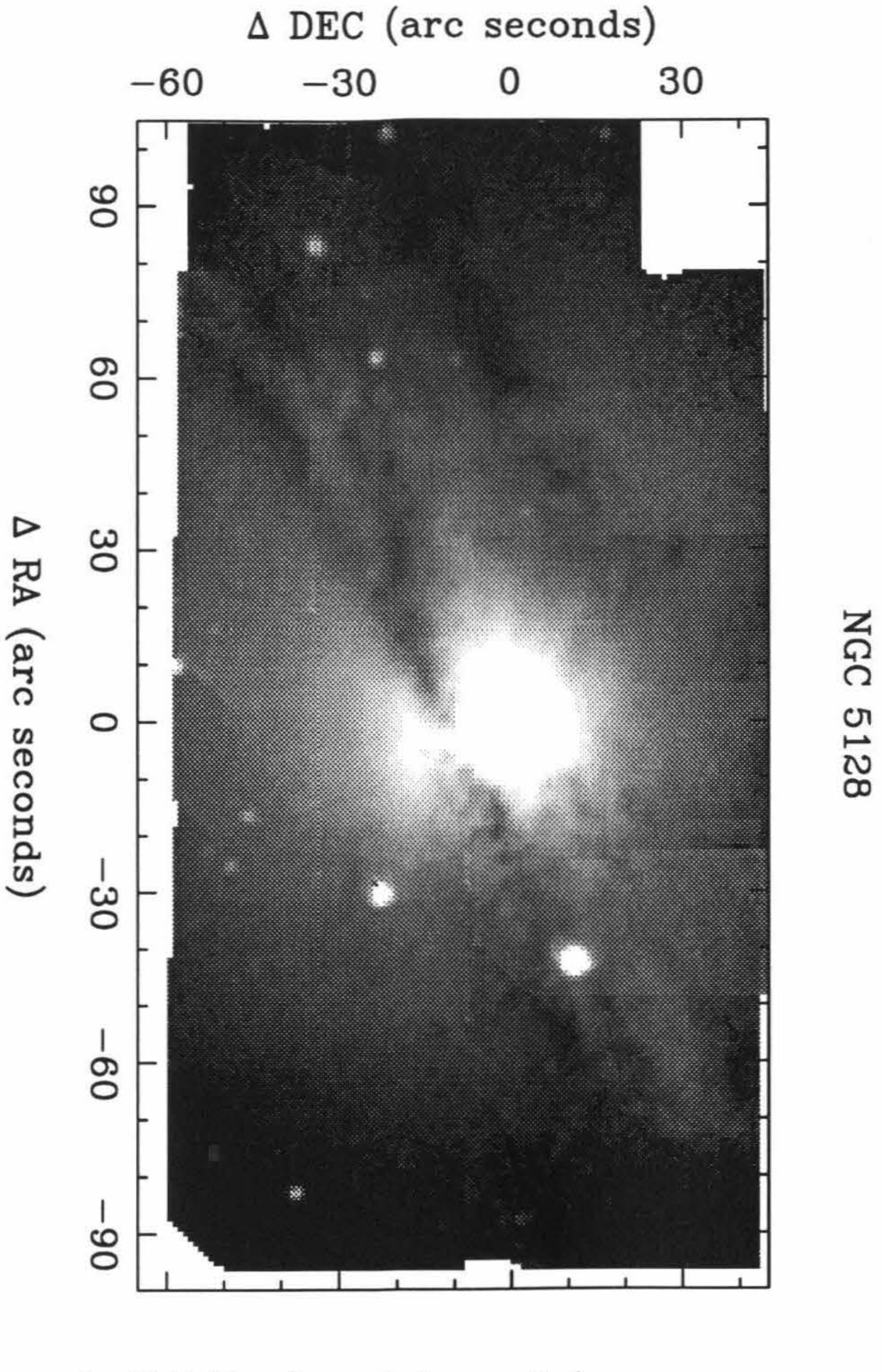

Figure 2. H (1.65 μm) mosaic in magnitudes per square arcsec. The range shown is 14.8 to 17.0 magnitudes per square arcsec. See Figure 8a for detail at the nucleus.

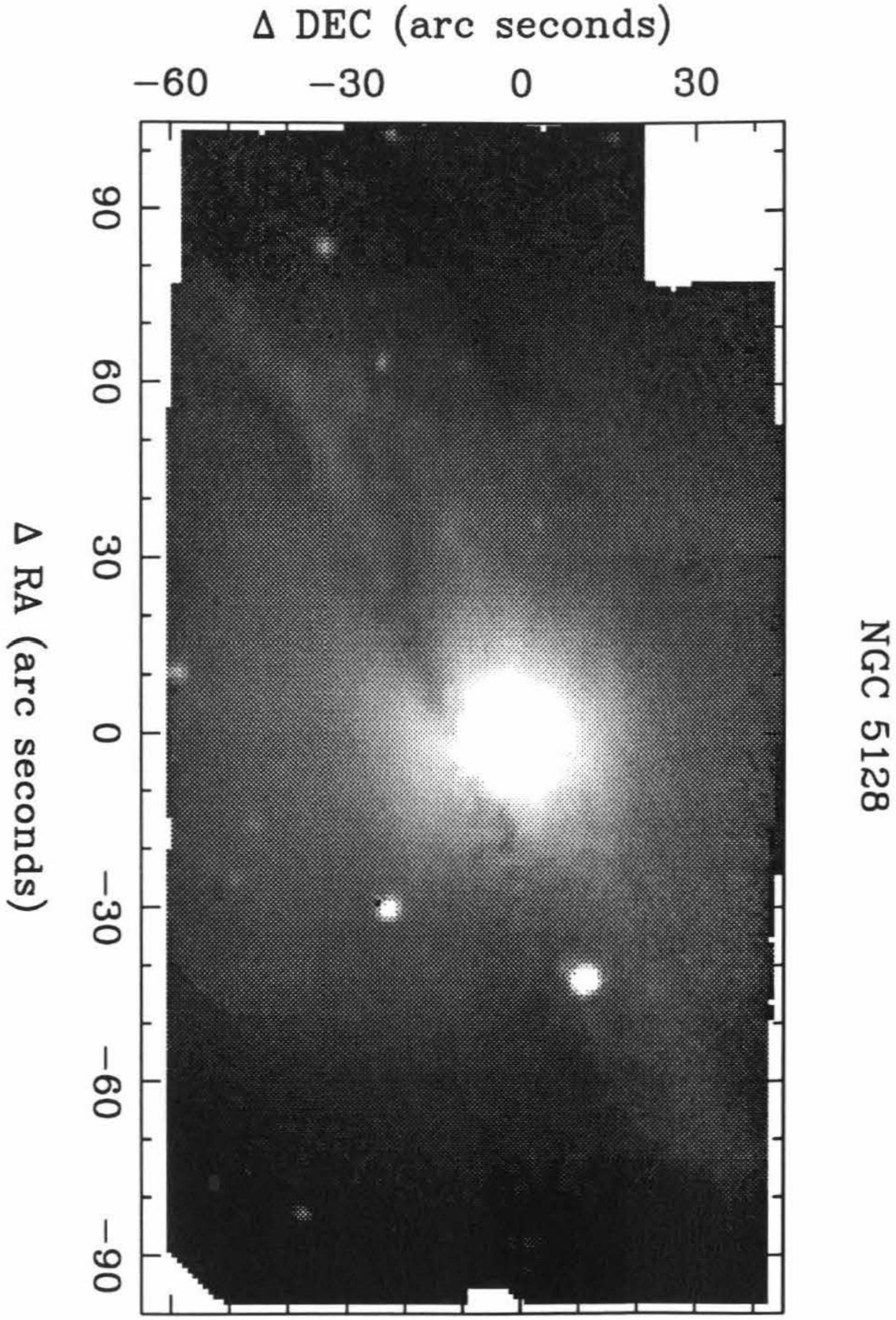

Figure 3. K (2.16 μm) mosaic in magnitudes per square arcsec. The range shown is 14.0 to 16.5 magnitudes per square arcsec. See Figure 9a for detail at the nucleus.

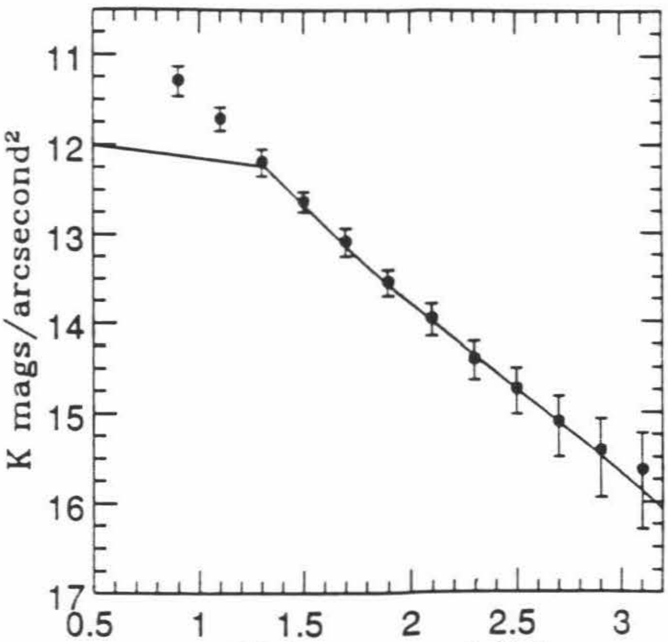

Figure 4. Surface brightness at K in magnitudes per square arcsecond vs. $r^{1/4}$. The points are at the average surface brightness of a wedge of the K mosaic that is 10 degrees wide extending from the nucleus to the eastern edge of the mosaic. The error bar widths are determined from the scatter of the pixels used in the average, and the uncertainty in the underlying sky level. The solid line is the surface brightness from an integration of the light density we used to model our data (see Table 1 for the parameters of the model). The model at $r < 3''$ ($r^{1/4} < 1.3$) gives a poor fit to the data because the resolution of the model is $3''$.

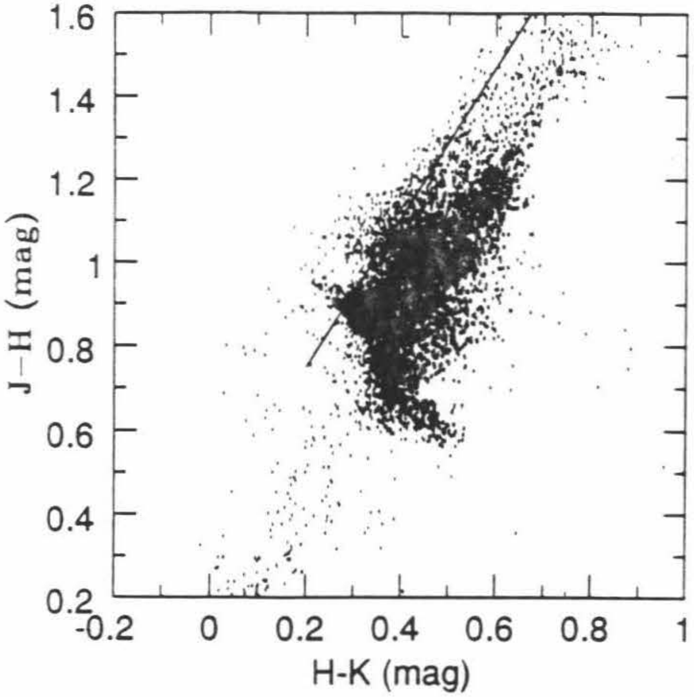

Figure 5. Color-Color map J-H vs H-K for the pixels in the three mosaics, excluding the right hand side of the mosaic (those pixels with RA offset greater than 30″ from the position of the nucleus). The side of the mosaic was excluded because of the inferior quality of the data on this side of the mosaic (see §2). The solid line is at the slope of the reddening line and begins at the position of the color of an old stellar population (Frogel *et al.* 1978). Offsets from this line are not significant since they are within the photometric accuracy of our mosaic.

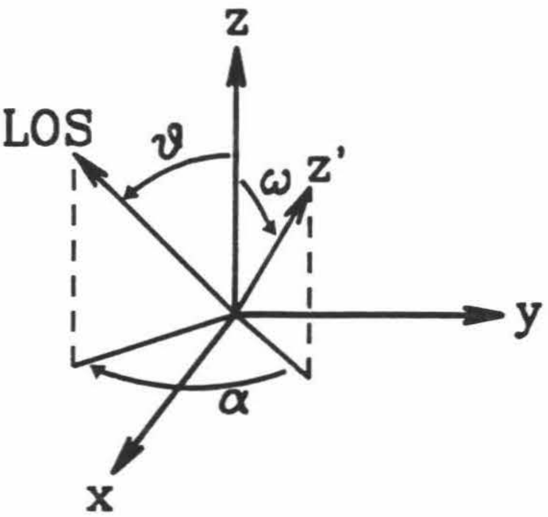

Figure 6. Definition of angles used to described the warped disk. The x, y and z axes are the principal axes of the potential. The z' axis is the axis of symmetry of the ring represented by the dotted ellipse. LOS is the line of sight. See §3.3 for further details.

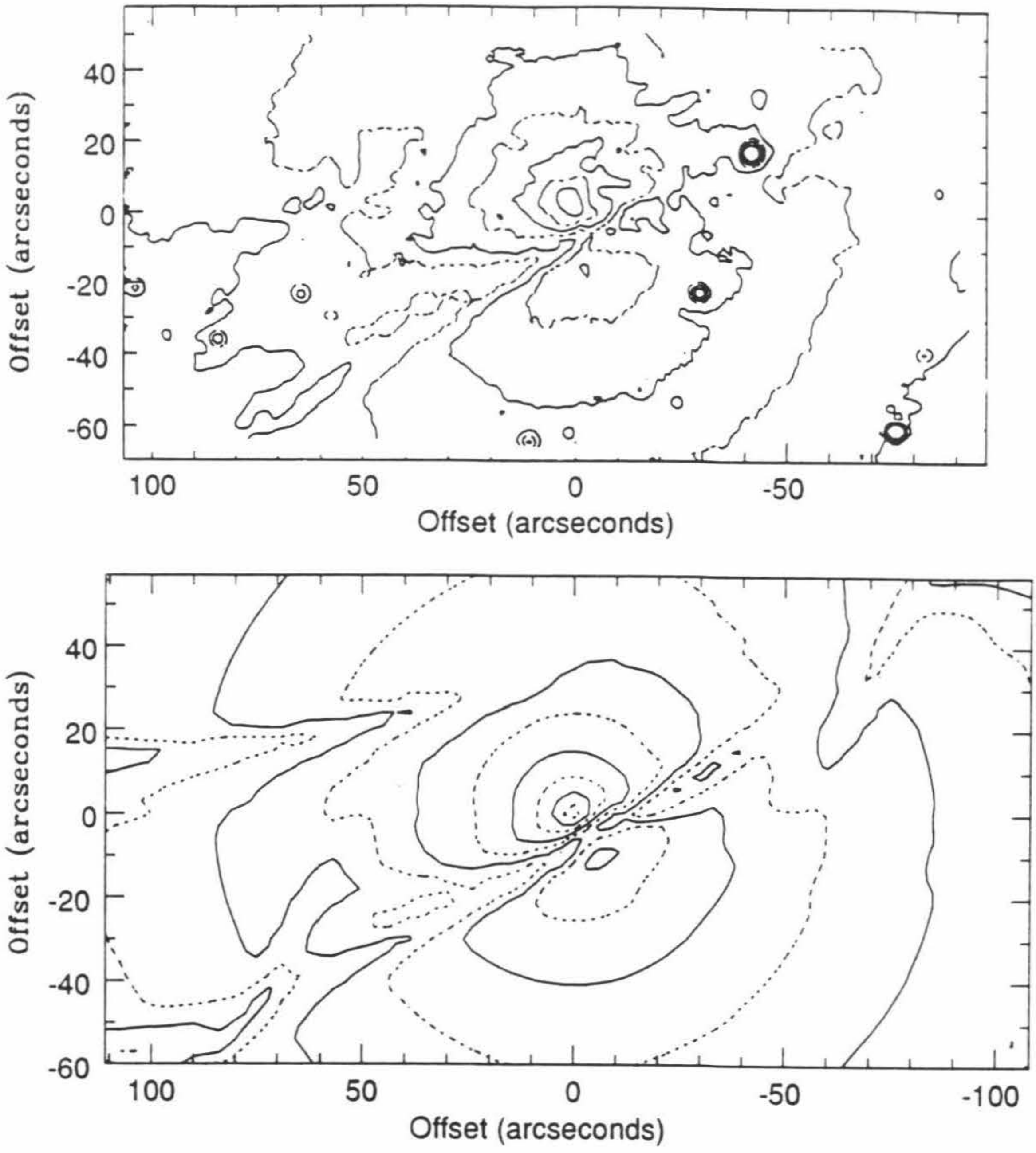

Figure 7. a) J mosaic. The contour interval is 0.5 magnitudes per square arcsecond with the lowest contour at the nucleus at 14.0. Brighter contours for the star 40″ to the west of the nucleus are not shown. Solid contours are at integer levels and dotted contours are at half integer levels. For $r > 40''$ from the nucleus, the data has been smoothed with a Gaussian with FWHM of 2″. Offsets are from the position from the nucleus at K. North is up and East is to the left. b) J model at same contour levels. Parameters for this model are given in Table 1. See text for further details.

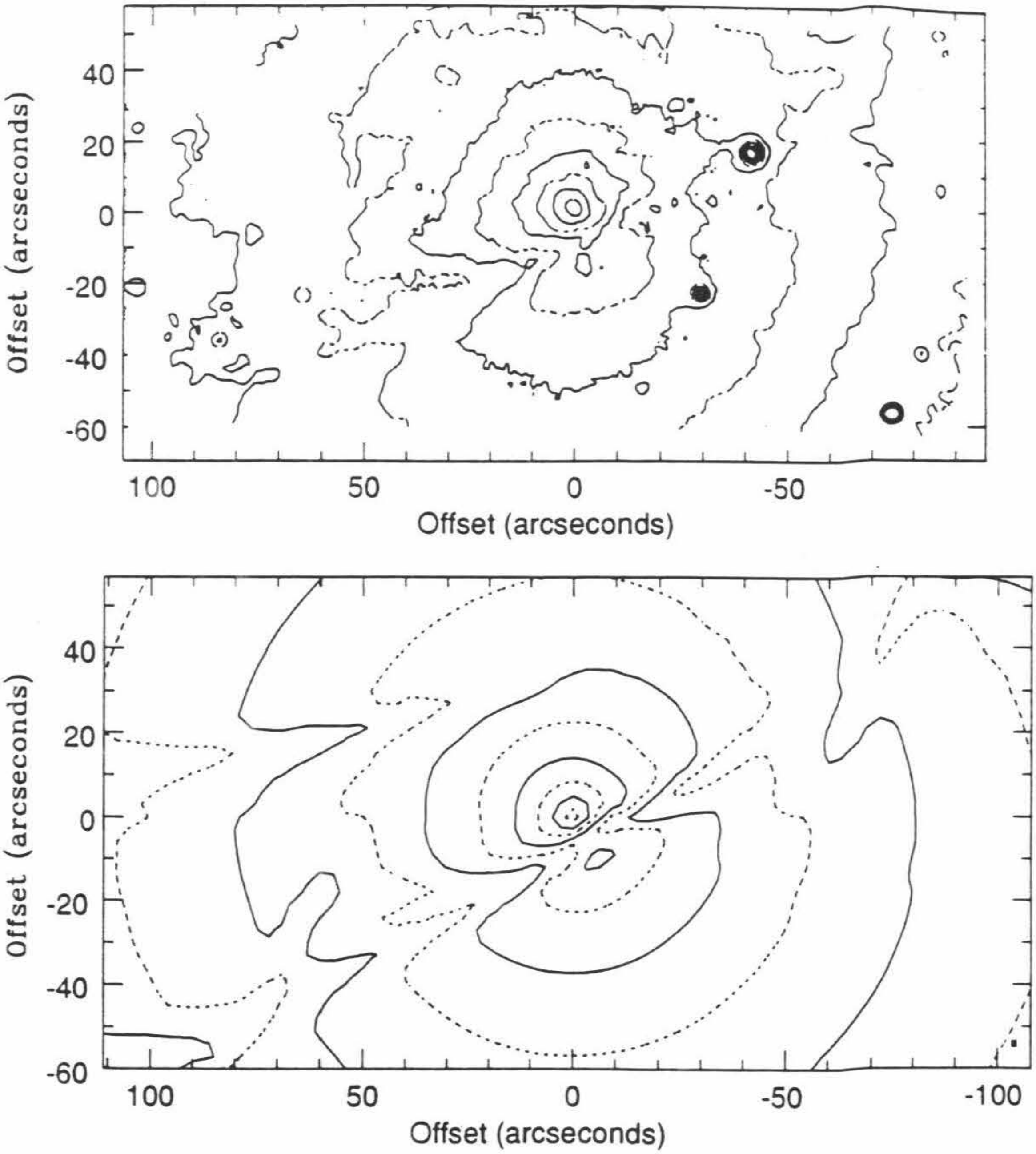

Figure 8. a) H mosaic. The contour interval is 0.5 magnitudes per square arcsecond with the lowest contour at the nucleus at 12.5. Brighter contours for the star 40″ to the west of the nucleus are not shown. Solid contours are at integer levels and dotted contours are at half integer levels. For $r > 40''$ from the nucleus, the data has been smoothed with a Gaussian with FWHM of 2″. Offsets are from the position from the nucleus at K. b) H model at same contour levels.

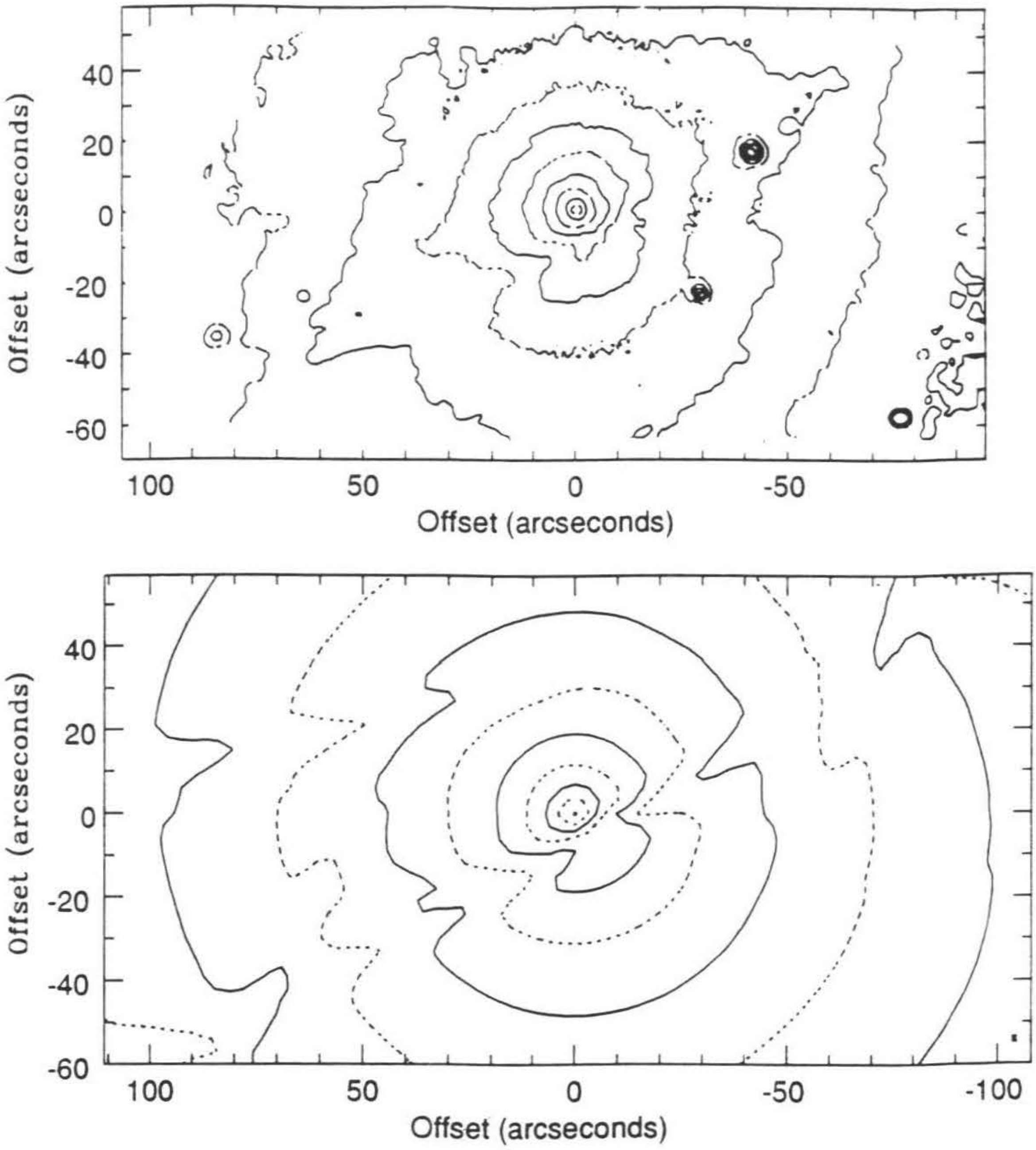

Figure 9. a) K mosaic. The contour interval is 0.5 magnitudes per square arcsecond with the lowest contour at the nucleus at 11.5. Solid contours are at integer levels and dotted contours are at half integer levels. For $r > 40''$ from the nucleus, the data has been smoothed with a Gaussian with FWHM of $2''$. Offsets are from the position from the nucleus at K. b) K model at same contour levels.

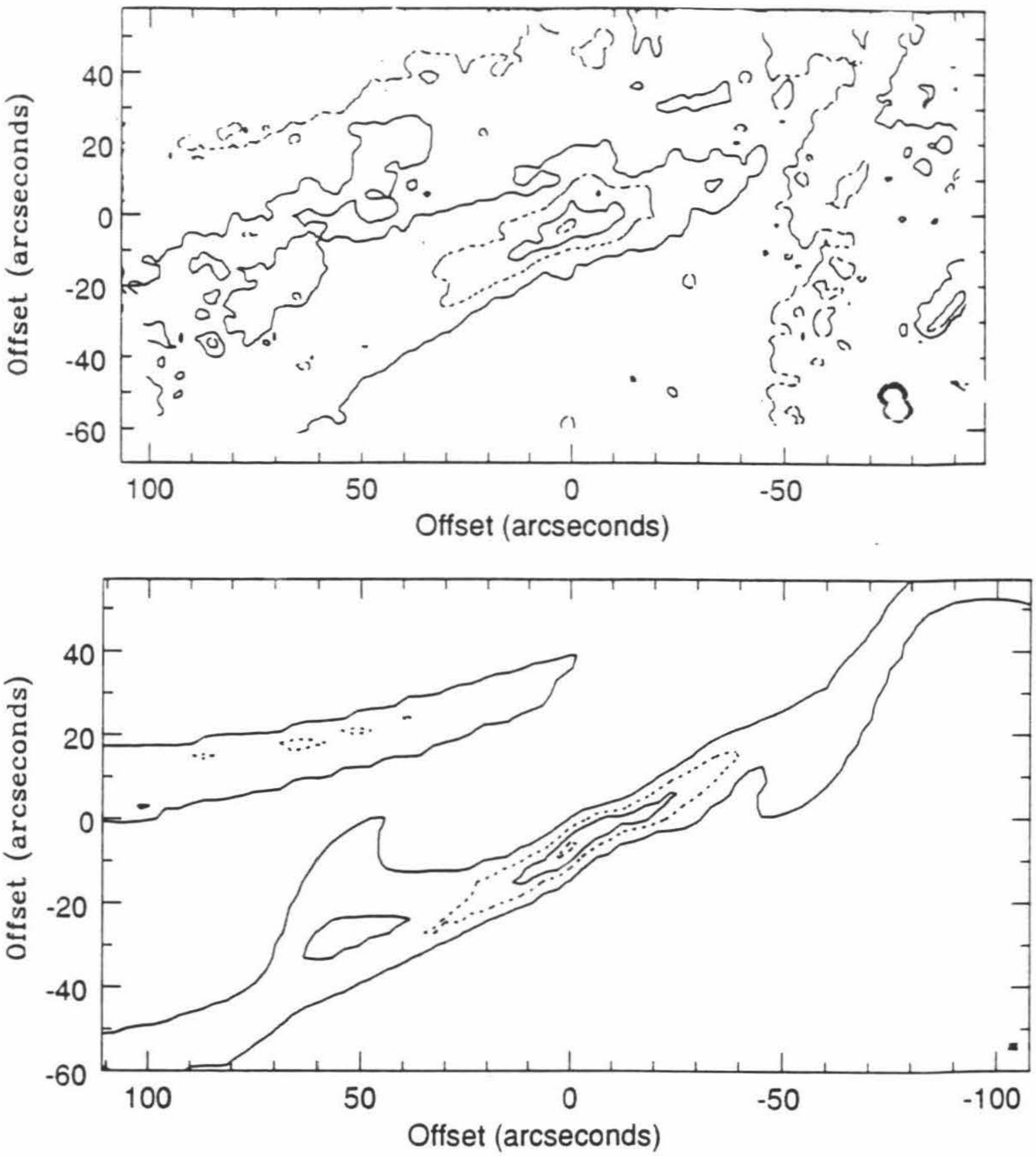

Figure 10. a) J-H mosaic. The contour interval is 0.25 magnitudes per square arcsecond with the highest contour at 1.75. Solid contours are at multiples of 0.5 and dotted contours are at levels in between the solid contours. The data has been smoothed with a Gaussian with FWHM of 2″. Offsets are from the position from the nucleus at K. b) J-H model at same contour levels.

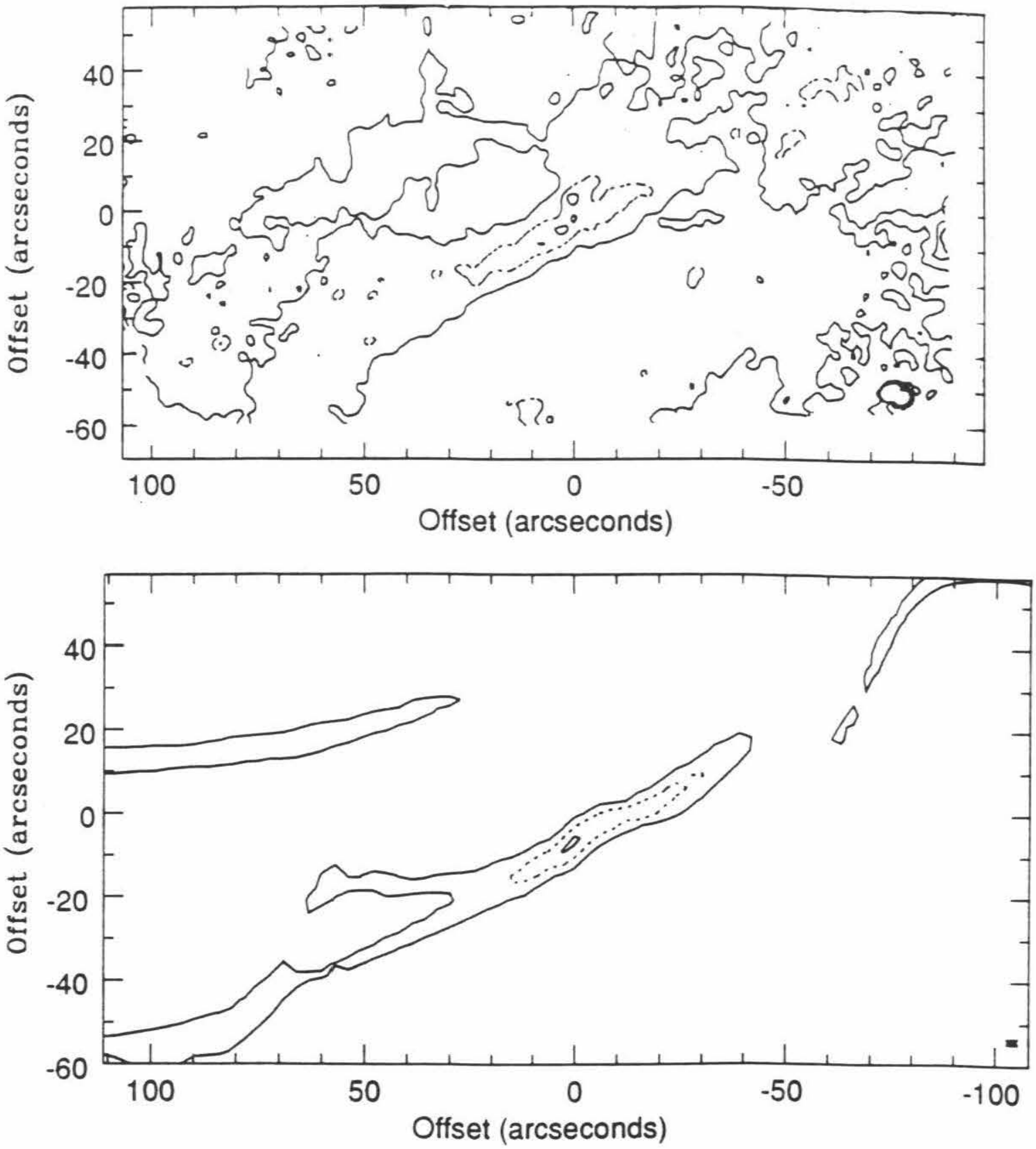

Figure 11. a) H-K mosaic. The contour interval is 0.2 magnitudes per square arcsecond with the highest contour at 0.65. The spacing between the solid contours is 0.4 beginning at 0.45, and dotted contours are at levels in between the solid contours. The data has been smoothed with a Gaussian with FWHM of 2″. Offsets are from the position from the nucleus at K. b) H-K model at same contour levels.

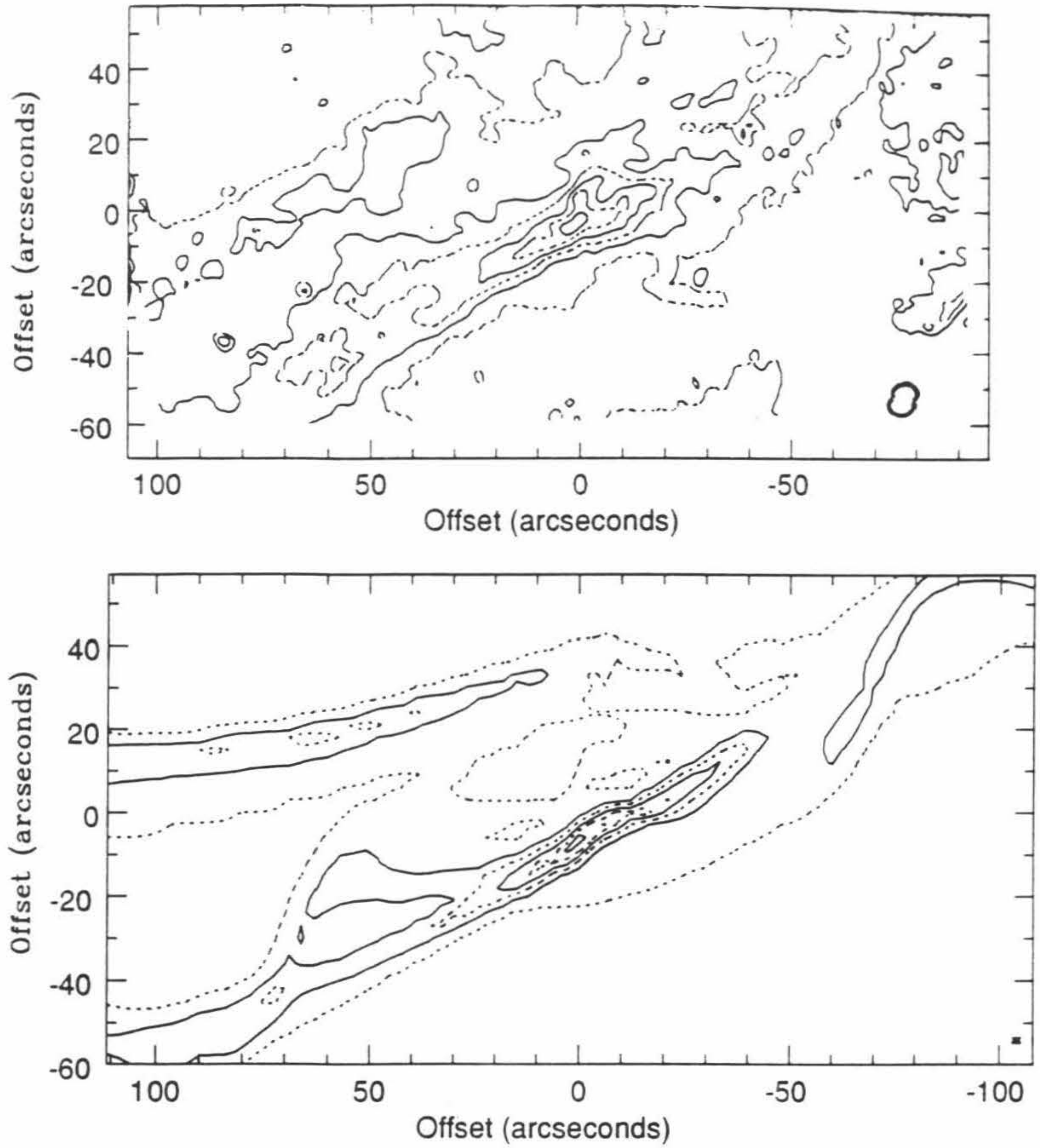

Figure 12. a) J-K mosaic. The contour interval is 0.25 magnitudes per square arcsecond with the highest contour at 2.5. Solid contours are at multiples of 0.5 and dotted contours are at levels in between the solid contours. The data has been smoothed with a Gaussian with FWHM of 2″. Offsets are from the position from the nucleus at K. b) J-K model at same contour levels.

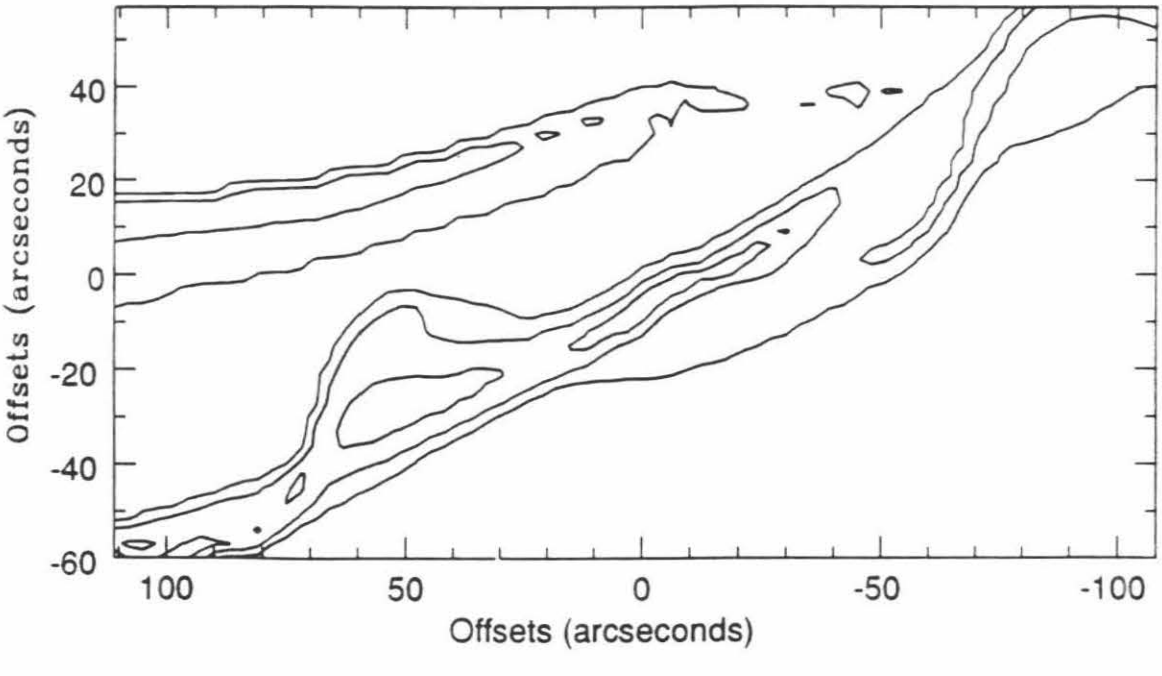

Figure 13. Contour map of the energy of X-rays at which $\tau = 1$ from our model. Contours are at 400, 800 and 1200 eV. See §4.4 for details.

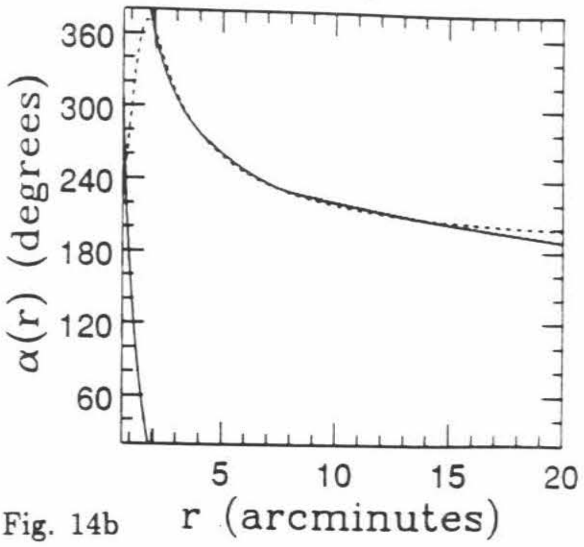

Fig. 14b

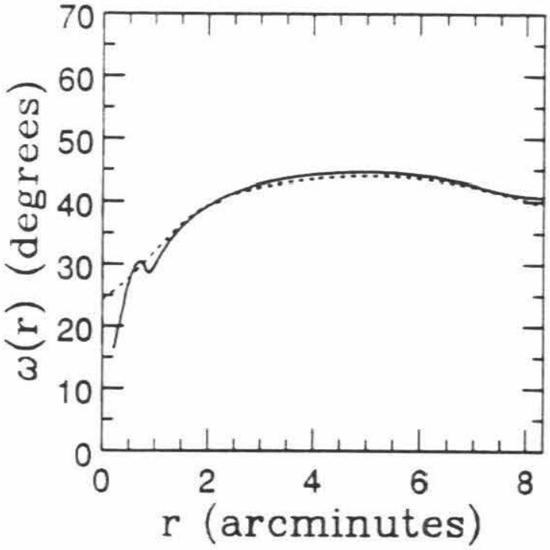

Fig. 14a

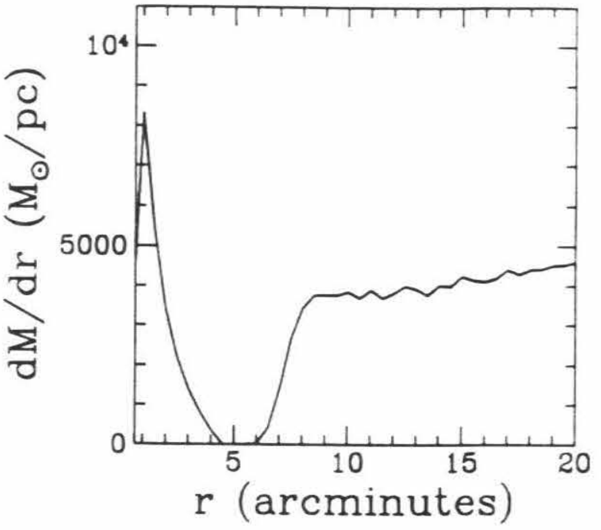

Fig. 14c

Figure 14. Gas configuration resulting from a numerical integration of an infalling orbit. Parameters of the integration are given in Table 3. Angles are given in degrees. See §5 for details. a) The solid line is the inclination angle $\omega(r)$ resulting from the numerical integration. The dotted line is the function we used to generate the models for the mosaics (§3). b) The mass surface density (in $M_\odot$/pc) of material stripped from the infalling galaxy as a function of radius. c) The solid line is the precession angle $\alpha(r)$ at the present time resulting from the numerical integration. The dotted line is the function (equation 3.4) with parameters given in Table 1) we used to generate the models for the mosaics (§3).

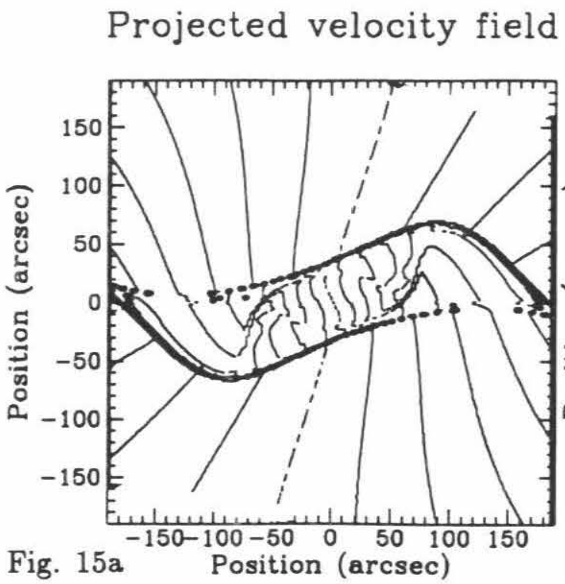

Fig. 15a

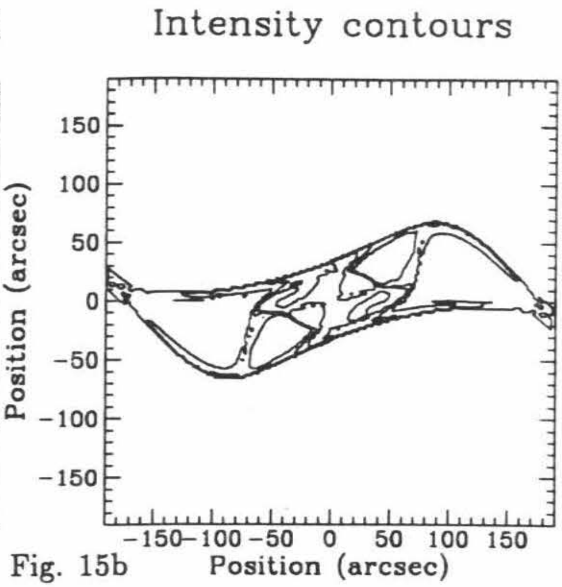

Fig. 15b

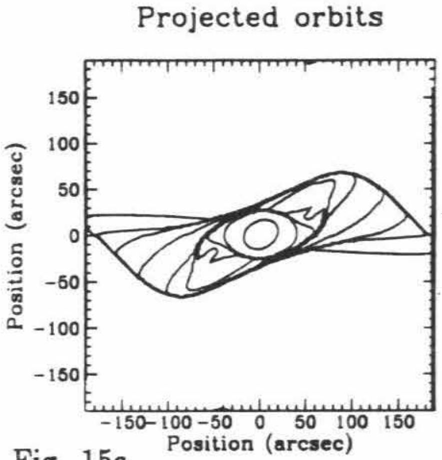

Fig. 15c

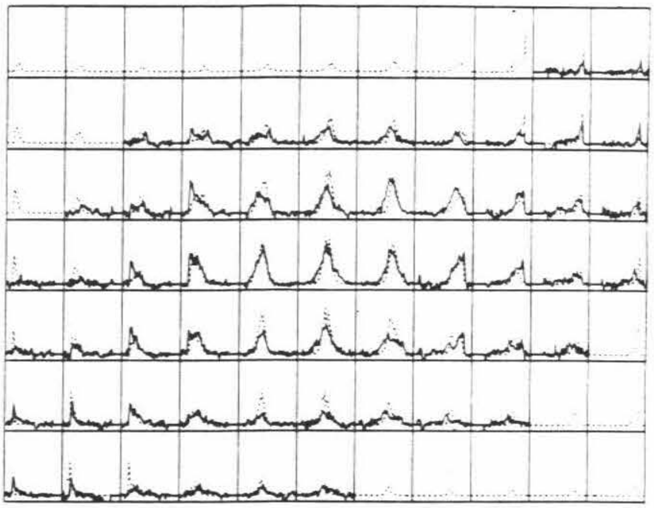

Fig. 15d

Figure 15. Kinematics of the Near Infrared Models. a) Projected model velocity field. Contours are 50 km s^{-1} apart. The dot–dash contour is at the systemic velocity V_{sys}. The dotted contours are at velocities less than V_{sys} and the solid ones indicate velocities larger than V_{sys}. b) Intensity contours. Contours are at 2, 6, 18 and 26 percent of maximum intensity level. c) Projected orbits. Contours are $20''$ apart and are the radius on the gas plane as seen on the sky. d) Comparison of model to CO data. Solid lines are the data, dotted lines are the model. The vertical axes give the main beam antenna temperature in Kelvin and range from −0.1K to 1.0K. The horizontal axes give velocity with respect to the local standard of rest, V_{LSR}, and range from 170 to 900km s^{-1}. See Chapter 2 for more details about the data.

CHAPTER 4

THE KINEMATICS OF THE MOLECULAR GAS IN M82

A.C. Quillen,[1,2] *C. E. Walker,*[3] *T.G. Phillips*[4]

---

[1] Theoretical Astrophysics, 130-33, California Institute of Technology, Pasadena, CA 91125, E-mail: alice@chico.caltech.edu

[2] Ohio State University, Dept. Astronomy, 174 W. 18th Ave., Columbus, OH 43210

[3] Astronomy Department, University of Texas, Austin, TX 78712, E-mail: cew@hypathia.as.utexas.edu

[4] Downs Laboratory of Physics 320-47, California Institute of Technology, Pasadena, CA 91125, E-mail: phillips@tacos.caltech.edu

' "Cheshire Puss, ... Would you tell me, please, which way I ought to go from here?"

"That depends a good deal on where you want to get to," said the Cat.

"I don't much care where —" said Alice.

"Then it doesn't matter which way you go," said the Cat.

"— so long as I get *somewhere,*" Alice added as an explanation.

"Oh, you're sure to do that," said the Cat, " if you only walk long enough."

Alice felt that this could not be denied, so she tried another question. "What sort of people live about here?"

"In *that* direction," the Cat said, waving its right paw round, "lives a Hatter: and in *that* direction," waving the other paw, "lives a March Hare. Visit either you like: they're both mad."

"But I don't want to go among mad people," Alice remarked.

"Oh, you can't help that," said the Cat: "we're all mad here. I'm mad. You're mad."

"How do you know I am mad?" said Alice.

"You must be," said the Cat, "or you wouldn't have come here." '

— Lewis Carroll, *Alice's Adventures in Wonderland*

ABSTRACT

We model the kinematics of the molecular gas in the nearly edge-on disk in M82, by considering velocity and surface density perturbations caused by a possible rotating kpc long bar. A model with a bar that has an Inner Linblad Resonance at $r \sim 10'' \sim 150$ pc fits the molecular observations of the inner torus. This model is consistent with the angle of the bar inferred from the K (2.2μm) isophotes. The clouds have a cloud-cloud velocity dispersion of $\sim 30\,\mathrm{km\,s^{-1}}$ implying that the disk is unstable to short timescale axisymmetric perturbations. This is consistent with the hypothesis that the high star formation efficiencies in starbursts are due to the the short timescales of gravitational instability. It is likely that the bar has mediated the starburst.

There are serious deviations from our model at large radii. It is likely that there are two components of molecular material which were not considered by our model: (i) a component at large radii that is in the galactic plane and has low line-of-sight velocities due to a larger scale bar or due to the fact that there is a lack of molecular gas over a large range of radius (perhaps due to a previous interaction which caused a large fraction of the gas to sink into the nucleus), and (ii) a molecular wind with velocities of the order of the observed line widths ($80 - 120\,\mathrm{km\,s^{-1}}$). While dense gas can be accelerated in a galactic superwind to velocities of this order of magnitude, it is unclear how this gas interacts with the superwind.

Subject headings: galaxies: individual (M82) – galaxies: kinematics and dynamics – galaxies: ISM – ISM: molecules

1. INTRODUCTION

The nearby[1] "starburst" galaxy M82 (NGC3034, 3C231, Arp 337) has been studied in almost every part of the electromagnetic spectrum. It is one of the most powerful infrared sources (of luminosity $L_{IR} = 3 \times 10^{10} L_{\odot}$, Telesco and Harper 1980) which is interpreted to be the result of a high star formation rate. In the nuclear region more than 40 compact nonthermal radio sources are detected which are most likely young supernova remnants, implying a supernova rate of ~ 0.3 supernovae per year (Kronberg *et al.* 1985). M82 suffered a close collision with M81 and NGC3077 approximately 2×10^8 years ago, which is responsible for the large steamers and tails of HI linking the three galaxies (Yun 1992, Yun *et al.* 1993,

---

[1] The distance to M82 is estimated to be 3.25 Mpc (Tammann and Sandage 1968)

Cottrell 1977). The results of a restricted N-body simulation of the three galaxy collision reproduces remarkably well the observed velocities and distribution of this gas (Yun 1992, Brouillet *et al.* 1991). It has been frequently suggested that the tidal interaction between the three galaxies triggered the starburst in the nucleus of M82.

There is a high concentration of molecular of gas ($\sim 5.5 \times 10^7 M_\odot$ Walker *et al.* 1993, Lo *et al.* 1987, Knapp *et al.* 1980) which is located in the same vicinity as the central starbursting region. This double lobed molecular structure is thought to be in the form of a rotating ring with a radius of approximately 250 pc (Weliachew *et al.* 1984, Nakai *et al.* 1987, Loiseau *et al.* 1988, 1990, Lo *et al.* 1987, Carlstrom 1988a). High resolution observations show that the molecular material is composed of separate clumps (or associations of clumps) which have sizes and velocity dispersions comparable to galactic Giant Molecular Cloud complexes (Brouillet and Schilke 1993 (hereafter BRSC)).

In the near infrared K or 2.2μm band, there is a plateau of emission which is interpreted as evidence for a kpc long bar (Telesco *et al.* 1991 (hereafter TCJDD), Larkin *et al.* 1993) which may have caused the molecular gas to sink into the nuclear region. This mechanism for fueling a starburst has been predicted by numerical simulations of galaxy-galaxy collisions which include gas dynamics (Noguchi 1987,1988, Barnes and Hernquist 1991). Comparison of extinction estimates based on near infrared colors with dust emission suggest that the molecular ring is not axisymmetric but possibly in the form of dustlanes leading each side of the bar (Larkin *et al.* 1993). The position velocity plot along the major axis of the molecular torus of BRSC, double peaks observed in the channel maps of ^{12}CO(1-0) (Carlstrom 1988a), and a twist observed in the contours of the projected velocity field of Loiseau *et al.* (1990) and Sofue *et al.* (1992) suggest that there are non-circular motions in the molecular gas, possibly induced by the bar.

In this paper, by modeling the kinematics of the molecular material we attempt to see if peculiarities of the velocities observed in the molecular material of the torus can be caused by bar induced non-circular motions. Because the disk of M82 is edge on and direct observation of the bar is not possible, we use the simplest of assumptions for the rotating bar. We assume that the bar is a quadrupolar perturbation to the potential, with corotation radius near the end of the bar. We compare our models to ^{12}CO(2-1) and ^{12}CO(3-2) maps of M82 observed at the CSO (Caltech Submillimeter Observatory) which is presented and discussed more thoroughly in Walker *et al.* (1993) (hereafter Paper I).

There is also an extended large line width component of CO emission (Stark and Carlson 1982) of mass $\sim 10^8 M_\odot$ (Lo *et al.* 1987) which has been interpreted to be in the form of a high velocity molecular outflow (Nakai *et al.* 1987), an extended halo with possible slower rotation than the galaxy (Loiseau *et al.* 1988), a rotating component displaying a decline in the rotational velocity of the galaxy (Sofue *et al.* 1992, Young and Scoville 1984) or showing tidal distortions caused by the M81,M82 NGC3077 interaction (Yun *et al.* 1993). This gas appears to be in the same region as ionized filaments extending out of M82's galactic plane (McCarthy *et al.* 1987), X-ray emission (Watson *et al.* 1984, Fabbiano 1988, Schaaf *et al.* 1989) and other observations which are believed to be associated with a galactic superwind caused by the rapid star formation in the nuclear region (Tomisaka and Ikeuchi 1988, Heckman *et al.* 1990, Chevalier and Clegg 1985). This molecular emission may also be associated with an underlying wide velocity dispersion component observed in Hα spectra (Bland and Tully 1988), and a kpc circumnuclear annulus of gas and dust observed in extinction by Waller *et al.* (1992) and in emission by Hughes *et al.* (1990).

In §2 we discuss the thickness and velocity dispersion of the molecular disk. In §3 we describe our modeling procedure and in §4 our assumptions for bar induced velocity and surface density perturbations are discussed. The models are compared with the data in §5. Our models do not fit the data in the outer regions where the diffuse component is observed. Because of the lower quality of our data in this region, and the lack of symmetry in the distribution of this gas, we do not model this component however possible configurations it are discussed in §6. A discussion follows in §7.

2. THE THICKNESS OF THE TORUS

In this section we discuss the molecular material in the plane of the galaxy. We note that although we refer to the gas as being in a torus, axisymmetry is *not* necessarily implied. By using hydrostatic equilibrium, the observed thickness of the torus provides a limit on the velocity dispersion of the clouds in the torus. Because the spectra in this region are wider than this limit, we discuss possible explanations.

If the potential is dominated by a thin stellar disk then hydrostatic equilibrium requires that the stellar density $\rho_*(r,z) \propto \mathrm{sech}^2(z/h_*)$ with scale height h_*

$$h_* \approx \frac{\sigma_*^2}{\pi G \Sigma} \tag{2.1}$$

where σ_* is the velocity dispersion of the stars, and Σ is the mass surface density at radius r of the stellar disk. The molecular torus should be located at radii close to or less than the scale length of the disk (assuming that the stellar disk has an exponential form) so that we may approximate $\Sigma(r) \sim v_c^2/G\pi r$ over the range of the molecular data. If the gas is a small fraction of the disk mass then the gas density as a function of z is approximately Gaussian, $\rho_g(z) \propto \exp(-z^2/2h_g^2)$ with scale height h_g such that

$$\frac{h_g}{h_*} \approx \frac{\sigma_g}{\sigma_*} \tag{2.2}$$

where σ_g is the velocity dispersion of the gas clouds. Substituting this into the previous expression gives

$$\frac{\sigma_g}{v_c} \sim \frac{h_g}{\sqrt{r h_*}}. \tag{2.3}$$

If the stellar scale height is greater or equal to the gas scale height then we can set a limit

$$\frac{\sigma_g}{v_c} < \sqrt{\frac{h_g}{r}}. \tag{2.4}$$

We now use the this relation to set a limit on the velocity dispersion of the gas clouds composing the disk. Recent interferometric observations show that the integrated intensity of emission from HCN at $r \sim 13''$ has a width on the sky of

$>\sim 3''$ HWHM (BRSC at $2''$ resolution) so that $h_g/r \sim 0.2$. The rotation curve reaches a maximum of $v_c \sim 100 - 130\,\mathrm{km\,s^{-1}}$ at this radius so that we may set a limit on the velocity dispersion of $\sigma_g < 55\,\mathrm{km\,s^{-1}}$. However the line widths observed in the torus are higher than this limit (Paper I, Loiseau *et al.* 1990, Carlstrom 1988a). We note the cloud complexes have line widths of less than $30\,\mathrm{km\,s^{-1}}$, (BRSC) hence the observed line widths are dominated by the bulk gas motions not the line widths of the molecular cloud complexes themselves (which may be broadened by turbulence and other processes). The high resolution ($2''$ beam) spectra have similar line widths so that the large line widths are not due to the large beam of previous observations.

There are a number of possible explanations for the observed wide profile shapes:

(i) A bar causes non-circular motion in the gas, so that each beam position samples a larger range of velocities.

(ii) Extended diffuse gas which has a larger velocity dispersion is also detected at the central positions increasing the observed profile widths.

(iii) The molecular ring is expanding (similar to one possible interpretation of non-circular velocities observed in our Galactic Center.

Recent estimates of extinction based on near infrared maps show that the extinction is higher on the eastern side of the galaxy than on the western side, although the concentration of dust and molecular gas is similar on either side of the nucleus (Larkin *et al.* 1993). This implies that the gas disk is not axisymmetric. If such a configuration is in a steady state, it is not possible for the gas to be in uniform circular motion. Double peaks observed in CO(1-0) channel maps (Carlstrom 1988a) and large line widths observed in the position velocity plot of molecular material along the major axis of the disk (BRSC) can either be interpreted as emission from an expanding gas ring, or due to non-circular motion induced by a rotating bar. Because the torus is not axisymmetric non-circular motions are a likely explanation for the large line widths. In §4 we discuss our method for modeling profile shapes in a potential with a rotating bar in order to explore this possibility.

3. KINEMATIC MODELING

In this section we describe our procedure for modeling molecular line profile shapes. Because M82 is close to edge on, it is necessary to consider the vertical structure of the disk. We model our profile shapes in a fashion similar to that previously done by Quillen *et al.* (1992); however we integrate along the line of sight as well as over the plane of the sky, so that the integration is performed in three dimensions. This integration is simplified by the assumption that the molecular material is composed of optically thick clouds with a low volume filling factor, so that the probability that any cloud is blocked by another is low. Observations that support this assumption are discussed in §3.2. The function we used to describe the surface density as a function of radius is discussed in §3.3, and our description for the vertical structure of the disk is discussed in §3.4. The projection angles for the galaxy are defined in §3.5, and the rotation curves used are described in §3.6. The form we chose for the rotating bar potential and the induced velocity and surface density perturbations are discussed in §4.

3.1 *Modeling Procedure*

Our procedure consists of doing a simulated observation in which a model velocity field is convolved with the beam of the CSO. Around each position on the sky where we have a CO spectrum, we construct a three–dimensional grid. Simultaneously we also make an array of velocity bins. At each position on the grid a mean line of sight velocity is computed, and a corresponding weight is placed at that location in the velocity bin array. This weight consists of three factors:

(i) A factor that depends on the distance between the point of the grid and the center of the beam. For the CSO, a Gaussian representation of the beam is accurate to the one percent level. We tested the sensitivity of our profile shapes to the beam of the telescope by changing the size of our model beam by a few percent. We did not see a significant difference in our model profile shapes resulting from this change.

(ii) A factor that depends on the averaged surface intensity of the model disk at that radius and azimuthal angle (see §3.3 and §4.2).

(iii) A factor which depends on z, the distance from the plane of the galaxy which describes the vertical structure of the disk (see §3.4).

Afterwards the spectrum is convolved with a Gaussian of width determined from the velocity dispersion of the clouds in the gas disk. The resulting velocity array is a model profile shape that incorporates the finite size of the telescope beam, and can be compared directly to the observations. We assume that the velocity dispersion is constant as a function of z and r. We do not consider any radiative transfer effects.

3.2 *See-through Disk*

Recent high resolution multi-line molecular studies find that the molecular gas in the torus is hot $\sim 45K$ and that the ^{12}CO(2–1) and ^{12}CO(3–2) lines are optically thick with a maximum area filling (or covering) factor (on the sky) $f_a \sim 0.5$ (Wild *et al.* 1992, Paper I). CO, HCN and HCO$^+$ observations show that the molecular material in the torus is in the form of dense clouds with a volume filling factor $f_v < 0.002$ (Carlstrom 1988b, BRSC). These estimates of area and volume filling factor imply that the probability that emitting clouds are blocked by another one is low, and that we can see through the disk. Symmetry about the nucleus of the observed projected velocity field (Carlstrom 1988a, Loiseau *et al.* 1990, Sofue *et al.* 1992) ($r \rightarrow -r$ implies $v \rightarrow -v$) is consistent with this assumption. For regions on the sky with a high area filling factor our model will overestimate the surface brightness because the opacity of individual clouds when they block one another is ignored.

3.3 *Surface Intensity of the Torus*

If the beam is filled with optically thick clouds at temperatures T_c (assuming LTE) that have an area filling factor f_a (on the sky) then the antenna temperature observed is $f_a T_c$. We describe the disk surface intensity as a function of radius in terms of the integrated intensity (integrated over all velocities) that would be observed if the disk were observed face on at high angular resolution.

There is little molecular material observed within $r < 5''$ of the nucleus, and for $r > 20''$. Therefore we chose a function for the azimuthally averaged surface intensity as a function of radius that is flat from r_1 to r_2 and decays for $r < r_1$ and for $r > r_2$. This choice roughly follows the form of the observed integrated intensity; however, we note that the observed surface density may not reflect the azimuthally averaged surface intensity because of perturbations caused by the bar. The function we use for the integrated intensity as a function of radius is

$$\begin{aligned} i(r) &= B \exp \frac{(r-r_1)^2}{-2\sigma_1^2} && r < r_1 \\ &= B && r_1 < r < r_2 \\ &= B \exp \frac{(r-r_2)^2}{-2\sigma_2^2} && r > r_2 \end{aligned} \tag{3.1}$$

where B is the integrated intensity observed ($K\,\mathrm{km\,s^{-1}}$) if the disk were observed face on at the radius of maximum surface intensity. We compare our models to two molecular lines hence we denote the integrated intensity maxima for the two lines by $B_{\mathrm{CO}(2-1)}$ and $B_{CO(3-2)}$. The line ratio between these two lines is assumed to be constant.

We have chosen a smooth function for the surface intensity as a function of radius. However, high resolution observations (at 2″) show that the disk is resolved into individual molecular cloud complexes (BRSC). Since we compare our models to lower resolution observations the effects of these individual complexes is averaged. However we do expect some deviations from our model in the data due to individual clouds. (Individual cloud complexes may cause bright pointed features in the spectra not seen in the model.)

3.4 *Vertical Structure of the Gas Disk*

If the gas is in hydrostatic equilibrium the gas density as a function of distance z from the galactic plane can be approximated by a Gaussian

$$\rho(z) \propto \exp\left(-z^2/2h_g^2\right) \tag{3.2}$$

where h_g is the scale height of the gas disk and

$$\frac{h_g}{r} = \frac{q\sigma_g}{v_c} \tag{3.3}$$

where $q^2 = h_*/r$ is the axis ratio of the stellar (and halo) component of the galaxy. This assumes that the gas clouds are in a steady state and supported primarily by their velocity dispersion σ_g which is constant as a function of z. We use this function to describe the gas density as a function of z and allow q to vary. The circular velocity, v_c used is described in §3.6. We assume that the gas scale height is azimuthally symmetric.

3.5 *Projection Angles of the Galaxy*

We describe the orientation of the galaxy with the three angles ϑ, χ and ϕ_b. We define χ to be the position angle on the sky of the projected rotational axis (z-axis) of the stellar disk (measured from the north), and ϑ to be the angle between the line of sight and the z-axis (i.e., the inclination of the galaxy). We define ϕ_b to be the angle between the major axis of the bar and the line of sight projected onto the principal plane of the galaxy. We assume that the southern side of the disk is more distant; this assumption is supported by observations showing heavier redenning on the southern side (Waller *et al.* 1992). When the less distant end of the bar is to the west of the nucleus we define $\phi_b > 0$. Our definition for ϕ_b is shown schematically in Figure 1. Estimates for the inclination of the disk of M82 based on the ellipticity of isophotes range from $\vartheta = 70 - 82^\circ$ (see references cited in TCJDD) hence we allow ϑ to vary in our models within this range. From K isophotes at a radius of $r \sim 40''$ the position angle of the galaxy is found to be $\chi \sim 20^\circ$ which we adopt in our models. TCJDD observe an offset of 4° of the K isophotes interior to $30''$. This radius is suspected to be approximately the end of the bar, since a plateau of constant K surface intensity ends at this radius. From this TCJDD find that $\phi_b \sim 68^\circ$ if the galaxy is at an inclination of $\vartheta = 80^\circ$. This estimate is crude since the inclination of the galaxy is not accurately known and the angle of the K isophotes is influenced by the form of the bar and by extinction from dust. We allow ϕ_b to vary in our models within 10° of this estimated value.

3.6 *Rotation Curves*

We explored two rotation curves, the first without an Inner Linblad Resonance (ILR) from the bar (assuming that the corotation radius is near the the end of the bar) and the second with an ILR. (See §4.3 for discussion on the location of the ILR and the angular rotation rate of the bar.) Both of these rotation curves are described by two parameters, a peak velocity A and a core radius r_0. A is close to the maximum velocity observed and is $100 - 150\,\mathrm{km\,s^{-1}}$. Previous observations suggest that the core radius is small ($r_0 < 10''$ Loiseau *et al.* 1990, Carlstrom 1988a), however the bar may induce non-circular velocities, hence the observed velocity centroids may not accurately trace the gravitation potential. We therefore treat r_0 as a free parameter.

The circular velocity at radius r for the rotation curve without an ILR is given by

$$v_c(r) = \frac{Ar}{\sqrt{(r^2 + r_0^2)}}. \tag{3.4}$$

This rotation curve is flat for $r >> r_0$ and is linear for $r << r_0$. This model has a small mass density at the nucleus and so would correspond to galaxy with a small bulge. Yun (1992)'s numerical simulations of the M82, M81, NGC 3077 encounter require a large mass for M82, and the CO and HI data observed outside a kpc radius do not support a falling rotation curve (Min *et al.* 1993, Young and Scoville 1984) so that the rotation curve could be flat at large radii. However the velocities observed in the outer positions $r > 2'$ along the major axis of the galaxy show a large decline in the rotational velocity (Sofue *et al.* 1992) so if the molecular gas is undergoing circular rotation at these radii this rotation curve will not accurately model the velocities observed at large radii.

An Inner Linblad Resonance (ILR) could exist and would be found near where the bulk of the molecular material is located (Kenney *et al.* 1992, TCJDD). The second rotation curve which has an ILR is given by

$$v_c(r) = \frac{2A\sqrt{rr_0}}{(r + r_0)} \tag{3.5}$$

and has a higher mass density near the core radius r_0 which would correspond to a central bulge component of the stellar disk. This rotation curve corresponds to a spherical density distribution with a surface density that gives a good approximation to a de Vaucouleurs $R^{1/4}$ law (Hernquist 1990).

4. GAS RESPONSE TO A BAR

Because the disk of M82 is close to edge on, we do not have much information about the bar axis ratio, the amplitude of the quadrupole and higher moments of the potential, and the bulge to disk mass ratio. Because of this lack of information we try to keep our assumptions about the bar as simple as possible.

4.1 *Bar Potential*

We assume that the rotating component of the potential caused by the bar is a quadrupolar perturbation $\Phi_1(r,\phi) = \Phi_b(r)\cos\left[2\left(\phi - \phi_b\right)\right]$, where $\Phi_b(r)$ describes the dependence of the bar potential on radius, and ϕ_b is the angle of the major axis of the bar on the principal plane of the galaxy (see §3.5). We chose the following form for $\Phi_b(r)$ as a function of radius

$$\Phi_b(r) = -\epsilon_p \Phi_0(r) \exp\frac{-(r-r_b)^2}{2\sigma_b^2} \tag{4.1}$$

where $\Phi_0(r)$ is the axisymmetric part of the potential and determined by the rotation curves described in §3.6 and ϵ_p is the ellipticity of the potential at the radius r_b. The width σ_b determines the range of range of radii where the potential has a significant ellipticity. Bar potentials derived from photometry of other barred galaxies (that are not edge on) can have a form similar to this (Athanassoula 1992b). ($r_b + \sigma_b \sim R_b$ where R_b is the end of the bar (Athannassoula 1992b)). We assume that the core of the galaxy does not have a large ellipticity. The plateau in surface intensity at K extends out to $\sim 30''$ on either side of the nucleus (TCJDD) so that r_b should be within this radius. The peak velocity width seen along the major axis of the HCN(1-0) isophotes is at $r \sim 12''$ (BRSC) so we would expect r_b to be close to this radius.

4.2 *Velocity and Surface Density Perturbations*

Gas clouds are expected to settle onto closed orbits since collisions between gas clouds dissipate energy. Recent hydrodynamic simulations of gas flows in model barred galaxies show that gas flows are intimately linked to the closed ballistic periodic orbits (Athanassoula 1992a). We note that a good fit to bar induced noncircular velocities observed in the molecular gas in the Galactic Center of our galaxy has been found assuming that the gas follows these periodic orbits (Binney *et al.* 1991). Since the velocities of the molecular data in M82 (as in the Galactic Center) can be roughly understood if most of the gas is in circular orbits, we assume that the motions induced by the bar are perturbations to circular motion, and so are in orbits that are near the closed periodic orbits. Recent observations find that the rotation of the stars and gas in the inner region is identical (McKeith *et al.* 1993). This suggests that dissipative processes may not significantly affect the gas velocities. The fact that stars are forming in the molecular disk at a high rate suggests that the velocity shear is not large. This also suggests that the gas orbits can be approximated by orbits that are close to circular.

If the gas response to the bar is small then the first order velocity perturbations v_r and v_ϕ in the plane of the galaxy are (equations 6-30 Binney and Tremaine 1987)

$$\begin{aligned} v_r(r,\phi) &= \left(\frac{4\Omega\Phi_b}{r} + 2(\Omega-\Omega_b)\frac{d\Phi_b}{dr}\right)\frac{\sin\left[2\left(\phi-\phi_b\right)\right]}{\Delta} \\ v_\phi(r,\phi) &= \left(\frac{4(\Omega-\Omega_b)\Phi_b}{r} + \frac{\kappa^2}{2\Omega}\frac{d\Phi_b}{dr}\right)\frac{\cos\left[2\left(\phi-\phi_b\right)\right]}{\Delta} \end{aligned} \tag{4.2}$$

where $\Delta = \kappa^2 - 4(\Omega-\Omega_b)^2$, κ is the epicyclic frequency, Ω_b is the bar pattern angular rotation rate, and Ω is the angular rotation rate determined from the rotation curve ($\Omega = v_c(r)/r$, see §3.6 for our adopted rotation curves). We note that we have neglected the force due to gas pressure. From the continuity equation (and neglecting dv_r/dr which should be second order), we find that the perturbation to the surface density Σ_1 is

$$\Sigma_1(r,\phi) = \frac{\Sigma_0}{2(\Omega - \Omega_b)} \left(\left(\frac{1}{r} + \frac{d\Sigma_0}{dr} \frac{1}{\Sigma_0} \right) v_r \cot \left[2\left(\phi - \phi_b \right) \right] - \frac{2v_\phi}{r} \right) \tag{4.3}$$

where Σ_0 is the unperturbed gas mass surface density (assumed axisymmetric) at radius r. In our models we assume that the CO line surface intensity is proportional to the mass surface density. We note that the equations for the velocity and surface density equations diverge near the ILR. In terms of the ballistic closed orbits of the potential, this range of radii corresponds to where a shock causes gas on an x_1 orbit to plunge onto an orbit of the x_2 family deeper in the potential (Athanassoula 1992a, Binney *et al.* 1991). Since the region where this is occurs is small, (typically a region of width less than $30R_b$, where R_b is the radius of the end of the bar) we set the perturbations to zero over this region (where $|\Delta/\Omega^2| < 0.15$). We estimate the percent of integrated intensity contributed from this range of radii to be less than 30% per CSO beam.

4.3 *Bar Angular Rotation Rate*

We may estimate the pattern angular bar rotation rate from the radius of corotation. By considering the stellar orbits near the corotation radius, Contopoulos *et al.* (1989) have shown that bars must end interior to this radius, and Kent (1990) finds that barred galaxies have a ratio of corotation radius to bar radius of ~ 1.2. Combes and Elmegreen (1993) have found from N-body simulations that galaxies with larger bulge to disk mass ratios form bars with a flat density profile and corotation radius near the end of the bar. Since M82 has a bar with a flat density profile (as observed in the K isophotes TCJDD), it is likely that corotation is near the end of the bar. From this we may estimate that $\Omega_b \sim A/(1.2R_b)$ where A is the maximum rotational velocity (see §3.6 for our adopted rotation curve), and R_b is the radius of the end of the bar. The plateau in surface intensity at K extends out to $\sim 30''$ on either side of the nucleus (TCJDD) so that $R_b \sim 30''/\sin\phi_b$. Using this estimate for Ω_b and the rotation curve described in equation (3.5), we find that $R_{ILR} \lesssim 10''$ which agrees with the estimate of TCJDD.

5. RESULTS OF MODELING

We compare our models to three sets of data. These data are composed of single disk spectra with positions in a grid centered on the 2.2μ nucleus. The first set of data is a 5×5 position map in the ^{12}CO(3-2) line with a $6''$ spacing between the positions of the grid. The second map has 9×9 positions also in the same line with a $12''$ spacing between positions. The third set of data is a 11×9 position map in ^{12}CO(2-1) with a $12''$ spacing between positions. Though the pointing offset errors between individual positions in the maps is $2''-3''$ the whole map may have a pointing offset from the position of the 2.2μm nucleus as large as $5''-6''$. When comparing the model to the profile shapes, we adjust the position of the whole map to account for this possible pointing offset. The offsets used are listed in the figure captions. The beam for the CO(2-1) data has FWHM $\sim 30''$ and for the CO(3-2) data has FWHM $\sim 20''$. See paper I for further discussion about this data.

Models are displayed in Figures 2 and 3 with parameters listed in Table 1. Ranges of the varied parameters where a good fit to the data was found are also given in Table 1. No good fit to the data was found with the rotation curve described by equation (3.4) so details of these models are not displayed. Using the rotation curve given by equation (3.5) (with ILR) a model without a bar (having circular orbits) is displayed in Figure 2, and a model with a bar is displayed in Figure 3. Integrated intensity maps are shown (for comparison to HCN(1-0) BRSC, CO(2-1) Sofue *et al.* 1992 and Loiseau *et al.* 1990, CO(1-0) Carlstrom

1988a). and a projected mean line of sight velocity plot (for comparison to Figure 3 Sofue *et al.* 1992) and a position velocity plot along the major axis of the gas (for comparison to Figure 5 BRSC and other data). Also displayed are channel maps (for comparison to channel maps in Carlstrom 1988a, BRSC, and Loiseau *et al.* 1990) and model spectral profile shapes compared with data presented in Paper I.

5.1 *Without a Bar*

Models without a bar do not fit the data or the phenomenology of the observations well. No twist in the projected velocity field is predicted by the model, and the line widths are smaller than observed. Nevertheless some parameters of our models can be determined.

The parameters of the rotation curves (see §3.6) r_0, the core radius, and A, the maximum rotational velocity, were both varied for best fit to the data. We find that our best fitting model has close to circular orbits for $r \sim 25''$ so that the peak velocity observed at this radius is equal to A. Since the disk is close to edge–on, our value for A is not sensitive to the inclination ϑ of the disk. Our best fit value for r_0 is determined by the radius where the observed line of sight velocity ceases to rise though we note that this observed radius can be influenced by the velocity perturbations caused by the bar.

We adjusted the cloud-cloud velocity dispersion σ_g (see §3.4 and §2) so that the model could reproduce the finer features in the data ($\sigma_g < 45\,\mathrm{km\,s^{-1}}$), yet did not have large spikes that are not observed in the data ($\sigma_g > 20\,\mathrm{km\,s^{-1}}$). A good fit to the data was found with $\sigma_g = 30 \pm 15\,\mathrm{km\,s^{-1}}$. We note that the dispersion of the clouds may in fact be lower than this; when clouds block one another the width of the line shapes is larger than the velocity dispersion (F. Combes, private communication). Because of the high inclination of the disk, the width of the disk observed at high resolution is approximately twice the gas scale height of the disk. The thickness of the gas disk is related to the axis ratio of the stellar disk (equation 3.3) so that our estimate for σ_g allows us to estimate $q^2 \sim h_*/r \sim 0.4$. This estimate for the axis ratio of the stellar disk is similar to the ellipticity of the observed K isophotes (Larkin *et al.* 1993) at $r < 10''$. The isophotes may be more circular at this radius than at larger radii because of a stellar nuclear bulge. That we did not find a good fit to the data using rotation curve (equation 3.4) and did with the rotation curve with an ILR (equation 3.5) also suggests that the galaxy has a central bulge at $r < 10''$. If individual molecular cloud complexes have sizes that are similar to the thickness of the disk, or if the velocity dispersion of the individual clould complexes themselves is larger than the dispersion of the clouds in the galaxy, we may have overestimated the scale height of both the gas and stellar disk.

5.2 *With a Bar*

The model with a bar has a twist in the projected mean velocity field that has been previously observed in projected velocity fields (see Figure 4 which displays the projected velocity field of Sofue *et al.* 1992). This twist can also be seen as a tendency for the intensity in channel maps around systemic velocity to allign at an angle that is not perpendicular to the major axis of the disk (see Figure 5 which displays channel maps from Loiseau *et al.* 1990). This twist causes a shift in the centroids of our model line profile at positions along the minor axis of the disk which is observed in the data (see Figure 3d).

The parameters that describe the range of radii of the bar potential are r_b and σ_b (see §4). Bar induced velocity perturbations are highest near the ILR for the rotation curve given in (equation 3.5) and highest nearest r_b for the other rotation curve. Best fits were found for $r_b \sim \sigma_b = 20'' \pm 10''$.

The peaks of the isophotes of the model are primarily determined by perturbations in the surface density caused by the bar. As a result the fits to the data were insensitive to the parameters describing the azimuthally averaged surface intensity $r_1, r_2, \sigma_1, \sigma_2$ (see §3.3) and these parameters could only be estimated crudely, however, our fits did required form for the surface intensity that had a hole in the middle. The integrated intensity between the ILR and the radius of corotation r_{CR}, is highest along the bar so peaks in the observed integrated intensity are predicted for $r = r_b \pm \sigma_b/2$ for the rotation curve without ILR and for $r_{ILR} < r < r_{CR}$ for the rotation curve with ILR. Our models have $\epsilon_p = 0.06$ which is the maximum ellipticity we allowed. Larger values cause severe departures from circular motion and our approximations are no longer valid.

Because of the large beam of the data $(21'' - 31'')$, the model profile shapes were insensitive to the value of the inclination of the galactic disk ϑ. However a low value for the inclination affected the axis ratio of the integrated intensity contours on the sky (see figure 1a). For $\vartheta < 80°$ the model disk was wider than high resolution observations of the disk (BRSC, Carlstrom 1988a). On the principal plane of the galaxy, the model contours of constant gas density are ellipses. If the gas in M82 were in the form of dust lanes leading the bar (as observed in many face on barred galaxies, and in M82 suggested by observations in the near infrared Larkin *et al.* 1993) then a lower inclination for the disk would be consistent with the observed thickness of the molecular disk.

The integrated intensity maximum of the disk when observed face on, B, (see §3.3) was scaled to fit the data for the two CO lines. $B_{CO(2-1)}$ was 30% higher than $B_{CO(3-2)}$. This small difference between the temperature of the two lines is consistent with the assumption that the disk is composed of optically thick clouds (Wild *et al.* 1992). Most of the area on the sky in these model channel maps is at a temperature less than $20K$. If the average cloud excitation temperature is $45K$ (Wild *et al.* 1992) then these areas on the sky have area filling factor of ~ 0.5 (for clouds in the given velocity channel) and our approximation of a see-through disk (see §3.2) overestimates the intensities by a factor of $\sim$ 10% (assuming Poisson statistics). For areas on the sky in the channel maps above $20K$, our approximation of a see-through disk more severely overestimates the peak intensities. However the area on the sky where this happens is small. For the most part our approximation of a see-through disk is a reasonable one. Differences between the profile shapes and integrated intensity on either side of the nucleus may be in part due to the opacity of the disk (if the gas density is not axisymmetric).

The mass surface density of the disk can be estimated from our model value of the maximum integrated intensity that would be measured if the disk were observed face on (B) and by using the empirical relation for the H_2 column density

$$N_{H_2} = \xi I_{\rm CO} \tag{5.1}$$

where $I_{\rm CO}$ is the integrated antenna temperature of the CO(1-0) line and the constant of proportionality

$$\xi = 2 - 4 \times 10^{20} {\rm cm}^{-2} ({\rm K\,km\,s}^{-1})^{-1} \tag{5.2}$$

for optically thick molecular clouds in the Galactic disk (Scoville and Good 1989). We note that the molecular clouds are different in M82 than in our galaxy so that ξ may differ in M82. For optically thick clouds the antenna temperatures in CO(2-1) and CO(1-0) are approximately the same (as is observed Wild *et al.* 1992). Using these relations with $I_{\rm CO} \sim 500{\rm K\,km\,s}^{-1}$ for our best fitting model, we find that the maximum azimuthally averaged molecular gas mass surface density is

$$\Sigma_0 \sim 0.5{\rm g/cm}^2 \sim 2.2 \times 10^2 M_\odot/{\rm pc}^2. \tag{5.3}$$

Our value for the total mass in the torus is $\sim 7 \times 10^7 M_\odot$ which agrees previous estimates ($\sim 5.5 \times 10^7 M_\odot$ Walker *et al.* 1993, Lo *et al.* 1987, Knapp *et al.* 1980). Axisymmetric stability to gravitational perturbations in a gas disk requires that $Q > 1$ where

$$Q = \frac{\sigma_g \kappa}{\pi G \Sigma_0}. \tag{5.4}$$

Using our estimate of the cloud-cloud velocity dispersion σ_g and approximating the epicyclic frequency $\kappa \sim \sqrt{2}A/r$ we find that $Q \sim 0.7$ which implies that the gas disk is unstable to perturbations (as would be expected from the observed high star formation rate). The instability has a time scale of $\sim Q/\kappa \sim 10^6$ years. We note that though these estimates are crude, they are nevertheless consistent and also support Larson (1987)'s suggestion that the high efficiency of star formation in starburts is due to the short time scale of gravitational instabilities. Gas circulating in the disk will be compressed by the bar approximately once every 4×10^6 years ($\pi/(\Omega - \Omega_b)$) which suggests that there may be a difference in angle in the plane of the galaxy between supernovae (which take $\sim 10^6$ years to occur) and the major axis of the bar. This may account for the anticorrelation between the observed supernova remnants and the dense molecular cloud cores (BRSC).

The rotation curve with an ILR gives a surprisingly good fit to the data. Our modeling procedure is successful at reproducing the observed spectra in the inner region and reproduces the large line widths of the high resolution observations (BRSC, Carlstrom *et al.* 1988a) and yet the thickness and velocity dispersion of the disk are not large and so are consistent with high resolution observations. The large extent of the intensity contours in each of the channel maps (Carlstrom 1988a, Figure 2 BRSC) and the triangular shape in the position velocity plot (Figure 3 BRSC, Carlstrom 1988a) are also predicted by our model. The ILR of this model coincides with a plateau observed in K isophotes (TCJDD). Since the near infrared colors do not differ remarkably in this region, it is unlikely that recent star formation is responsible for this plateau (Larkin *et al.* 1993) so this inner plateau may reflect a larger stellar density. Inside the ILR stellar orbits will also be aligned perpendicular to the bar which could cause the sharp jump observed in the K surface brightness at this radius.

The peaks in the data are higher than those in the model. Our model may lack these peaks since our model disk is not made up of individual molecular cloud complexes. Peaks in the integrated intensity $\sim 20\%$ higher than the average that are $\sim 10''$ apart are observed in HCN(1-0) (BRSC) so differences of this order between our model and the CO data would not be unexpected. Our model has an arbitrarily chosen form for the azimuthally averaged gas surface density as a function of radius (see §3.3). A more accurate function would give a better fit to the data. A model that considers strong surface density variations caused by the bar as well as CO opacity may also improve the fit to the data.

6. EXTENDED EMISSION

There is a component of emission which extends out of the galactic plane and to large radii along the major axis of the galaxy which is not present in our models. This component has very wide profiles shapes of width $80 - 120\,\mathrm{km\,s^{-1}}$ FWHM. The profile shapes in the outer region vary only slightly from beam position to beam position unlike the profile shapes near the nucleus. The centroids of the outer profile shapes are close to systemic velocity showing little rotation (Sofue *et al.* 1992, Loiseau *et al.* 1990, Young and Scoville 1984). The mean velocities on southern side of the galaxy are redshifted by $\sim 30\,\mathrm{km\,s^{-1}}$. This has been interpreted as evidence for a molecular outflow (Nakai *et al.* 1987). This diffuse component is brighter on the Eastern side of the galaxy and seems to be correlated with both ionized filaments and optical dustlanes (Yun *et al.* 1993, Carlstrom 1988a). The morphology of the integrated intensity of the extended emission is not symmetrical about the nucleus (Yun *et al.* 1993, Sofue *et al.* 1992).

6.1 *Material Stripped Tidally*

It is possible that this gas is gas stripped tidally due to the M82, M81, NGC3077 tidal interaction. Stripped material is not in circular motion, so it will not rotate with the galaxy. It is then possible that the line-of-sight velocity of stripped material could be close to the the systemic velocity as we observe for the diffuse extended molecular material. However material stripped tidally from the outer parts of a galactic disk is observed to have small line widths (Hibbard and van Gorkom 1992 in NGC 7252 and NGC 3921, Yun 1992, Yun *et al.* 1993 in HI tails between M81 and M82). HI and CO emission from gas far from the nucleus ($r > 3'$) along the major axis of M82 is observed to have small line widths ($30 - 60\,\mathrm{km\,s^{-1}}$ (Yun *et al.* 1993), Sofue *et al.* 1992) unlike the larger line widths observed in our data at smaller radii. The HI intensity maps at these larger radii also shows that the galactic plane of M82 begins to warp at $r > 3'$ (Yun *et al.* 1993). The low line width material near the galactic plane at $r > 3'$ is probably material stripped tidally from the galaxy, whereas the large line width material nearer to the nucleus is not.

Gas interior to the tidal radius may have been strongly affected by the tidal encounter with M81 (or perhaps by passing through the outer part of M81's disk, Yun 1992). We note that if the circular velocity at $r = 2'$ is $\sim 100\,\mathrm{km\,s^{-1}}$ then the rotational period is $\sim 10^8$ years which is similar to the time since the closest approach of M81 and M82 (Cottrell 1977, Yun 1992). Because of the slow rotation at these radii, non-axisymmetric disturbances in the disk caused by the interaction may still be present. This may in part account for the lack of symmetry about the origin in the observed CO integrated intensity.

6.2 *Gas in the Galactic Plane*

The large line widths observed in this gas suggest that either the gas is not confined to the plane of the galaxy or it is not undergoing circular motion. We first consider the possibility that a component of this the gas is found in the galactic plane. A large scale warp is unlikely because no tilt is observed in either the optical isophotes or the CO integrated intensity contours for $r < 3'$ (Sofue *et al.* 1992). It is unlikely that perturbations from spiral arms on the galactic plane could cause the appearance of both a lack of rotation and large line widths over such a large range; however a large scale tidally induced bar (larger scale than the one considered in this paper as suggested by Yun *et al.* 1993) could possibly account for these observations. If there is a lack of molecular gas over a range of radii (e.g., $0.5' \lesssim r \lesssim 1.5'$) (resulting from a previous large scale inflow into the nucleus) and a significant amount of gas remains at larger radii, then the observed low rotational velocities along the major axis of the galaxy could be from gas far from the nucleus that is undergoing circular motion. We note that in all cases the velocities observed may not accurately trace the potential of the galaxy so that Sofue *et al.* 1992's interpretation of the low rotational velocities as evidence of a small mass for M82 may not be entirely consistent.

6.3 *Gas Above the Galactic Plane*

Since there is a significant amout of dust emission observed above and below the galactic plane (Hughes *et al.* 1990) and the CO emission is correlated with Hα filaments and optical dustlanes, there must be a component of molecular gas above and below the galactic plane. The correlation with filaments and dust suggests that the molecular gas has origin from the galactic plane and is associated with the starbursting region. Our molecular spectra do not show the double peak (with separation between the peaks of $\sim 200 - 300\,\mathrm{km\,s^{-1}}$) observed in $H\alpha$ spectra along the minor axis of the galaxy (Heckman *et al.* 1990, Axon and Taylor 1978) so that this molecular component not outflowing at the high velocities of the atomic component.

Clouds can be accelerated by a hot superwind to a velocity of

$$v_{cloud} = 400 L_{bol,11}^{1/2} r_{kpc}^{-1/2} N_{21}^{-1/2}\,\mathrm{km\,s^{-1}} \tag{6.1}$$

(see the excellent review by Heckman *et al.* 1992) where N_{21} is the column density of the clouds in units of $10^{21}\mathrm{cm}^{-2}$, $L_{bol,11}$ is the bolometric luminosity of the starbursting region in units of $10^{11} L_{\odot}$ (which for M82 $L_{bol,11} \sim 0.3$ as estimated from L_{IR}) and r_{kpc} is the initial location of the clouds. Dense molecular clouds with number densities $\sim 10^{3} - 10^{6}\mathrm{cm}^{-3}$ (such as are found in the torus) and $1 - 20$ pc size scales located above the galactic plane would be accelerated to lower speeds than the atomic component to velocities of the order of the observed profile widths ($10-200\,\mathrm{km\,s^{-1}}$) (but not to the large velocities suggested by Nakai *et al.* 1987). Shocks driven by the wind into the molecular material will also heat the clouds, but if the clouds have a high density they will not be heated to high temperatures.

The pressure and the ambient radiation field determine whether molecular clouds will be disassociated. The pressure in the molecular clouds in the torus range from $10^{-12} < P < 10^{-9}$ dyne cm^{-2} assuming that the number density $10^3 < n < 10^5 \mathrm{cm}^{-3}$ and $20K < T < 40K$, while the pressure in the high temperature ($\sim 10^7 K$) gas above the plane is $P \sim 3 \times 10^{-12} \eta^{-1/2}$ dyne cm^{-2} where η is the volume filling factor of the X-ray emitting gas (Fabbiano 1988). The high pressure in the wind coupled with a less intense radiation field suggests that the molecular material may not be disassociated above the galactic plane. If there is a poloidal magnetic field geometry in the high temperature gas (Reuter *et al.* 1992), conduction between the hot and cold gas will not be important, however turbulent mixing between the high and low temperature phases (Begelman and Fabian 1990) may affect the evolution of the wind (e.g., by lowering the cooling time of the hot gas) and set the observable emission line ratios (e.g., Slavin *et al.* 1992).

It is difficult to differentiate between molecular gas clouds that are at large distances from the nucleus and clouds that are associated with the superwind. However, high resolution multi-line spectra observations should be able to tell the difference between these two components using temperature and pressure diagnostics. The amount of dust emission observed above and below the disk (Hughes *et al.* 1990) suggests that most of the CO detected above and below the disk ($10^7 - 10^8 M_\odot$) is material that has been ejected from the disk. This would imply that a large portion of the gas that could be forming stars has been ejected from the disk. This would severely lower estimates of the star formation efficiency of the starburst (Rieke *et al.* 1980).

7. SUMMARY AND CONCLUSION

In this paper we model the kinematics of the molecular gas of the nearly edge-on disk in M82. A model with velocity perturbations caused by a bar that has an Inner Linblad Resonance at $r \sim 10'' \sim 150$ pc fits the molecular observations remarkably well. This model predicts the large line widths that are observed, and yet the model disk is not thicker than observed. This model has the bar orientation angle consistent with the angle of the K isophotes interior to the end of the bar. The two-lobed appearance in the integrated intensity contours is primarily caused by non-axisymmetric perturbations in the gas surface density. The clouds have a cloud-cloud velocity dispersion of $\lesssim 30\,\mathrm{km\,s^{-1}}$ implying that the disk is unstable to short timescale axisymmetric perturbations. This is consistent with Larson (1987)'s hypothesis that the high star formation efficiencies in starbursts are due to the the short timescales of gravitational instability. It is likely that the bar mediated the starburst by causing gas in the outer parts of the disk to sink into the nucleus.

There are serious deviations from our model at large radii along the major axis of the galaxy and above and below the galactic plane. It is likely that there are two additional components of molecular material which were not considered by our model: (i) a component at large radii that is in the galactic plane and has low line of sight velocities due to a large scale bar or due to the fact that there is a lack of molecular gas over a large range of radius. (This is perhaps because of a previous interaction, which caused a large fraction of the gas to sink into the nucleus.) (ii) A molecular wind with velocities of the order of the observed line widths $(80 - 120\,\mathrm{km\,s^{-1}})$. While dense gas can be accelerated in a galactic superwind to velocities of this order, it is unclear how this gas interacts with the superwind. High resolution multi-line observations of the molecular gas above and below the disk may be able to differentiate between the two molecular components and study the nature of the molecular material in the wind. Studies of emission lines may find evidence of mixing between the phases of the wind (Slavin *et al.* 1993).

We regard this investigation as a first attempt to model the kinematics of this complex galaxy. Future models should be compared to existing higher resolution molecular data and should use the observed K surface intensity to estimate the potential of the galaxy. It is difficult to compare M82 with the results of fluid codes (such as explored by Athanassoula 1992a) because the galaxy is edge on and direct measurement of the morphology of the molecular gas and bar is not possible. Nevertheless, we hope that understanding gained from comparing observations of galaxies that are not edge-on to the results of this type of simulations will help us better understand edge on galaxies such as M82. The detailed knowledge of the M81,M82, NGC3077 interaction may soon permit exploration through N-body codes of the formation and subsequent evolution of the bar in M82. Since the mass of the gas is $\sim 10\%$ of the dynamical mass in the nucleus, it is likely that the process of causing the the gas to sink into the nucleus has caused the bar to evolve on short timescales.

We thank the CSO staff for help with the observations. We thank James Larkin for letting us be involved with his beautiful infrared images, Lee Armus for discussions about superwinds, and Min Su Yun for insight on the M82-M81-NGC3077 interaction and the tidal tails linking the three galaxies and helpful comments on this work. We thank Rob Olling for help with modeling the vertical structure of the gas disk, Peter Schilke and Nathalie Brouillet for an enlightening discussion about their beautiful high resolution HCN observations, and Lia Athanassoula for correspondence about gas dynamics in barred galaxies. We thank John Carlstrom for insight on his thesis, and S. Sridhar, Joss Bland-Hawthorn, and Mark Morris. A.C.Q. thanks E. S. Phinney and B. T. Soifer for comments and corrections which significantly improved this work. A.C.Q. thanks James R. Graham for his encouragement and hospitality in Berkeley. This research was supported in part by NASA grant NAGW 2144 (which paid the salary of A.C.Q.), NSF grant AST 90-15755 and by an A. P. Sloan Fellowship to E.S. Phinney. C.E.W acknowledges support from the W.M. Keck Foundation.

APPENDIX A. OBSERVATIONS

Observations of M82 in the $J = 2 \rightarrow 1$ and $J = 3 \rightarrow 2$ transitions of ^{12}CO were made at the Caltech Submillimeter Observatory (CSO) on Mauna Kea in 1989 March. A description of the CSO can be found in Phillips *et al.* (1987). At rest frequencies of 230 GHz and 345 GHz the beam size is 30″ FWHM and 20″ FWHM respectively. The velocity resolution for the CO(2-1) observations was $1.3\,\mathrm{km\,s^{-1}}$ over a range of $650\,\mathrm{km\,s^{-1}}$ and for the CO(3-2) observations was $0.85\,\mathrm{km\,s^{-1}}$ over a range of $430\,\mathrm{km\,s^{-1}}$. The spectra were centered at $V_{LSR} = 220\,\mathrm{km\,s^{-1}}$ (which is approximately the systemic velocity of M82 ($V_{LSR} = 230 \pm 10\,\mathrm{km\,s^{-1}}$ Loiseau *et al.* 1990).

We obtained three sets of observations, a 11×9 position map in CO(2-1), a 9×9 map in CO(3-2) and a 5×5 map in CO(3-2) with smaller spacing. Data were obtained on a grid on the sky along the east-west direction (not along the major axis of the galaxy). The spacing between the positions in the grid for the 11×9 CO(2-1) and 9×9 CO(3-2) maps was 12″, and for the 5×5 CO(3-2) maps was 6″. We note that this spacing is smaller than the beam for both frequencies. The grid is centered at the position of the 2.2μm emission peak: RA(1950)= $9^{\mathrm{h}}51^{\mathrm{m}}43^{\mathrm{s}}.9$ and DEC(1950)= 69°55′01″ (Rieke *et al.* 1980). The central 7×7 positions of the map in CO(2-1) were observed on March 7, whereas the outer positions were observed on March 27. The central 7×7 positions of the 9×9 map in CO(3-2) were observed March 25, and the outer positions were observed March 26. The 5×5 CO(3-2) map was observed on March 26. The data are displayed in Figures 1, 2. The data were calibrated by the usual ambient/chopper technique. The data were divided by the main beam efficiencies, $\eta_{MB} = 0.72$ (CO(2-1)) and $\eta = 0.6$ (CO(3-2)), as determined by continuum measurements of planets and a linear baseline was removed from the data. On source integration times range from 2 minutes near the nucleus to 3 minutes in the outer parts of the maps. There may be a relative pointing offset between individual spectra observed on different nights as large as $5-10''$. However pointing offsets between individual spectra taken on the same night should be less than $2-3''$. We checked our pointing every night by making sure that at the nuclear position, we could clearly see the double peaked profile shape centered at the systemic velocity.

‘ ’Twas brillig, and the slithy toves
Did gyre and gimble in the wabe:
All mimsy were the borogoves,
And the mome raths outgrabe.

“It seems very pretty,” she said when she had finished it, “but it’s *rather* hard to understand!” (You see she didn’t like to confess, even to herself, that she couldn’t make it out at all.) “Somehow it seems to fill my head with ideas — only I don’t exactly know what they are!...” ’

— Lewis Carroll, *Through the Looking Glass*

TABLE 1

MODEL PARAMETERS[1]

Rotation Curve[2]	
$A(\,\mathrm{km\,s^{-1}})$	140 ± 15
$V_{sys}(\,\mathrm{km\,s^{-1}})$ (LSR)	220 ± 10
$r_0('')$	15 ± 8
Surface Intensity of Torus[3]	
$B_{\mathrm{CO}(3-2)}(K\,\mathrm{km\,s^{-1}})$	500 ± 50
$r_1('')$	10 ± 3
$r_2('')$	15 ± 5
$\sigma_1('')$	5 ± 3
$\sigma_2('')$	10 ± 5
Projection Angles[4]	
χ	$20^\circ \pm 5$
ϑ	$80^\circ \pm 5$
ϕ_b^7	$60^\circ \pm 15$
Bar Parameters[5,7]	
$r_b('')$	15 ± 10
$\sigma_b('')$	15 ± 10
$\epsilon_p('')$	0.06
$\Omega_b(10^{-7}\mathrm{yr}^{-1})$	2.2
Thickness Parameters[6]	
h_*/r	0.4 ± 0.2
$\sigma_g(\,\mathrm{km\,s^{-1}})$	25 ± 15

[1] See §5 for discussion of the sensitivity of the parameters and comparison to the data. [2] See §3.6 for description of parameters. [3] See §3.3. [4] See §3.5. [5] See §4. [6] See §3.4. [7] These parameters are only used in the model with the bar.

REFERENCES

Athanassoula, E. 1992a, MNRAS, 259, 345.

Athanassoula, E. 1992b, preprint.

Axon, D.J., & Taylor, K. 1978, Nature, 274, 37.

Barnes, J.E. & Herquist, L.E. 1991, ApJL, 370, L65.

Begelman, M.C. & Fabian, A.C. 1990, MNRAS, 244, 26P.

Binney, J., & Tremaine, S. 1987, *Galactic Dynamics* (Princeton U. Press).

Binney, J.J., Gerhard, O.E., Stark, A.A., Bally, J., & Uchida, K.I. 1991, MNRAS, 252, 210.

Bland, B., & Tully, R.B. 1988, Nature, 334, 43.

Brouillet, N., Combes, F., & Baudry, A. 1991, IAU Symp Vol 146, 347.

Brouillet, N., & Schilke, P. 1993, preprint (BRSC).

Carlstrom, J.E. 1988a, Ph.D. Dissertation, University of California, Berkeley.

Carlstrom, J.E. 1988b, in Galactic and Extragalactic Star Formation, edited by R.E. Pudritz and M. Fich (Kluwer, Dordrecht), p. 571.

Chevalier, R.A., & Clegg, A.W. 1985, Nature, 317, 44.

Combes, F., & Elmegreen, B.G. 1993, A&A preprint.

Contopoulos, G., Gottesman, S.T., Hunter, Jr., J.H., & England, M.N. 1989, ApJ 343, 608.

Cottrell, G.A. 1977, MNRAS, 178, 577.

Fabbiano, G. 1988, ApJ, 330, 672.

Fridman, A.M., & Polyachenko, V.L. 1984, Physics of Gravitating Systems, (Springer Verlag New York Inc.).

Heckman, T.M., Armus, L., & Miley, G.K. 1990, ApJS, 74, 833.

Hernquist, L. 1990, ApJ, 356, 359.

Hughes, D.H., Gear, W.K., & Robson E.I. 1990, MNRAS, 244, 759.

Jarvis, B.J., Dubath, P., Martinet, L., & Bacon, R. 1988, A& A S, 74, 513.

Kenney, J.D.P., Wilson, C.D., Scoville, N.Z., Devereux, N.A., & Young, J.S. 1992, ApJ, 395, L79.

Kent, S.M. 1990, AJ, 100, 377.

Knapp, G.R., Phillips, T.G., Huggins, P.J., Leighton, L.B., & Wannier, P.G. 1980, ApJ, 240, 60.

Krolik, J.H., & Begelman, M.C. 1988, ApJ, 329, 702.

Kronberg, P.P., Biermann, P., Schwab., F.R. 1985, ApJ, 291,693.

Larkin, J.E., Graham, J.R., Matthews, K., Soifer, B.T., Beckwith, S., Herbst, T.M. & Quillen, A.C. 1993, ApJ submitted.

Larson, R. 1987, in Starbursts and Galaxy evolution, ed. T. Thuan, T. Montmerle, and T. Tran Thahn Van (Editions Frontieres: Paris), p. 467.

Lester, D.F., Carr, J.S., Joy, M., & Gaffney, N. 1990, ApJ, 352, 544.

Lo, K.Y., Cheung, K.W., Masson, C.R. , Phillips, T.G., Scott, S.L., & Woody, D.P. 1987, ApJ, 312, 574.

Loiseau, N., Nakai, Y., Wielebinski, R., Peuter, H.P., & Klein, U. 1990, A&A, 228, 331.

Loiseau ,N., Reuter, H.P., Wielebinski, R., & Klein U. 1988, A&A, 200, L1.

McCarthy, P.J., Heckman, T., & van Breugel, W. 1987, AJ, 92, 264.

McKeith, C.D., Castles. J., Greve, A., & Downes, D. 1993, preprint.

Nakai, N., Hayashi, M., Handa, T., Sofue, Y., & Hasegawa T. 1987, PASJ, 39, 685.

Noguchi, M. 1987, MNRAS, 228, 635.

Noguchi, M. 1988, A& A, 203, 259.

Quillen, A. C., de Zeeuw, P.T., Phinney, E.S, & Phillips, T. G. 1992, ApJ, 392, 121.

Rieke, G.H., Lebofsky, M.J., Thompson, E.I., Low, F.J., & Tokunaga, A.T. 1980, ApJ, 238,24.

Reuter, H.P., Klein, U., Lesche, H., Wielebinski, R. & Kronberg, P. 1992, A & A, 256, 10.

Schaaf, R., Pietsch, W., Biermann, P.L., Kronberg, P.P., & Schmutzler, T. 1989, ApJ, 336, 722.

Slavin, J.D., Schull, M.J. & Begelman, M.C. 1993, preprint.

Sofue, Y., Reuter, H.P., Krause, M., Wielebinski, R., & Nakai, N. 1992, ApJ, 395, 126.

Scoville, N.Z., & Good, J.C. 1989, ApJ, 339, 149.

Stark, A.A., & Carlson, E.R. 1982, 279, 122.

Tammann, G.A., Sandage, A.R. 1968, ApJ, 151, 825.

Telesco, C.M., Campins, H., Joy, M., Dietz, K., & Decher, R. 1991, ApJ, 369, 135 (TCJDD).

Telesco, C.M., & Harper, D.A. 1980, ApJ, 235, 392.

Tilanus, R.P.J., Tacconi, L.J. , Sutton, E.C., Zhou, S., Sanders, D.B., Wynn-Williams , C.G. Lo, K.Y., & Stephens, S.A. 1991, ApJ 376, 500.

Tomisaka, K., and Ikeuchi, S. 1988, ApJ, 330, 695.

Turner, J.L., Martin, R.N., Ho, P.T.P. 1991, ApJ, 367, 677.

Waller, W.H., Gurwell, M., & Tamura M. 1992, AJ, 104, 63.

Walker, C.E., Quillen, A.C., Phillips, T.G.,& Bash, F.N. 1993, preprint (Paper I).

Watson, M.G., Stanger, V., & Griffiths, R.E. 1984, ApJ, 286, 144.

Weliachew, L., Fomalont, E.B., & Grieson, E.W. 1984, A & A , 137, 335.

Wild, W., Harris, A.I., Eckart, A., Gensel, R., Graf, U.U., Jackson, J.M., Russell, A.P.G., Stutzki, J. 1992, A&A, 265, 447.

Young, J.S., & Scoville, N.Z. 1984, ApJ, 187, 153.

Yun, Min Su, 1992, Ph.D. Dissertation, Harvard University.

Yun, M. S., Ho, P.T.P. & Lo, K.Y. 1993, ApJ preprint.

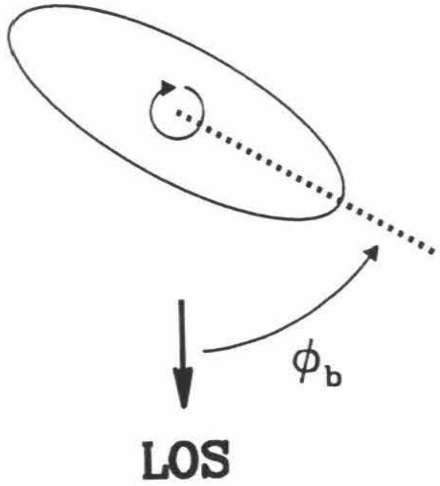

Figure 1. Definition of the bar angle ϕ_b. This figure shows the bar (represented by the ellipse) in the plane of the galaxy. LOS is the line of sight. The dotted line follows the major axis of the bar. The circle in the center shows the direction of galactic rotation. The nearer side of the bar is to the west of the nucleus on the sky.

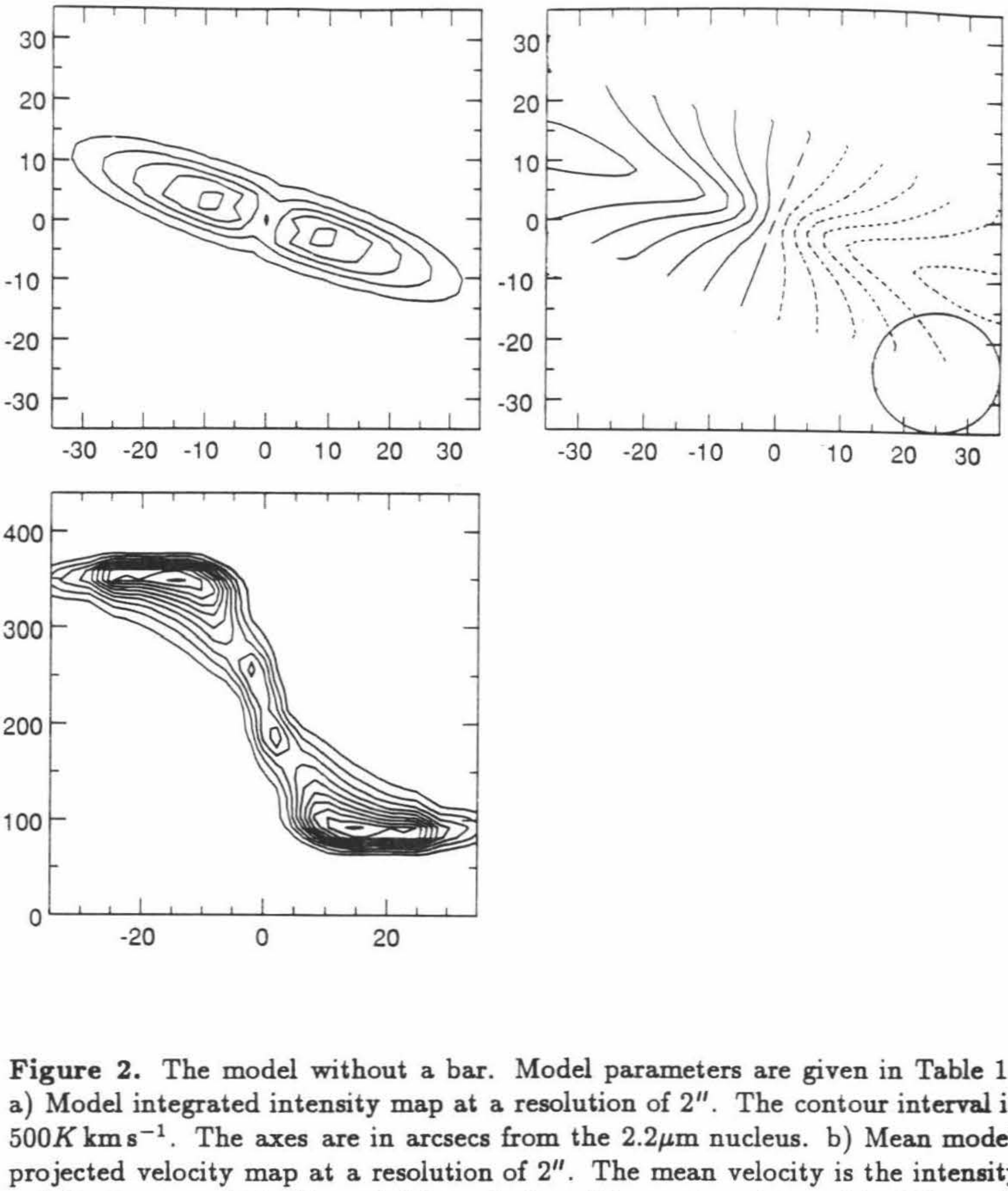

Figure 2. The model without a bar. Model parameters are given in Table 1. a) Model integrated intensity map at a resolution of 2″. The contour interval is $500K\,\mathrm{km\,s^{-1}}$. The axes are in arcsecs from the 2.2μm nucleus. b) Mean model projected velocity map at a resolution of 2″. The mean velocity is the intensity weighted mean of the line of sight velocity. The contour interval is $20\,\mathrm{km\,s^{-1}}$. Solid lines are at velocities greater or equal to the systemic velocity and dotted lines are at velocities lower than systemic velocity. The axes are in arcsecs from the 2.2μ nucleus. The 20″ beam is displayed as a circle in the lower right hand corner. c) Model position velocity map along the major axis of the galaxy in a strip on the sky of 8″ wide (for comparison to Figure 5 of BRSC). The contour interval is $10K$. The horizontal axis is in arcsec and the vertical axis is in $\mathrm{km\,s^{-1}}$ (VLSR).

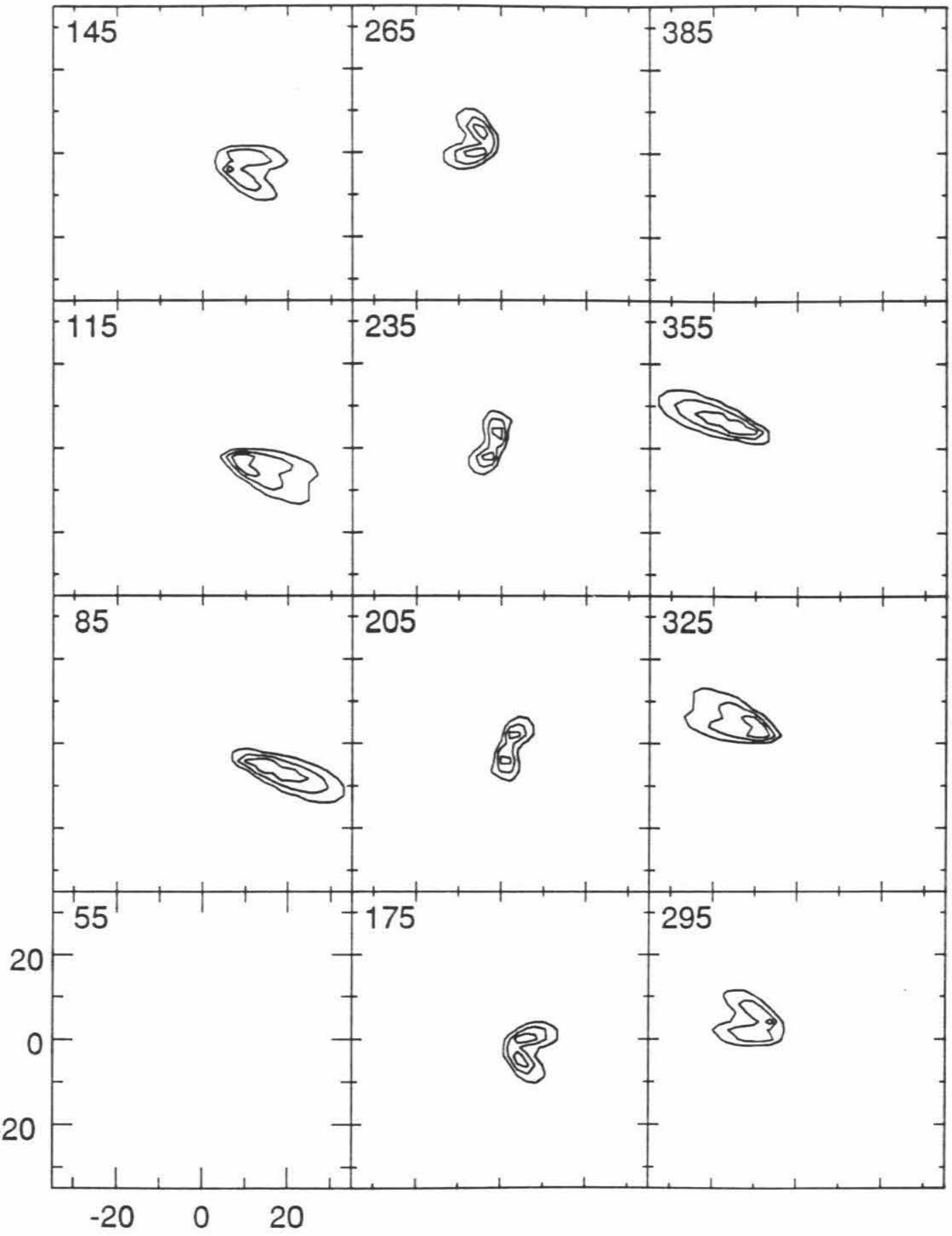

Figure 2d) Model channel maps. The contour interval is $10K$. The central velocity for each channel (VLSR) is written on the top left hand corner of each map. The axes are in arcsecs from the 2.2μ nucleus.

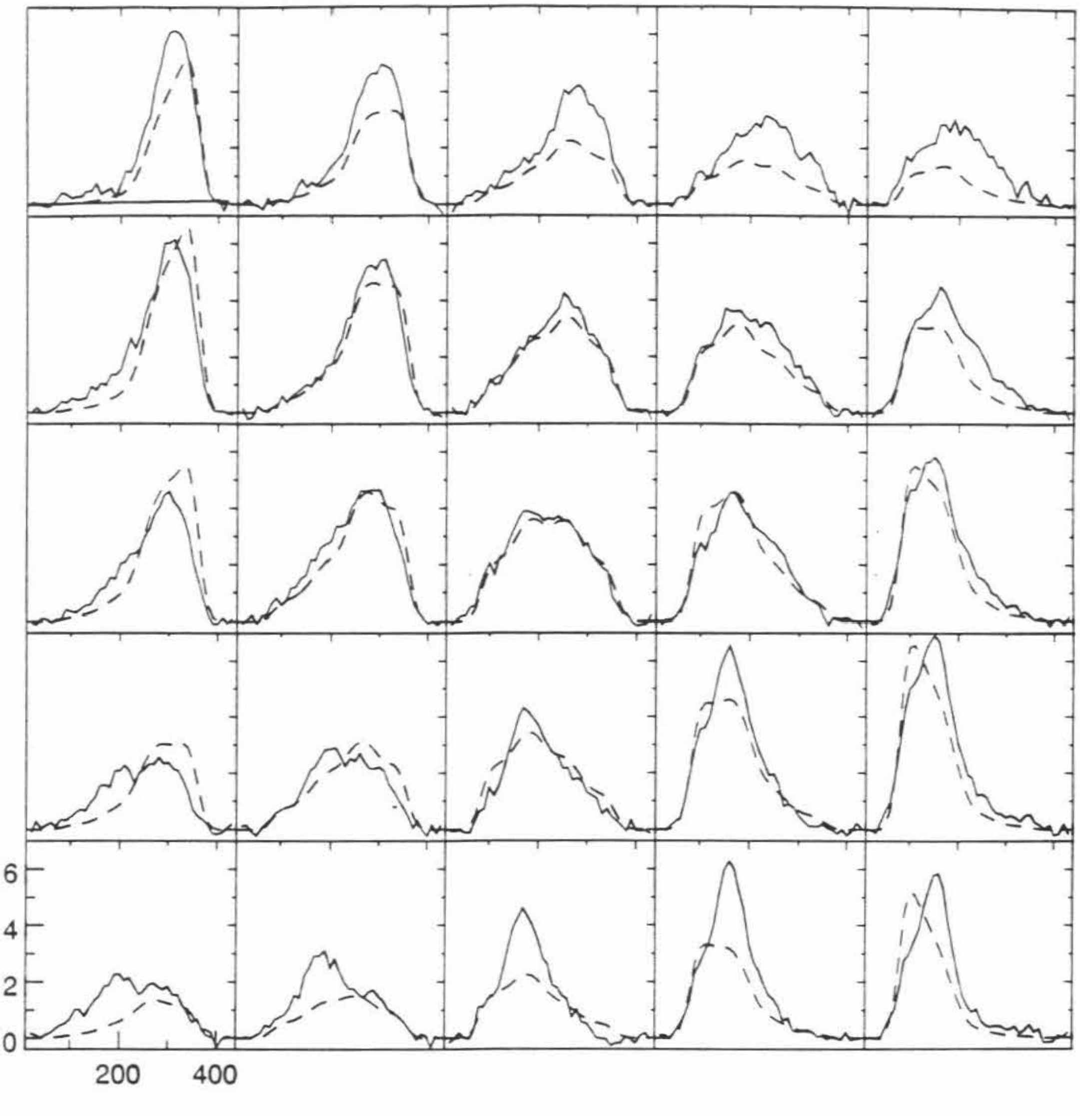

Figure 2e) Comparison of ^{12}CO observations with the model without a bar. Individual spectra of 5×5 grid in ^{12}CO(3-2). The data were taken on a north-south, east-west grid with a grid spacing of 6″ between positions centered at the 2.2μm nucleus. The velocity resolution displayed here is $10\,\mathrm{km\,s^{-1}}$. The vertical axis is given in antenna temperature, the horizontal axis in $\mathrm{km\,s^{-1}}$ (VLSR). The dotted line is the model and the solid line is the data.

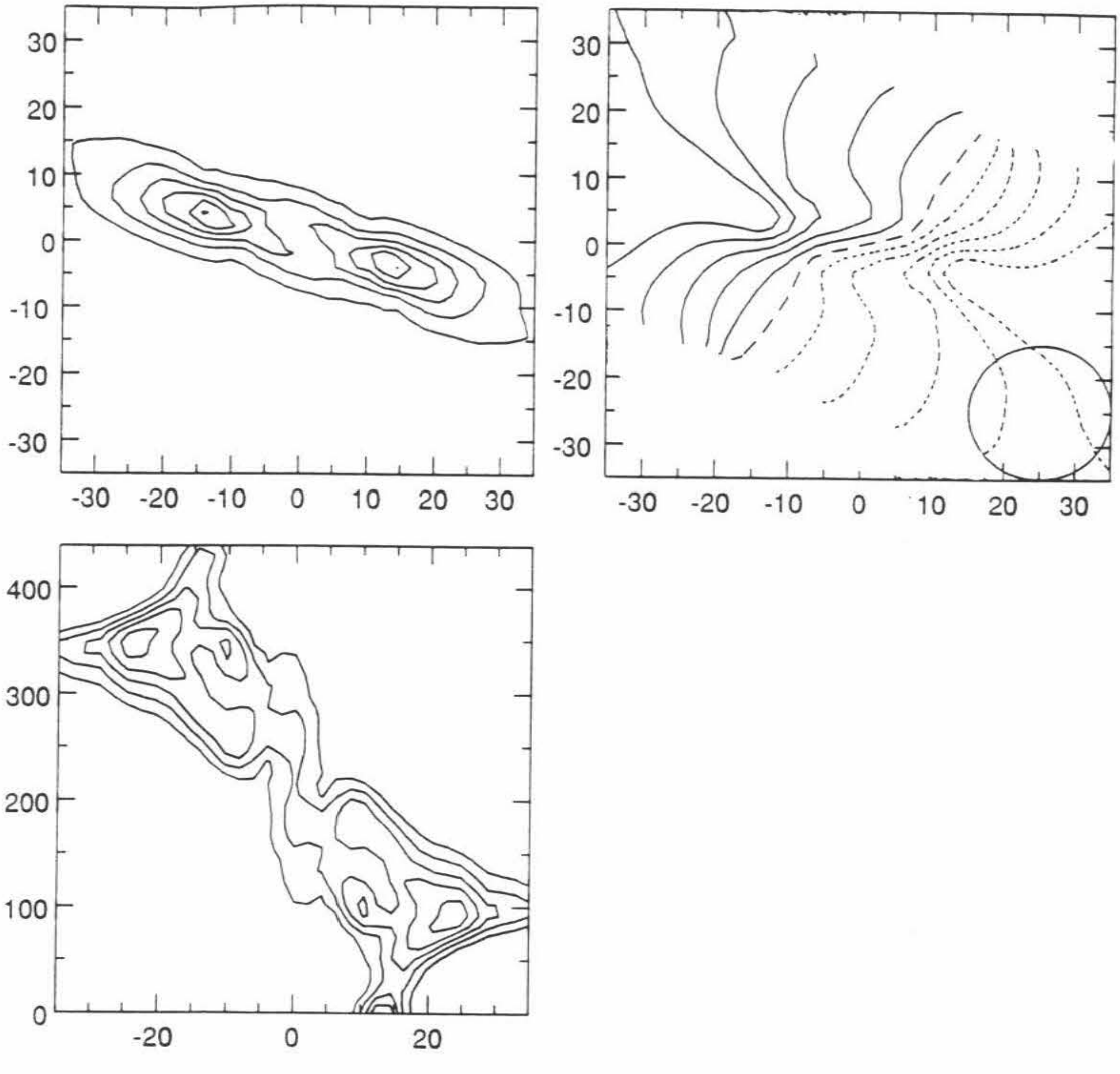

Figure 3. The model with a bar. Model parameters are given in Table 1. a) Integrated intensity map. b) Projected velocity map. c) Position Velocity map along the major axis. See Figure 2 caption and text for further details.

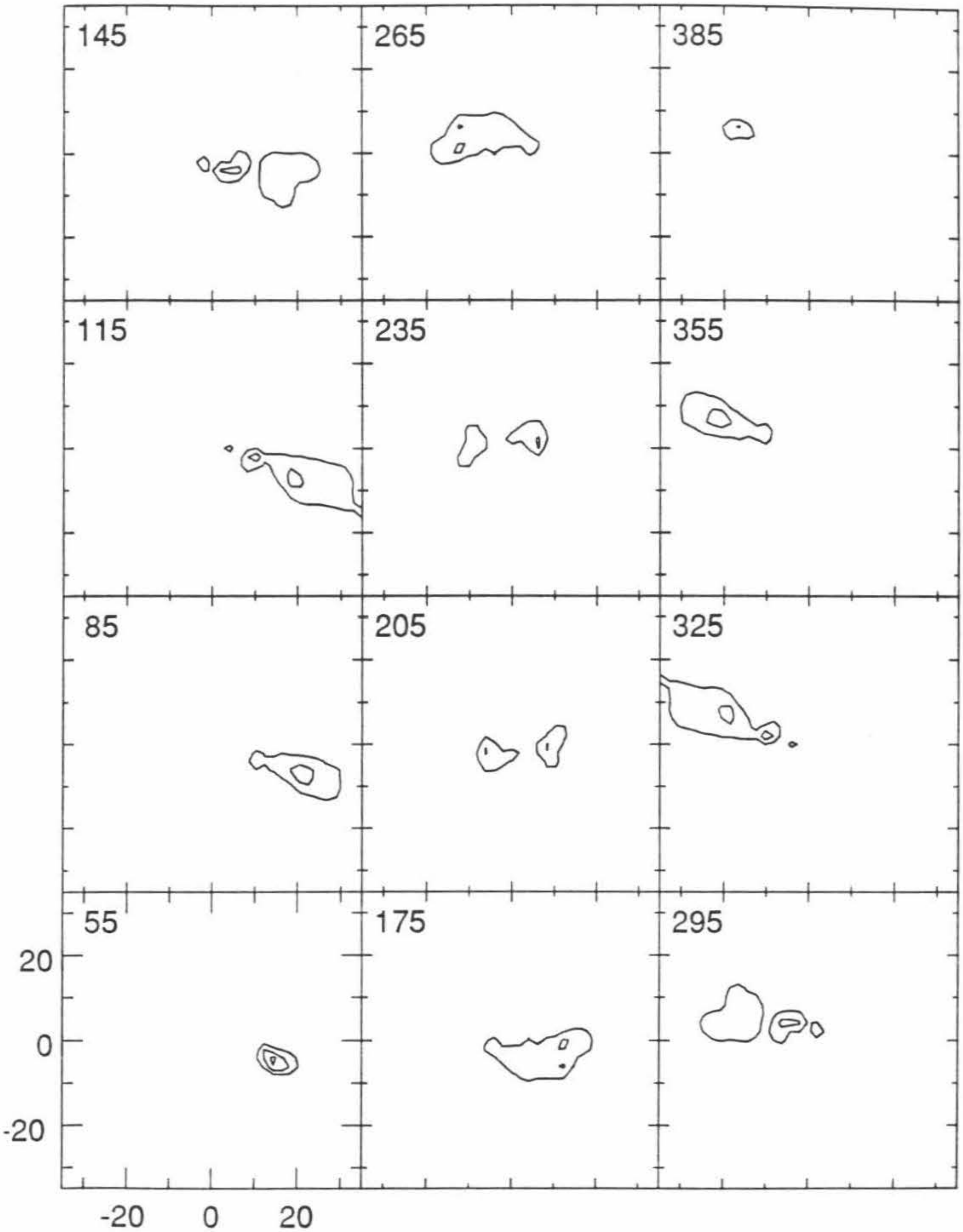

Figure 3d) Model channel maps.

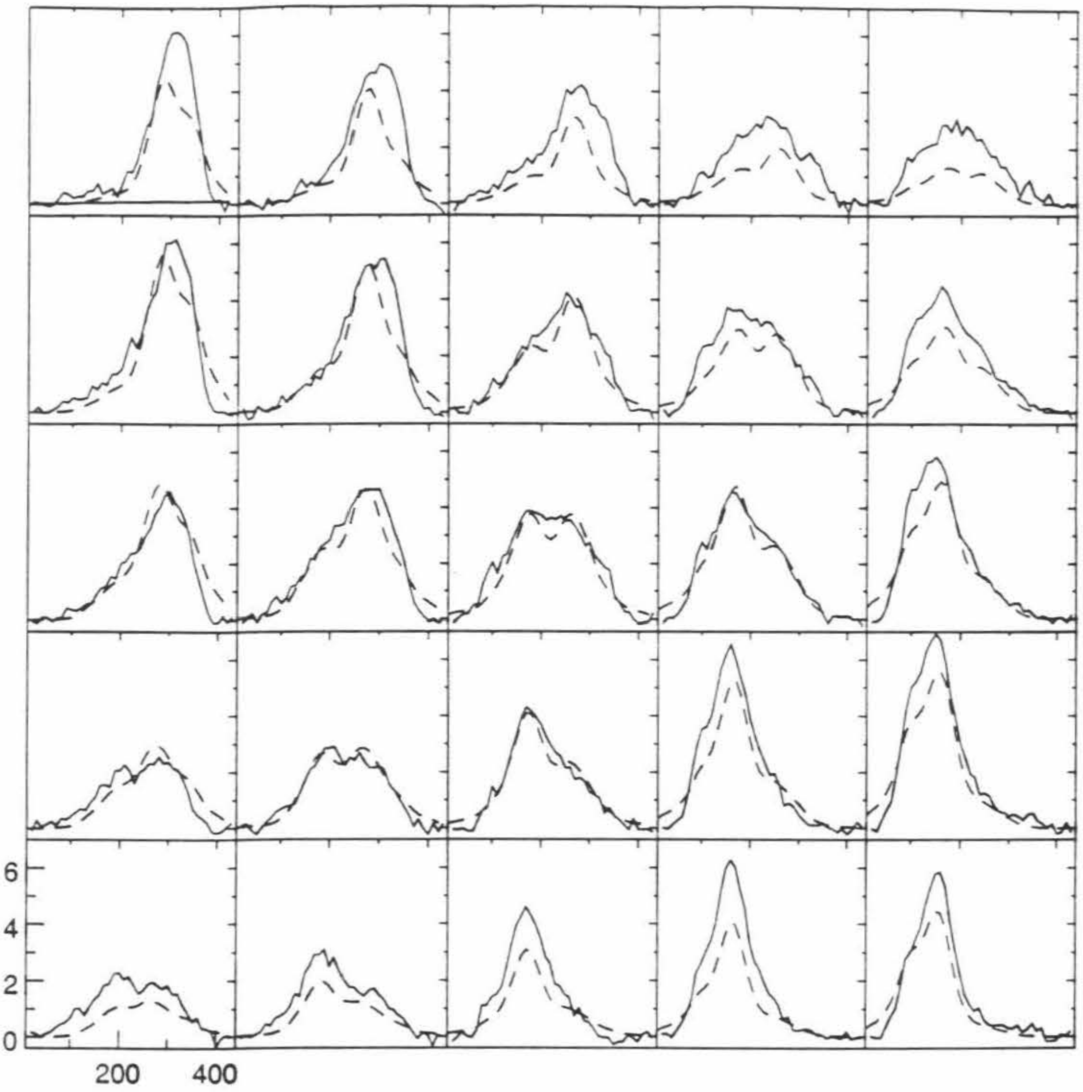

Figure 3e) Comparison of ^{12}CO observations with a model with a bar. Individual spectra of 5×5 grid in ^{12}CO(3-2). The dotted line is the model and the solid line is the data.

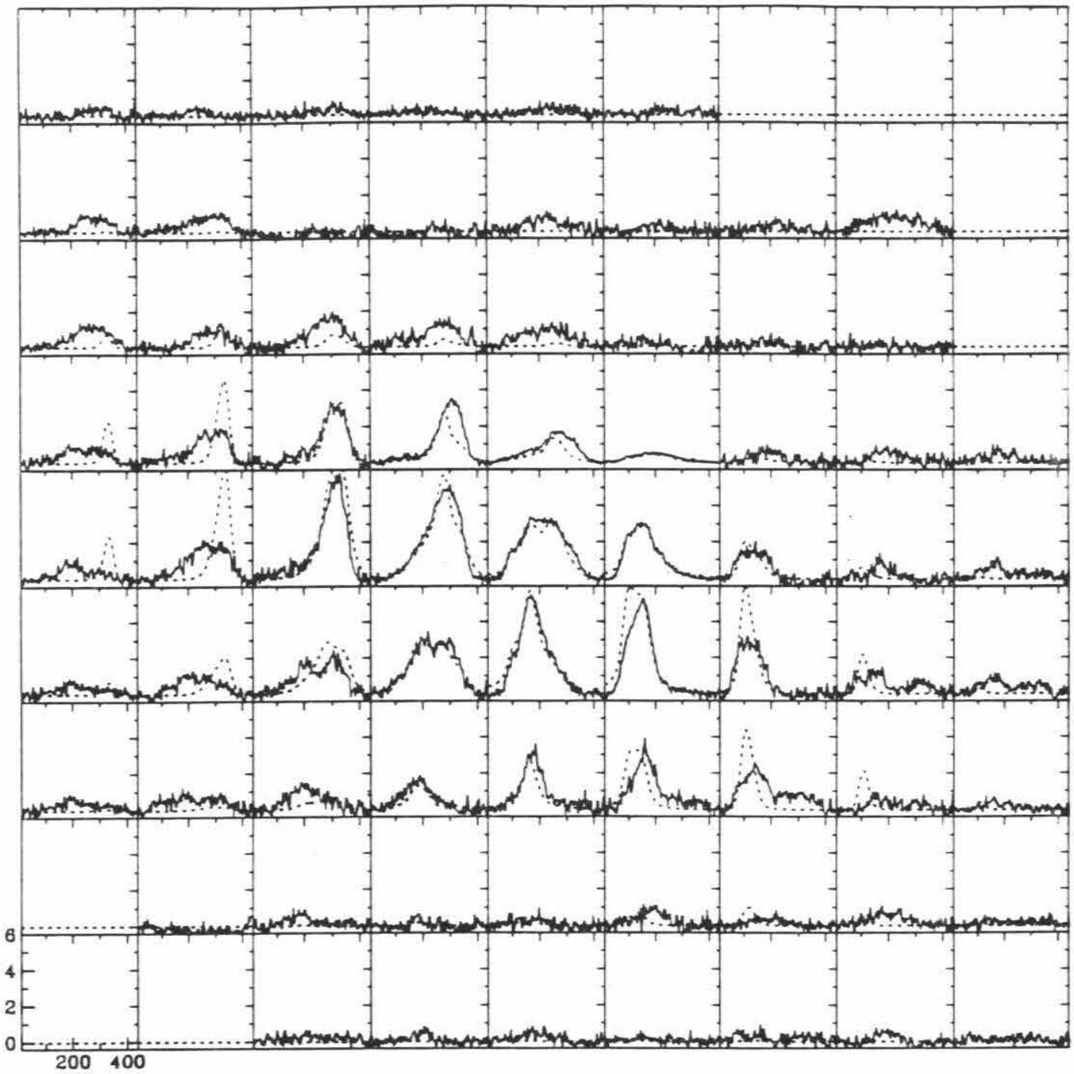

Figure 3f) Comparison of ^{12}CO observations with a model with a bar. Individual spectra of 9×11 grid in ^{12}CO(3-2). The grid spacing is $12''$ between positions. The data has a pointing offset so that the central position of the map is $-5''$ to the west and $-5''$ to the north of the 2.2μm nucleus. Axes are the in the same units as Figure 2e. The dotted line is the model and the solid line is the data.

Figure 3g) Comparison of ^{12}CO observations with a model with a bar. Individual spectra of 9×9 grid in ^{12}CO(2-1). The grid spacing is $12''$ between positions. The data has a pointing offset so that the central position of the map is $-5''$ to the west and $-5''$ to the north of the 2.2μm nucleus. Axes are the in the same units as Figure 2e. The dotted line is the model and the solid line is the data.

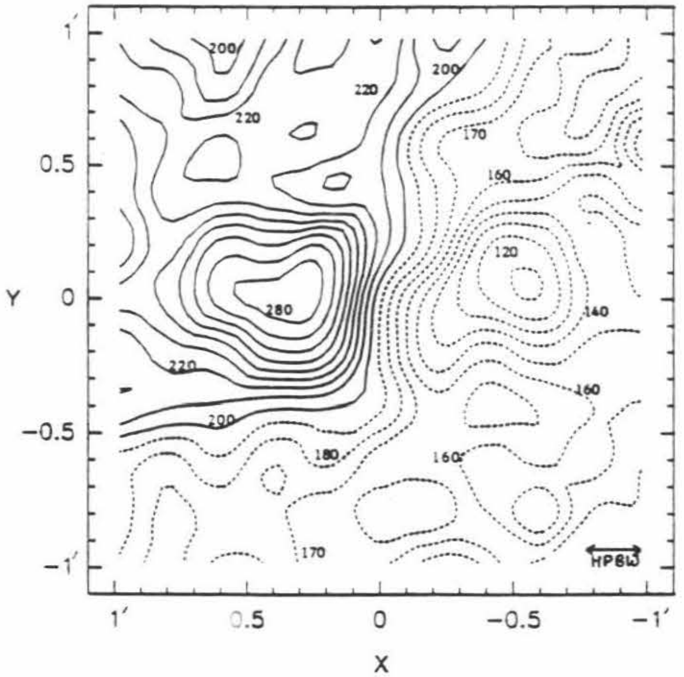

FIG. 3.—Mean velocity field for M82 as obtained from the CO($J = 2 - 1$) observations. LSR velocities in km s^{-1} are indicated on the contours.

Figure 4 Mean velocity field from Sofue *et al.* (1992). The x direction is along the major axis of the galaxy.

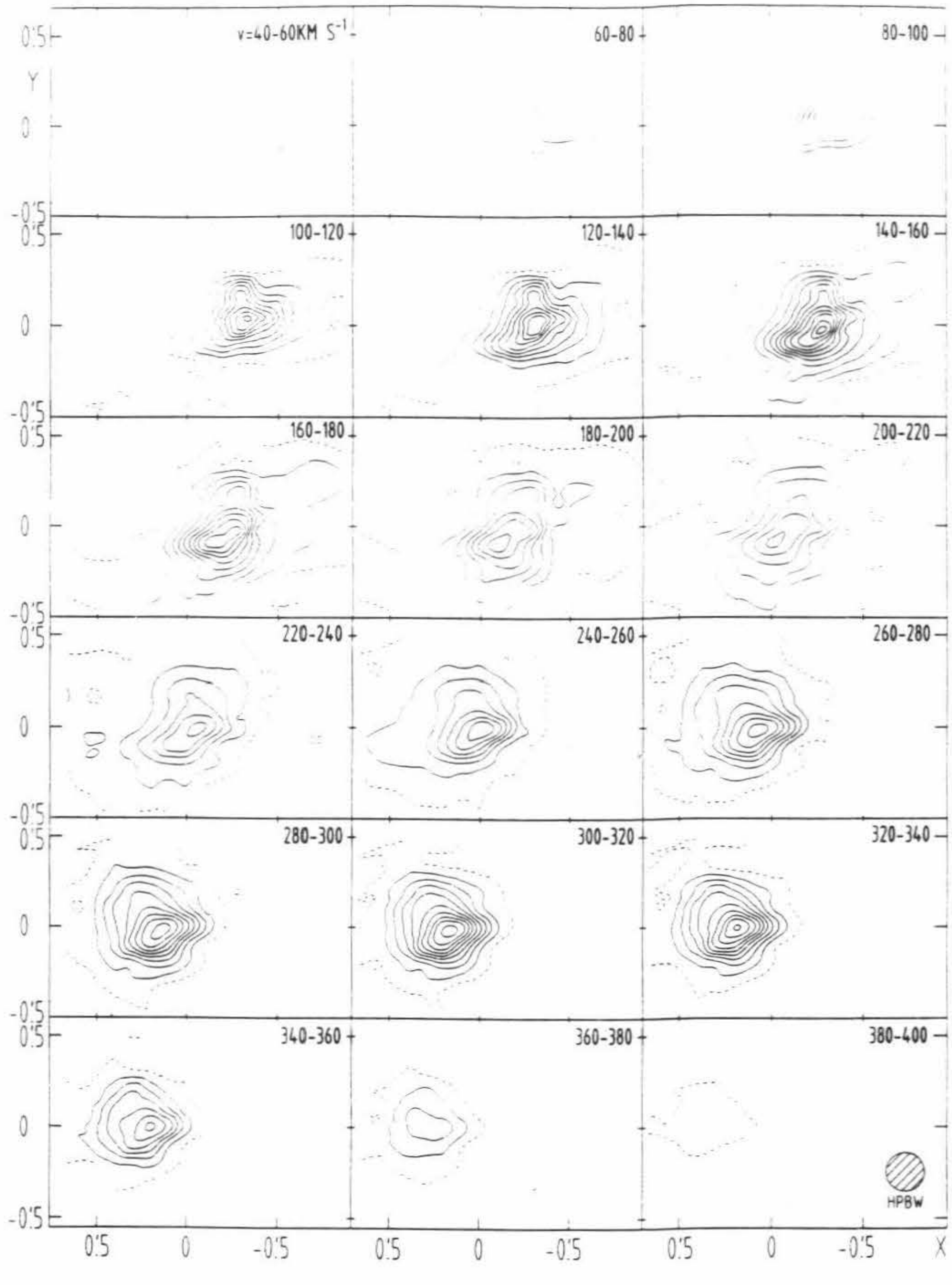

Fig. 4. Channel maps of the ^{12}CO ($J=2-1$) line intensity at every 20 km s^{-1} velocity interval. Contours are 5 (dashed), 15, 25, ... K km s^{-1}

Figure 5 Channel maps from Loiseau *et al.* (1990). The horizontal direction is along the major axis of the galaxy.